arXiv:1612.06137v3 [math.NA] 3 Feb 2017

Optimal Paths for Variants of the 2D and 3D Reeds-Shepp Car with Applications in Image Analysis

R. Duits * · **S.P.L. Meesters** * · **J-M. Mirebeau** * · **J.M. Portegies** *

Abstract We introduce a PDE-based approach for finding minimal paths for the Reeds-Shepp car. In our model we minimize a (data-driven) functional involving both curvature and length penalization, with several generalizations. Our approach encompasses the two and three dimensional variants of this model, state dependent costs, and moreover, the possibility of removing the reverse gear of the vehicle. We prove both global and local controllability results of the models.

Via eikonal equations on the manifold $\mathbb{R}^d \times \mathbb{S}^{d-1}$ we compute distance maps w.r.t. highly anisotropic Finsler functions, which approximate the singular (pseudo)-metrics underlying the model. This is achieved using a Fast-Marching (FM) method, building on Mirebeau [37, 38]. The FM method is based on specific discretization stencils which are adapted to the preferred directions of the metric and obey a generalized acuteness property. The shortest paths can be found with a gradient descent method on the distance map, which we formalize in a theorem. We justify the use of our approximating metrics by proving convergence results.

Our curve optimization model in $\mathbb{R}^d \times \mathbb{S}^{d-1}$ with data-driven cost allows to extract complex tubular structures from medical images, e.g. crossings, and incomplete data due to occlusions or low contrast. Our work extends the results of Sanguinetti et al. [47] on numerical sub-Riemannian eikonal equations and the Reeds-Shepp Car to 3D, with comparisons to exact solutions by Duits et al. [23].

Numerical experiments show the high potential of our method in two applications: vessel tracking in retinal images for the case $d = 2$, and brain connectivity measures from diffusion weighted MRI-data for the case $d = 3$, extending the work of Bekkers et al [7]. We demonstrate how the new model without reverse gear better handles bifurcations.

* Joint main authors ·
R. Duits, S.P.L. Meesters, J.M. Portegies
CASA, Eindhoven University of Technology, The Netherlands
Tel.: +31-40-2472859
E-mail: {r.duits, s.p.l.meesters, j.m.portegies}@tue.nl

J-M. Mirebeau
University Paris-Sud, CNRS, University Paris-Saclay, 91405 Orsay, France
E-mail: jean-marie.mirebeau@math.u-psud.fr

1 Introduction

Shortest paths in position and orientation space are central in this paper. Dubins describes in [20] the problem of finding shortest paths for a car in the plane between initial and final points and direction is introduced, with a penalization on the radius of curvature, for a car that has no reverse gear. Reeds and Shepp consider in [44] the same problem, but then for a car that does have the possibility for backward motion. In both papers, the focus lies on describing and proving the general shape of the optimal paths, without giving explicit solutions for the shortest paths.

This can be considered a curve optimization problem in the space $\mathbb{R}^2 \times (\mathbb{R}/2\pi\mathbb{Z})$, equipped with the natural euclidean metric but only among curves $\gamma(t) = (x(t), y(t), \theta(t))$ subject to the constraint that $(\dot{x}(t), \dot{y}(t))$ is proportional to $(\cos\theta(t), \sin\theta(t))$. Formulating the problem this way, it becomes one of the simplest examples of sub-Riemannian (SR) geometry: the tangent vector $\dot{\gamma}(t)$ is constrained to remain in the span of $(\cos\theta(t), \sin\theta(t), 0)$ and $(0, 0, 1)$. The SR curve optimization problem and the properties of its geodesics in $\mathbb{R}^2 \times \mathbb{S}^1$ have been studied and applied in image analysis by [42, 14, 21, 10, 39, 34, 2, 9], whereas a complete and optimal synthesis for the geometric control problem on

$\mathbb{R}^2 \times \mathbb{S}^1$ with uniform cost is provided by Sachkov [46]. Properties of SR geodesics in $\mathbb{R}^d \times \mathbb{S}^{d-1}$ with $d = 3$ have been studied in [23] and for general d in [24].

On the left in Fig. 1, we show an example of an optimal path between two points in $\mathbb{R}^2 \times \mathbb{S}^1$. The projection on $\mathbb{R}^2$ of this curve shows a cusp, after which the car continues in reverse (the red part of the line). From the perspective of image analysis applications this is undesirable and it is a valid question what the optimal paths are if cusps and reverse gear are not allowed. In this paper, similar to the difference between the Dubins car and the Reeds-Shepp car, we also consider this variant: it can be accounted for by requiring that the proportionality constant is non-negative. This variant falls outside the SR framework and requires asymmetric Finsler geometry instead.

Furthermore, we would like to extend the metric using two data-driven factors that can vary with position and orientation. This can be used to compute shortest paths for a car, where for example road conditions and obstacles are taken into account. In [7] it is shown that this approach is useful for tracking vessels in retinal images. Likewise, the 3D variant of the problem provides a basis for algorithms for blood vessel detection in 3D MRA data, or detection of shortest paths and quantification of structural connectivity in 5D diffusion weighted MRI data of the brain.

1.1 A distance function and the corresponding shortest paths on $\mathbb{R}^d \times S^{d-1}$

We fix the dimension $d \geq 2$, and let $\mathbb{M} := \mathbb{R}^d \times \mathbb{S}^{d-1}$ be the $2d-1$ dimensional manifold of positions and orientations. We use a Finsler metric on the tangent bundle of $\mathbb{M}$, $\mathcal{F} : T(\mathbb{M}) \to [0, +\infty]$ [1], of which specific properties are discussed later, to define a geometry on $\mathbb{M}$. Any such Finsler metric $\mathcal{F}$ induces a measure of length $\text{Length}_{\mathcal{F}}$ on the class of paths with Lipschitz regularity, defined as[2]

$$\text{Length}_{\mathcal{F}}(\gamma) := \int_0^1 \mathcal{F}(\gamma(t), \dot{\gamma}(t))\, \mathrm{d}t,$$

with the convention $\dot{\gamma}(t) := \frac{d}{dt}\gamma(t)$. The path is said to be *normalized* w.r.t. $\mathcal{F}$ iff $\mathcal{F}(\gamma(t), \dot{\gamma}(t)) = \text{Length}_{\mathcal{F}}(\gamma)$ for all $t \in [0, 1]$. Any path of finite length can be normalized by a suitable reparametrization. Finally, the pseudo-distance $d_{\mathcal{F}} : \mathbb{M} \times \mathbb{M} \to [0, +\infty]$ is defined for all $\mathbf{p}, \mathbf{q} \in \mathbb{M}$ by

$$d_{\mathcal{F}}(\mathbf{p}, \mathbf{q}) := \inf\{ \text{Length}_{\mathcal{F}}(\gamma) \mid \gamma \in \Gamma,\ \gamma(0) = \mathbf{p},\ \gamma(1) = \mathbf{q}\}, \quad (1)$$
$$\text{with } \Gamma := \text{Lip}([0, 1], \mathbb{M}).$$

Normalized minimizers of (1) are called minimal geodesics from $\mathbf{p}$ to $\mathbf{q}$ w.r.t. $\mathcal{F}$. For certain pairs $(\mathbf{p}, \mathbf{q})$ these minimizers may not be unique, and these points are often of interest.

Definition 1 (Maxwell point) Let $\mathbf{p}_S \in \mathbb{M}$ be a fixed point source and $\gamma \in \Gamma$ a geodesic connecting $\mathbf{p}_S$ with $\mathbf{q} \in \mathbb{M}$. Then $\mathbf{q}$ is a Maxwell point if there exists another extremal path $\tilde{\gamma} \in \Gamma$ connecting $\mathbf{p}_S$ and $\mathbf{q}$, with $\text{Length}_{\mathcal{F}}(\gamma) = \text{Length}_{\mathcal{F}}(\tilde{\gamma})$. If $\mathbf{q}$ is the first point (distinct from $\mathbf{p}_S$) on γ where such $\tilde{\gamma}$ exists, then $\mathbf{q}$ is called the first Maxwell point. The curves $\gamma, \tilde{\gamma}$ lose global optimality after the first Maxwell point.

1.2 Geometry of the Reeds-Shepp model

We introduce the metric $\mathcal{F}_0$ underlying the Reeds-Shepp car model, and the metric $\mathcal{F}_0^+$ corresponding to the variant without reverse gear. Let $(\mathbf{p}, \dot{\mathbf{p}}) \in T(\mathbb{M})$ be a pair consisting of a point $\mathbf{p} \in \mathbb{M}$ and a tangent vector $\dot{\mathbf{p}} \in T_{\mathbf{p}}(\mathbb{M})$ at this point. The physical and angular components of a point $\mathbf{p} \in \mathbb{M}$ are denoted by $\mathbf{x} \in \mathbb{R}^d$ and $\mathbf{n} \in \mathbb{S}^{d-1}$, and this convention carries over to the tangent:

$$\mathbf{p} = (\mathbf{x}, \mathbf{n}), \qquad \dot{\mathbf{p}} = (\dot{\mathbf{x}}, \dot{\mathbf{n}}) \in T_{\mathbf{p}}(\mathbb{M}).$$

We say that $\dot{\mathbf{x}}$ is proportional to $\mathbf{n}$, that we write as $\dot{\mathbf{x}} \propto \mathbf{n}$, iff there exists a $\lambda \in \mathbb{R}$ such that $\dot{\mathbf{x}} = \lambda \mathbf{n}$. Define

$$\mathcal{F}_0(\mathbf{p}, \dot{\mathbf{p}})^2 := \begin{cases} \mathcal{C}_1^2(\mathbf{p}) |\dot{\mathbf{x}} \cdot \mathbf{n}|^2 + \mathcal{C}_2^2(\mathbf{p}) \|\dot{\mathbf{n}}\|^2 & \text{if } \dot{\mathbf{x}} \propto \mathbf{n}, \\ +\infty & \text{otherwise.} \end{cases} \quad (2)$$

$$\mathcal{F}_0^+(\mathbf{p}, \dot{\mathbf{p}})^2 := \begin{cases} \mathcal{C}_1^2(\mathbf{p}) |\dot{\mathbf{x}} \cdot \mathbf{n}|^2 + \mathcal{C}_2^2(\mathbf{p}) \|\dot{\mathbf{n}}\|^2 & \text{if } \dot{\mathbf{x}} \propto \mathbf{n} \text{ and } \dot{\mathbf{x}} \cdot \mathbf{n} \geq 0, \\ +\infty & \text{otherwise.} \end{cases} \quad (3)$$

Here $\|\cdot\|$ denotes the norm and "$\cdot$" the dot product of the Euclidean space $\mathbb{R}^d$. The functions $\mathcal{C}_1$ and $\mathcal{C}_2$ are assumed to be continuous on $\mathbb{M}$, and uniformly bounded from below by a positive constant $\delta > 0$. In applications, $\mathcal{C}_1$ and $\mathcal{C}_2$ are chosen so as to favor paths which remain close to regions of interest, e.g. along blood vessels in retinal images. Note that their physical units are distinct: if one wishes $d_{\mathcal{F}}$ to have the dimension $[T]$ of

[1] We use the common terminology of Finsler metric, although $\mathcal{F}$ is sometimes called a Finsler function, since formally it is not a metric.

[2] In contrast to previous works [23,10,7,33,21] we parameterize such that the time integration stays on $[0, 1]$, and $t > 0$ is *not* a priori reserved (unless explicitly stated otherwise) for arclength parametrization (which satisfies $\mathcal{F}_{\boldsymbol{\gamma}(t)}(\dot{\boldsymbol{\gamma}}(t)) = 1$).

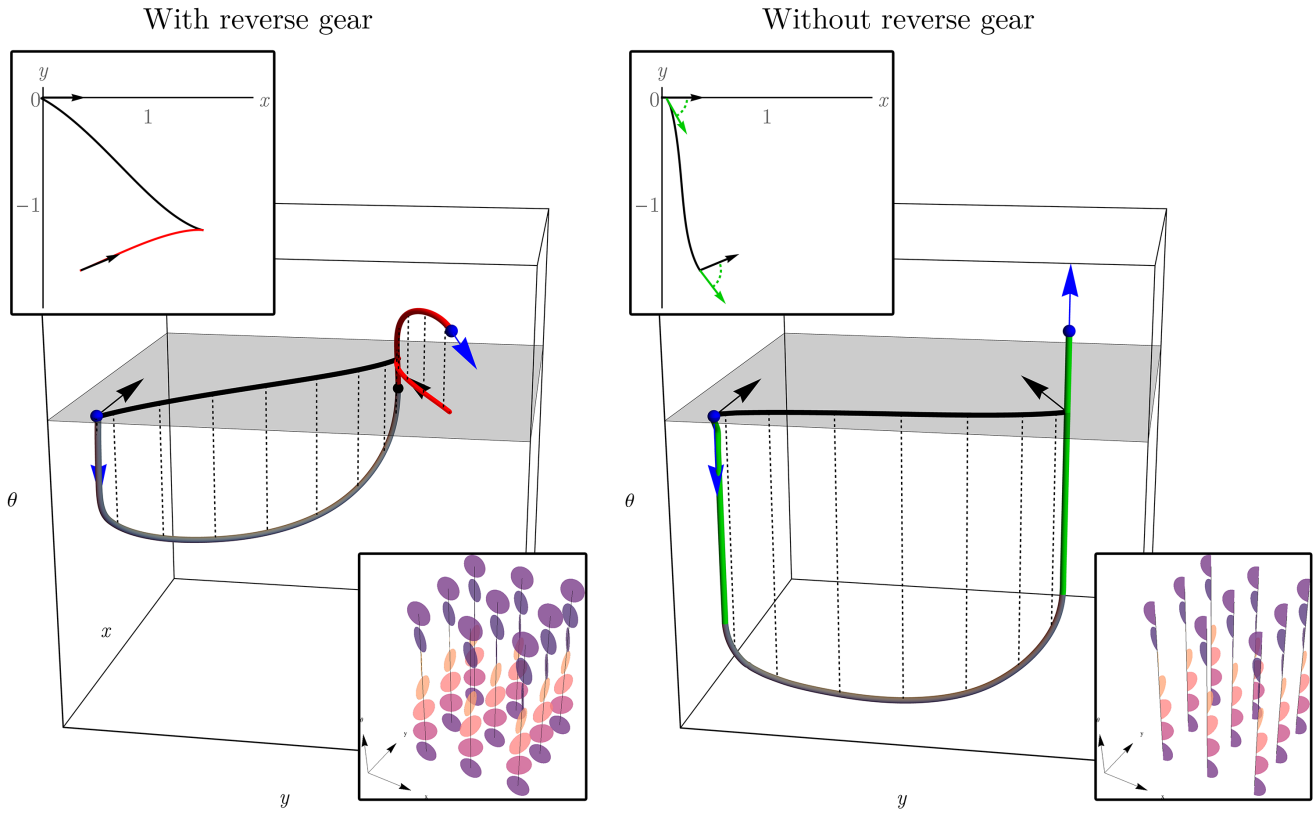

Fig. 1 Top: Example of a shortest path with (left) and without (right) reverse gear in $\mathbb{R}^2 \times S$ and its projection on $\mathbb{R}^2$. The black arrows indicate the begin and end condition in the plane. In the left figure, the projection of the path has a cusp, after which the line is covered backwards (the red part). On the right, backward motion is not possible. Instead, according to our model, the shortest path is a concatenation of an in-place rotation (green), a SR geodesic, and again an in-place rotation. Bottom: corresponding control sets as defined in (7) for the allowed velocities at each position and orientation, with $B_{\mathcal{F}_0}$ on the left and $B_{\mathcal{F}_0^+}$ on the right.

a travel time, then $\mathcal{C}_1^{-1}$ is a physical velocity $[L][T]^{-1}$, and $\mathcal{C}_2^{-1}$ is an angular velocity $[\mathrm{Rad}][T]^{-1}$. For simplicity one often sets $\mathcal{C}_1 = \xi\mathcal{C}_2$, where $\xi^{-1} > 0$ is a unit of length.

1.3 The eikonal equation and the fast marching algorithm

In the numerical part of the paper, we compute the distance map to a point source on a volume using the relation to eikonal equations. Let $\mathbf{p}_S \in \mathbb{M}$ be an arbitrary source point, and let U be the associated distance function

$$U(\mathbf{p}) := d_{\mathcal{F}}(\mathbf{p}_S, \mathbf{p}). \tag{4}$$

Then U is the unique viscosity solution [17,16] to the eikonal PDE:

$$\begin{cases} \mathcal{F}^*(\mathbf{p}, \mathrm{d}U(\mathbf{p})) = 1 & \text{for all } \mathbf{p} \in \mathbb{M} \setminus \{\mathbf{p}_S\}, \\ U(\mathbf{p}_S) = 0. \end{cases} \tag{5}$$

Here $\mathcal{F}^*$ is the dual metric of $\mathcal{F}$ and $\mathrm{d}U$ is the differential of the distance map U. However, for these relations to hold, $\mathcal{F}$ should be at least continuous. We therefore propose in Section 2.3 for both $\mathcal{F}_0$ and $\mathcal{F}_0^+$ an approximating metric, that we denote by $\mathcal{F}_\varepsilon$ and $\mathcal{F}_\varepsilon^+$, respectively, that are continuous and converge to $\mathcal{F}_0$ and $\mathcal{F}_0^+$ as $\varepsilon \to 0$. The approximating metrics correspond to a highly anisotropic Riemannian and Finslerian metric, rather than a sub-Riemannian or sub-Finslerian metric.

We design a monotone and causal discretization scheme for the static Hamilton-Jacobi PDE (5), which allows to apply efficient, single pass Fast-Marching Algorithm [53]. Let us emphasize that designing a causal discretization scheme for (5) is non-trivial, because its local connectivity needs to be obey an *acuteness property* [50,55] depending on the geometry defined by $\mathcal{F}$. We provide ad-hoc constructions for the metrics $\mathcal{F}_\varepsilon$ or $\mathcal{F}_\varepsilon^+$ of interest, based on the earlier works [37,38].

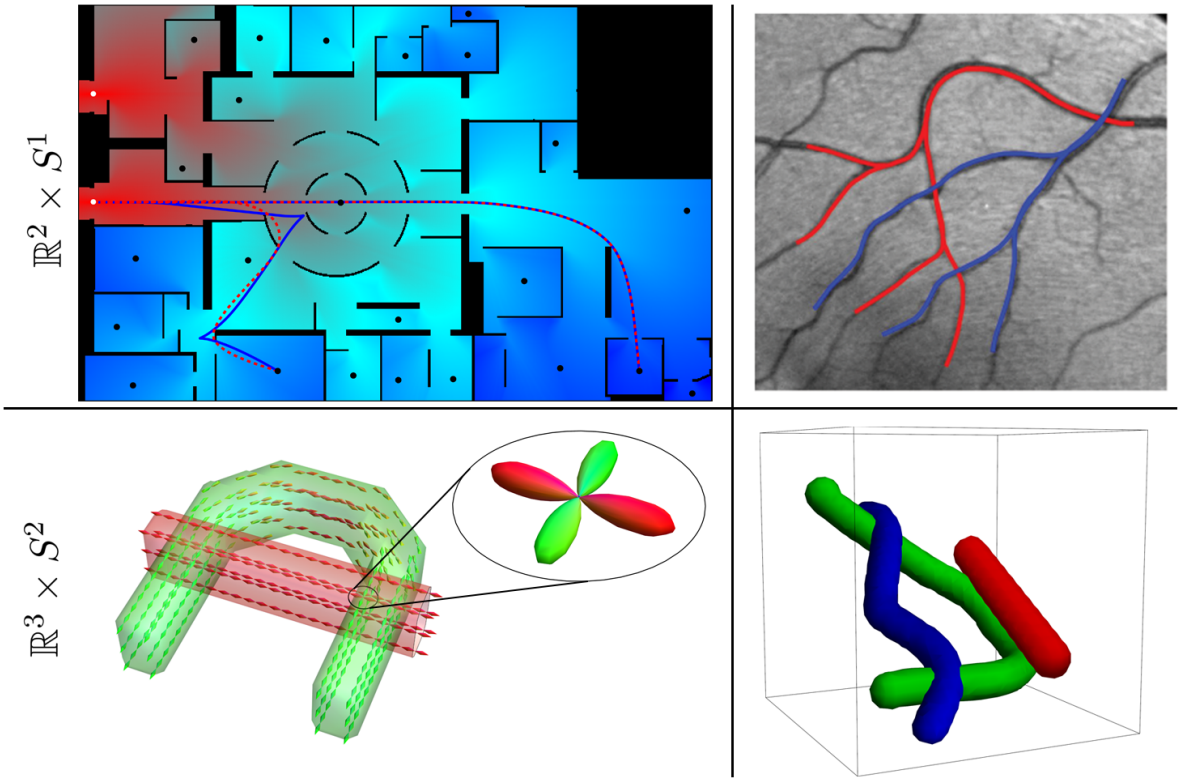

Fig. 2 Challenges and applications. Top row: the case $d = 2$, with a toy problem for finding the shortest way with or without reverse gear (blue and red, respectively) to the exit in Centre Pompidou (top left) and a vessel tracking problem in a retinal image. Bottom row: the case $d = 3$, connectivity in (simulated) dMRI data. Left: visualization of a dataset with two crossing bundles without torsion, with a glyph visualization of the data in $\mathbb{R}^3 \times S^2$ and a magnification of one such glyph, indicating two main fiber directions. Right: the spatial configuration in $\mathbb{R}^3$ of bundles with torsion in an artificial dataset on $\mathbb{R}^3 \times S^2$.

1.4 Shortest Paths and Minimal Distances in Medical Images

The application of the proposed method for finding shortest paths has been shown to be useful for vessel-tracking in retinal images [7], see Fig. 2 (top, right). A related approach using fast marching with elastica functionals can be found in [12,13]. The sub-Riemannian approach by Bekkers et al. [7] concerns the two-dimensional Reeds-Shepp car model with reverse gear, where 2D gray-scale images are first lifted to an orientation score defined on the higher dimensional manifold $\mathbb{R}^2 \times \mathbb{S}^1$. There, the combination of the sub-Riemannian metric, the cost function derived from the orientation score, and the numerical fast-marching solver, provided a solid approach to accurately track vessels in challenging sets of images.

For this reason, we apply the same strategy to diffusion-weighted MRI data. For such images, a signal related to the amount of diffusion is measured, which in the case of neuroimages is considered to be related to the underlying cell-structure. The images can in a natural way be considered to have domain $\Omega \subset \mathbb{R}^3 \times \mathbb{S}^2$. Fig. 2 (bottom) illustrates such images. On the left we use a glyph visualization, that shows a surface for each grid point, where the distance from the surface to the corresponding grid point $\mathbf{x}$ is proportional to the data-value $U(\mathbf{x}, \mathbf{n})$ and the coloring is related to the orientation $\mathbf{n} \in S^2$.

A large number of tractography methods exist, that are designed to estimate/approximate the fiber paths in the brain based on dMRI data. Most of these methods construct tracks that locally follow the structure of the data, see e.g. [52,19] or references in [31]. More related to our approach are geodesic methods, that have the advantage that they minimize a functional, and thereby are less sensitive to noise and provide a certain measure of connectivity between regions. These methods can be based on diffusion tensors in combination with Riemannian geometry on position space, e.g. [28,32, 30]. One can also make use of the more general Finsler geodesic tracking to include directionality [35,36], and use high angular resolution data (HARDI), examples of which can be found in [49,5]. Recently, a promising method has been proposed, based on geodesics on the full position and orientation space using a data-adaptive Riemannian metric [41]. We also work on this

joint space of positions and orientations, but use either Riemannian or asymmetric Finsler metrics that are highly anisotropic, that we solve by a numerical fast marching method that is able to deal with this high anisotropy. We show on artificial datasets how our method can be employed to give global minimizers between two regions w.r.t the imposed Finsler metric, and that these paths correctly follow the bundle structure.

1.5 Contributions and Outline

The extension to 3D of the Reeds-Shepp metric and the adaptation to model shortest paths for cars that cannot move backwards are new and provide an interesting collection of new theoretical and practical results:

- In Theorem 1 we show that the Reeds-Shepp model is globally and locally controllable, and that the Reeds-Shepp model without reverse gear is globally but not locally controllable. Hence the distance map loses continuity.
- We introduce regularizations $\mathcal{F}_\varepsilon$ and $\mathcal{F}_\varepsilon^+$ of the Reeds-Shepp metrics $\mathcal{F}_0$ and $\mathcal{F}_0^+$, which make our numerical discretization possible. We show that both the corresponding distances converge to $d_{\mathcal{F}_0}$ and $d_{\mathcal{F}_0^+}$ as $\varepsilon \to 0$ and the minimizing curves converge to the ones for $\varepsilon = 0$, see Theorem 2.
- We present and prove for $d = 2$ and uniform cost a theorem that describes the occurrence of cusps for the SR Reeds-Shepp model $\mathcal{F}_0$, and that using $\mathcal{F}_0^+$ leads to geodesics that are a concatenation of purely angular motion, a sub-Riemannian geodesic without cusps and again a purely angular motion. We call the positions where in-place rotation (or purely angular motion) takes place *keypoints*. For uniform cost, we show that the only possible keypoints are the begin and end point, and for many end conditions we can describe how this happens. The precise theoretical statement and proof are found in Theorem 3.
- Furthermore, we show in Theorem 4 how the geodesics can be obtained from the distance map, for a general Finsler metric, and in the more specific cases that we use in this paper. For our cases of interest, we show that backtracking of geodesics is either done via a single intrinsic gradient descent (for the models with reverse gear), or via two intrinsic gradient descents (for the model without reverse gear).
- For our numerical experiments we make use of a Fast-Marching implementation, for $d = 2$ introduced in [37]. In Section 6 we give a summary of the numerical approach for $d = 3$, but a detailed discussion of the implementation and an evaluation of the accuracy of the method is beyond the scope of this paper, and will follow in future work. For $d = 2$, we show an extensive comparison between the models with and without reverse gear for uniform cost, to illustrate the principle of the keypoints and to show that qualitative difference between the two models. In an example with non-uniform cost, see the top row of Fig. 2, we show that the model automatically places the keypoints at corners/bifurcations in the data, where the in-place rotation forms a natural 're-initialization' of the tracking.
  For $d = 3$, we give several examples to show the influence of the model parameters, in particular the cost parameter. The examples indicate that the method adequately deals with crossing or kissing structures.

Outline In Section 2, we give a detailed overview of the theoretical results of the paper. The theorems 1, 3 and 4 are discussed and proven in Sections 3, 4 and 5, respectively. The proof of Theorem 2 is given in Appendix A. We discuss the numerics briefly in Section 6. Section 7 contains all experimental results. Conclusion and discussion follow in Section 8.

2 Main results

In this section, we state formally the mathematical results announced in Section 1. Some preliminaries regarding the distance function are introduced in the Section below. Results regarding the exact Reeds-Shepp car models are gathered in Section 2.2. The description of the approximate models and the related convergence results appear in Section 2.3. Analysis of special interest points (cusps and keypoints) are done in Section 2.4. Results on the eikonal equation, and subsequent backtracking of optimal geodesics via intrinsic gradients is presented in Section 2.5.

2.1 Preliminaries on the (pseudo) Distance Function and Underlying Geometry

Geometries on the manifold of states $\mathbb{M} = \mathbb{R}^d \times \mathbb{S}^{d-1}$ are defined by means of Finsler metrics which are functions $\mathcal{F} : T(\mathbb{M}) \to [0, +\infty]$. On each tangent space, the metric should be 1-homogeneous, convex and quantitatively non-degenerate with a uniform constant $\delta > 0$: for all

$\mathbf{p} = (\mathbf{x}, \mathbf{n}) \in \mathbb{M}$, $\dot{\mathbf{p}}, \dot{\mathbf{p}}_0, \dot{\mathbf{p}}_1 \in T_{\mathbf{p}}(\mathbb{M})$, and $\lambda \geq 0$:

$$\begin{aligned} \mathcal{F}(\mathbf{p}, \lambda\dot{\mathbf{p}}) &= \lambda\mathcal{F}(\mathbf{p}, \dot{\mathbf{p}}), \\ \mathcal{F}(\mathbf{p}, \dot{\mathbf{p}}_0 + \dot{\mathbf{p}}_1) &\leq \mathcal{F}(\mathbf{p}, \dot{\mathbf{p}}_0) + \mathcal{F}(\mathbf{p}, \dot{\mathbf{p}}_1), \\ \mathcal{F}(\mathbf{p}, \dot{\mathbf{p}}) &\geq \delta\sqrt{\|\dot{\mathbf{x}}\|^2 + \|\dot{\mathbf{n}}\|}. \end{aligned} \tag{6}$$

A weak regularity property is required as well, see the next remark. The induced distance $d_{\mathcal{F}}$, defined in (1), obeys $d_{\mathcal{F}}(\mathbf{p}, \mathbf{q}) = 0$ iff $\mathbf{p} = \mathbf{q}$, and obeys the triangular inequality. However, unlike a regular distance, $d_{\mathcal{F}}$ needs not be finite, or continuous, or symmetric in its arguments. Note that $\mathcal{F}_0$ and $\mathcal{F}_0^+$ as defined in (2) and (3), respectively, indeed satisfy the properties in (6).

Remark 1 In contrast to the more common definition of Finsler metrics, we will *not* assume the Finsler metric to be smooth on $T(\mathbb{M})$, but use a weaker condition instead. Following [18], we require that the sets

$$\mathcal{B}_{\mathcal{F}}(\mathbf{p}) := \{\dot{\mathbf{p}} \in T_{\mathbf{p}}\mathbb{M} \,|\, \mathcal{F}(\mathbf{p}, \dot{\mathbf{p}}) \leq 1\} \tag{7}$$

are closed and vary continuously with respect to the point $\mathbf{p} \in \mathbb{M}$ in the sense of the Haussdorff distance. The sets $\mathcal{B}_{\mathcal{F}}(\mathbf{p})$ are illustrated on Fig. 1 for the models of interest. The condition implies that a minimal path exists from $\mathbf{p}$ to $\mathbf{q} \in \mathbb{M}$ whenever $d_{\mathcal{F}}(\mathbf{p}, \mathbf{q})$ is finite, and is used to prove convergence results in Appendix A.

A common technique in optimal control theory is to reformulate the shortest path problem defining the distance $d_{\mathcal{F}}(\mathbf{p}, \mathbf{q})$ into a time optimal control problem. That is, for $p \in [1, \infty]$ one has by Hölder's (in)equality, time re-parametrization, and 1-homogeneity of $\mathcal{F}$ in its 2nd entry, that:

$$\begin{aligned} &d_{\mathcal{F}}(\mathbf{p}, \mathbf{q}) = \\ &= \inf\{\int_0^1 \mathcal{F}(\gamma(t), \dot{\gamma}(t))\,\mathrm{d}t \mid \gamma \in \Gamma,\ \gamma(0) = \mathbf{p}, \gamma(1) = \mathbf{q}\} \\ &= \inf\{\left(\int_0^1 |\mathcal{F}(\gamma(t), \dot{\gamma}(t))|^p\,\mathrm{d}t\right)^{1/p} \mid \gamma \in \Gamma,\ \ldots\} \\ &= \inf\{T \geq 0 \ \mid\ \exists \gamma \in \Gamma_T,\ \gamma(0) = \mathbf{p}, \\ &\qquad \gamma(T) = \mathbf{q}, \forall_{t\in[0,T]}\, \dot{\gamma}(t) \in \mathcal{B}_{\mathcal{F}}(\gamma(t))\}, \end{aligned} \tag{8, 9}$$

where $\Gamma_T := \mathrm{Lip}([0, T], \mathbb{M})$, and with $\mathcal{B}_{\mathcal{F}}(\mathbf{p})$ as defined in (7). The latter reformulation is used in Appendix A to prove convergence results via closedness of controllable paths and Arzela-Ascoli's theorem, based on a general result originally applied to Euler elastica curves in [18].

In the special case $\mathcal{F} = \mathcal{F}_0$ the geodesics are SR geodesics. If $\mathcal{F} = \mathcal{F}_0$ the Finsler function is obtained by the square root of quadratic form associated to a SR metric $\mathcal{G}_0|_{\mathbf{p}}(\cdot, \cdot) = \mathcal{F}_0(\mathbf{p}, \cdot)^2$ on a SR manifold $(\mathbb{M}, \Delta, \mathcal{G}_0)$, where $\Delta \subset T(\mathbb{M})$ is a strict subset of allowable tangent vectors that comes along with the horizontality constraint

$$\dot{\mathbf{x}}(t) = (\dot{\mathbf{x}}(t) \cdot \mathbf{n}(t))\mathbf{n}(t), \qquad \forall t \in [0, 1], \tag{10}$$

that arises from (2).

Finally, we note that for the uniform cost case $\mathcal{C}_1 = \mathcal{C}_2 = 1$, the problem is covariant with respect to rotations and translations. For the data-driven case, such covariance is only obtained when simultaneously rotating the data-driven cost factors $\mathcal{C}_1, \mathcal{C}_2$. Therefore, only in the uniform cost case, for $d = 2, 3$, we shall use a reference point ('the origin') $\mathbf{e} \in \mathbb{R}^d \times S^{d-1}$. To adhere to common conventions we use

$$\begin{aligned} &\mathbf{e} = (\mathbf{0}, \mathbf{a}) \in \mathbb{R}^d \times S^{d-1}, \text{ with} \\ &\qquad \mathbf{a} := (1, 0)^T \qquad \text{if } d = 2 \text{ and} \\ &\qquad \mathbf{a} := (0, 0, 1)^T \quad \text{if } d = 3. \end{aligned} \tag{11}$$

2.2 Controllability of the Reeds-Shepp model

A model $(\mathbb{M}, \mathcal{F})$ is globally controllable if the distance $d_{\mathcal{F}}$ takes finite values on $\mathbb{M} \times \mathbb{M}$. In Theorem 1 we show that this is indeed the case for $\mathcal{F} = \mathcal{F}_0$ and $\mathcal{F} = \mathcal{F}_0^+$. Local controllability is satisfied when $d_{\mathcal{F}}$ satisfies a certain continuity requirement: if $\mathbf{p} \to \mathbf{q} \in (\mathbb{M}, \|\cdot\|)$, with $\|\cdot\|$ denoting the standard (flat) Euclidean norm on $\mathbb{M} = \mathbb{R}^d \times \mathbb{S}^{d-1}$, we must have $d_{\mathcal{F}}(\mathbf{p}, \mathbf{q}) \to 0$. We prove in Theorem 1 that $(\mathbb{M}, \mathcal{F}_0)$ is locally controlabble, but $(\mathbb{M}, \mathcal{F}_0^+)$ is not. Indeed the SR Reeds-Shepp car can achieve sideways motions by alternating the forward and reverse gear with slight direction changes, whereas the model without reverse gear lacks this possibility. For completeness, the theorem contains a standard (rough) estimate of the distance near the source point (due to well-known estimates [29,51,14,43]).

Furthermore, we prove existence of minimizers for the Reeds-Shepp model without reverse gear. Existence results of minimizers of the model with reverse gear (the SR model) already exist, by the Chow-Rashevski theorem and Fillipov theorems [2].

Theorem 1 ((Local) controllability properties) *Minimizers exist for both the classical Reeds-Shepp model, and for the Reeds-Shepp model without reverse gear. Both models are globally controllable.*

- *The Reeds-Shepp model without reverse gear is not locally controllable, since*

$$\limsup_{\mathbf{p}' \to \mathbf{p}} d_{\mathcal{F}_0^+}(\mathbf{p}, \mathbf{p}') \geq 2\pi\delta, \text{ for all } \mathbf{p} \in \mathbb{M}. \tag{12}$$

If the cost $\mathcal{C}_2 = \delta$ is constant on $\mathbb{M}$, then this inequality is sharp

$$\limsup_{\mathbf{p}'\to\mathbf{p}} d_{\mathcal{F}_0^+}(\mathbf{p},\mathbf{p}') = \lim_{\mu\downarrow 0} d_{\mathcal{F}_0^+}((\mathbf{x},\mathbf{n}),(\mathbf{x}-\mu\mathbf{n},\mathbf{n})) = 2\pi\delta. \tag{13}$$

– *The sub-Riemannian Reeds-Shepp model is locally controllable, since*

$$d_{\mathcal{F}_0}(\mathbf{p},\mathbf{p}') = \mathcal{O}\left(\mathcal{C}_2(\mathbf{p})\|\mathbf{n}-\mathbf{n}'\| + \sqrt{\mathcal{C}_2(\mathbf{p})\mathcal{C}_1(\mathbf{p})\|\mathbf{x}-\mathbf{x}'\|}\right) \quad \text{as } \mathbf{p}' = (\mathbf{x}',\mathbf{n}') \to \mathbf{p} = (\mathbf{x},\mathbf{n}). \tag{14}$$

For a proof see Section 3.

2.3 A Continuous Approximation for the Reeds-Shepp geometry

We introduce approximations $\mathcal{F}_\varepsilon$ and $\mathcal{F}_\varepsilon^+$ of the Reeds-Shepp metrics $\mathcal{F}_0$ and $\mathcal{F}_0^+$, depending on a small parameter $0 < \varepsilon \leq 1$, which are continuous and in particular take only finite values. This is a prerequisite for our numerical methods. Both approximations penalize the deviation from the constraints of collinearity $\dot{\mathbf{x}} \propto \mathbf{n}$, and in addition, $\mathcal{F}_\varepsilon^+$ penalizes negativity of the scalar product $\dot{\mathbf{x}}\cdot\mathbf{n}$, appearing in (2) and (3). For that purpose, we introduce some additional notation: for $\dot{\mathbf{x}} \in \mathbb{R}^d$ and $\mathbf{n} \in \mathbb{S}^{d-1}$

$$\begin{aligned} \|\dot{\mathbf{x}}\wedge\mathbf{n}\|^2 &:= \|\dot{\mathbf{x}}\|^2 - |\dot{\mathbf{x}}\cdot\mathbf{n}|^2, \\ (\dot{\mathbf{x}}\cdot\mathbf{n})_- &:= \min\{0, \dot{\mathbf{x}}\cdot\mathbf{n}\}, \\ (\dot{\mathbf{x}}\cdot\mathbf{n})_+ &:= \max\{\dot{\mathbf{x}}\cdot\mathbf{n}, 0\}. \end{aligned} \tag{15}$$

These are respectively the norm of the orthogonal projection[3] of $\dot{\mathbf{x}}$ onto the plane orthogonal to $\mathbf{n}$, and the negative and positive parts of their scalar product. The two metrics $\mathcal{F}_\varepsilon, \mathcal{F}_\varepsilon^+ : T(\mathbb{M}) \to \mathbb{R}_+$ are defined for each $0 < \varepsilon \leq 1$, as follows: for $(\mathbf{p},\dot{\mathbf{p}}) \in T(\mathbb{M})$ with components $\mathbf{p} = (\mathbf{x},\mathbf{n})$ and $\dot{\mathbf{p}} = (\dot{\mathbf{x}},\dot{\mathbf{n}})$

$$\mathcal{F}_\varepsilon(\mathbf{p},\dot{\mathbf{p}})^2 := \mathcal{C}_1(\mathbf{p})^2(|\dot{\mathbf{x}}\cdot\mathbf{n}|^2 + \varepsilon^{-2}\|\dot{\mathbf{x}}\wedge\mathbf{n}\|^2) + \mathcal{C}_2(\mathbf{p})^2\|\dot{\mathbf{n}}\|^2, \tag{16}$$

$$\begin{aligned} \mathcal{F}_\varepsilon^+(\mathbf{p},\dot{\mathbf{p}})^2 &:= \mathcal{C}_1(\mathbf{p})^2(|\dot{\mathbf{x}}\cdot\mathbf{n}|^2 + \varepsilon^{-2}\|\dot{\mathbf{x}}\wedge\mathbf{n}\|^2 + (\varepsilon^{-2}-1)(\dot{\mathbf{x}}\cdot\mathbf{n})_-^2) + \mathcal{C}_2(\mathbf{p})^2\|\dot{\mathbf{n}}\|^2 \qquad (17) \\ &= \mathcal{C}_1(\mathbf{p})^2((\dot{\mathbf{x}}\cdot\mathbf{n})_+^2 + \varepsilon^{-2}\|\dot{\mathbf{x}}\wedge\mathbf{n}\|^2 + \varepsilon^{-2}(\dot{\mathbf{x}}\cdot\mathbf{n})_-^2) + \mathcal{C}_2(\mathbf{p})^2\|\dot{\mathbf{n}}\|^2. \qquad (18) \end{aligned}$$

See Fig. 3 for a visualization of a levelset of both metrics in $\mathbb{R}^2\times S^1$. Note that $\mathcal{F}_\varepsilon$ is a Riemannian metric on $\mathbb{M}$ (with the same smoothness as the cost functions $\mathcal{C}_2, \mathcal{C}_1$), and that $\mathcal{F}_\varepsilon^+$ is neither Riemannian nor smooth due to the term $(\dot{\mathbf{x}}\cdot\mathbf{n})_-$. One clearly has the pointwise convergence $\mathcal{F}_\varepsilon(\mathbf{p},\dot{\mathbf{p}}) \to \mathcal{F}_0(\mathbf{p},\dot{\mathbf{p}})$ as $\varepsilon \to 0$, and likewise $\mathcal{F}_\varepsilon^+(\mathbf{p},\dot{\mathbf{p}}) \to \mathcal{F}_0^+(\mathbf{p},\dot{\mathbf{p}})$. The use of $\mathcal{F}_\varepsilon$ and $\mathcal{F}_\varepsilon^+$ is further justified by the following convergence result.

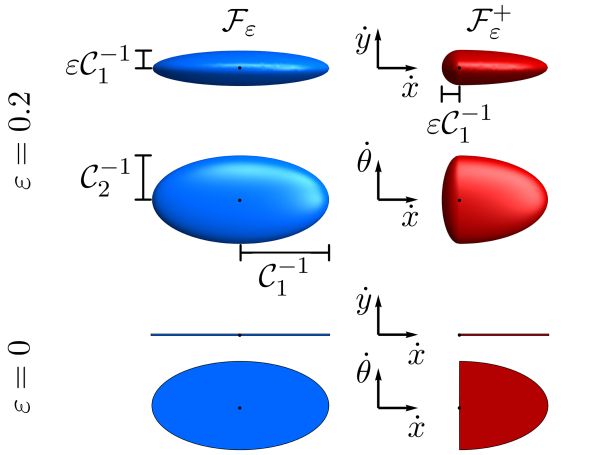

Fig. 3 Levelsets for $d = 2$ of the (approximating) metrics $\mathcal{F}_\varepsilon(\mathbf{0},(\dot{x},\dot{y},\dot{\theta})) = 1$ (left) and $\mathcal{F}_\varepsilon^+(\mathbf{0},(\dot{x},\dot{y},\dot{\theta})) = 1$ (right), with $\varepsilon = 0.2$ (top) and $\varepsilon = 0$ (bottom). In this example, $\mathcal{C}_2(\mathbf{0}) = 2\mathcal{C}_1(\mathbf{0})$.

Theorem 2 (Convergence of the Approximative Models to the Exact Models) *One has the pointwise convergence: for any $\mathbf{p},\mathbf{q} \in \mathbb{M}$*

$$\begin{aligned} d_{\mathcal{F}_\varepsilon}(\mathbf{p},\mathbf{q}) &\to d_{\mathcal{F}_0}(\mathbf{p},\mathbf{q}), \\ d_{\mathcal{F}_\varepsilon^+}(\mathbf{p},\mathbf{q}) &\to d_{\mathcal{F}_0^+}(\mathbf{p},\mathbf{q}), \end{aligned} \quad \text{as } \varepsilon \to 0.$$

Consider for each $\varepsilon > 0$ a minimizing path γ_ε^* from $\mathbf{p}$ to $\mathbf{q}$, with respect to the metric $\mathcal{F}_\varepsilon$, parametrized at constant speed

$$\mathcal{F}_\varepsilon(\gamma_\varepsilon^*(t),\dot{\gamma}_\varepsilon^*(t)) = d_{\mathcal{F}_\varepsilon}(\mathbf{p},\mathbf{q}), \qquad \forall t \in [0,1].$$

Assume that there is a unique minimal path γ^* from $\mathbf{p}$ to $\mathbf{q}$ with respect to the sub-Riemannian distance $d_{\mathcal{F}_0}$ (in other words $\mathbf{q}$ is not within the cut locus of $\mathbf{p}$), parametrized at constant speed:

$$\mathcal{F}_0(\gamma^*(t),\dot{\gamma}^*(t)) = d_{\mathcal{F}_0}(\mathbf{p},\mathbf{q}), \qquad \forall t \in [0,1].$$

Then $\gamma_\varepsilon^* \to \gamma^*$ as $\varepsilon \to 0$, uniformly on $[0,1]$. Likewise replacing $\mathcal{F}_\varepsilon$ with $\mathcal{F}_\varepsilon^+$ for all $\varepsilon \geq 0$.

The proof, presented in Appendix A is based on a general result originally applied to the Euler elastica curves in [18]. Combining Theorem 2 with the local controllability properties established in Theorem 1, one obtains that $d_{\mathcal{F}_\varepsilon} \to d_{\mathcal{F}_0}$ locally uniformly on $\mathbb{M}\times\mathbb{M}$, and that the convergence $d_{\mathcal{F}_\varepsilon^+} \to d_{\mathcal{F}_0^+}$ is only pointwise.

[3] The quantity $\|\dot{\mathbf{x}}\wedge\mathbf{n}\|$ is also the norm of the wedge product of $\dot{\mathbf{x}}$ and $\mathbf{n}$, but defining it this way would require introducing some algebra which is not needed in the rest of this paper.

Remark 2 If there exists not a single, but a family of minimal geodesics $(\gamma_i^*)_{i\in I}$ from $\mathbf{p}$ to $\mathbf{q}$ with respect to $\mathcal{F}_0$ (resp. $\mathcal{F}_0^+$), then one can show nevertheless that for any sequence $\varepsilon_n \to 0$ one can find a subsequence and an index $i \in I$ such that $\gamma^*_{\varepsilon_{\varphi(n)}} \to \gamma_i^*$ uniformly as $n \to \infty$.

2.4 Points of Interest in Spatial Projections of Geodesics for the Uniform Cost Case: Cusps vs. Keypoints

Next we provide a theorem that tells us in each of the models/metric spaces $(\mathbb{M}, d_{\mathcal{F}_0})$, $(\mathbb{M}, d_{\mathcal{F}_\varepsilon})$ and $(\mathbb{M}, d_{\mathcal{F}_0^+})$, $(\mathbb{M}, d_{\mathcal{F}_\varepsilon^+})$, with $\mathcal{C}_1 = \mathcal{C}_2 = 1$ and $d = 2$ where cusps occur in spatial projections of geodesics or where keypoints with in-place rotations take place.

Definition 2 (Cusp) A cusp point $\mathbf{x}(t_0)$ on a spatial projection of a (SR-)geodesic $t \mapsto (\mathbf{x}(t), \mathbf{n}(t))$ in $\mathbb{M}$ is a point where

$$\tilde{u}(t_0) = 0, \text{ and } \dot{\tilde{u}}(t_0) \neq 0, \text{where } \forall t,\ \tilde{u}(t) := \mathbf{n}(t) \cdot \dot{\mathbf{x}}(t)$$

i.e. a point where the spatial control aligned with $\mathbf{n}(t_0)$ vanishes and switches sign locally.

Although this definition explains the notion of a cusp geometrically (as can be observed in Fig. 1 and Fig. 4), it contains a redundant part for the relevant case of interest: the second condition automatically follows when considering the SR geodesics in $(\mathbb{M}, d_{\mathcal{F}_0})$. The following lemma gives a characterization of a cusp point in terms of the distance function along a curve.

Lemma 1 *Consider a SR-geodesic* $\gamma = (\mathbf{x}, \mathbf{n}) : [0,1] \to (\mathbb{M}, d_{\mathcal{F}_0})$*, parametrized at constant speed, and which physical position* $\mathbf{x}(\cdot)$ *is not identically constant. Denote* $\mathbf{p}_S := \gamma(0)$ *and* $U(\cdot) := d_{\mathcal{F}_0}(\mathbf{p}_S, \cdot)$*. Let* $t_0 \in (0,1)$ *be such that* U *is differentiable at* $\gamma(t_0) = (\mathbf{x}(t_0), \mathbf{n}(t_0))$*. Then*

$$\begin{aligned} \mathbf{x}(t_0) \text{ is a cusp point } &\Leftrightarrow \mathbf{n}(t_0) \cdot \dot{\mathbf{x}}(t_0) = 0 \\ &\Leftrightarrow \mathbf{n}(t_0) \cdot \nabla_{\mathbb{R}^d} U(\mathbf{x}(t_0), \mathbf{n}(t_0)) = 0. \end{aligned} \tag{19}$$

The proof can be found in Appendix D.

Definition 3 (Keypoint) A point $\tilde{\mathbf{x}}$ on the spatial projection of a geodesic $\gamma(\cdot) = (\mathbf{x}(\cdot), \mathbf{n}(\cdot))$ in $\mathbb{M}$ is a keypoint of γ if there exist $t_0 < t_1$, such that $\mathbf{x}(t) = \tilde{\mathbf{x}}$ and $\dot{\mathbf{n}}(t) \neq 0$ for all $t \in [t_0, t_1]$, i.e., a point where an in-place rotation takes place.

Definition 4 We define the set $\mathfrak{R} \subset \mathbb{M}$ to be all endpoints that can be reached with a geodesic $\gamma^* : [0,1] \to \mathbb{M}$ in $(\mathbb{M}, d_{\mathcal{F}_0})$ whose spatial control $\tilde{u}(t)$ stays positive for all $t \in [0,1]$.

Remark 3 The word 'geodesic' in this definition can (in the case $d = 2$) be replaced by 'globally minimizing geodesic' [10]. For a definition in terms of the exponential map of a geometrical control problem $\mathbf{P}_{curve}$, see e.g. [21,24], in which the same positivity condition for $\tilde{u}$ is imposed. Fig. 5 shows more precisely what this set looks like for $d = 2$ [21], in particular that it is contained in the half-space $\mathbf{a} \cdot \mathbf{x} \geq 0$, and for $d = 3$ [24]. We extend these results with the following theorem.

Theorem 3 (Cusps and Keypoints) *Let* $\varepsilon > 0$*,* $d = 2$*,* $\mathcal{C}_1 = \mathcal{C}_2 = 1$*. Then,*

- *in* $(\mathbb{M}, d_{\mathcal{F}_0})$ *cusps are present in spatial projections of almost every optimal SR geodesics when their times* t *are extended on the real line until they reach their cut-time. In fact, the straight-lines connecting specific boundary points* $\mathbf{p} = (\mathbf{x}, \mathbf{n})$ *and* $\mathbf{q} = (\mathbf{x} + \lambda \mathbf{n}, \mathbf{n})$ *with* $\lambda \in \mathbb{R}$ *are the only exceptions.*
- *in* $(\mathbb{M}, d_{\mathcal{F}_\varepsilon^+})$ *and* $(\mathbb{M}, d_{\mathcal{F}_\varepsilon})$ *and* $(\mathbb{M}, d_{\mathcal{F}_0^+})$ *no cusps appear in spatial projections of geodesics.*

Furthermore,

- *in* $(\mathbb{M}, d_{\mathcal{F}_0})$*,* $(\mathbb{M}, d_{\mathcal{F}_\varepsilon})$ *and* $(\mathbb{M}, d_{\mathcal{F}_\varepsilon^+})$ *keypoints only occur with vertical geodesics (moving only angularly).*
- *in* $(\mathbb{M}, d_{\mathcal{F}_0^+})$ *keypoints only occur at the endpoints of minimal paths.*

An optimal geodesic γ_+ *in* $(\mathbb{M}, d_{\mathcal{F}_0^+})$ *departing from* $\mathbf{e} = (0,0,0)$ *and ending in* $\mathbf{p} = (x, y, \theta)$ *has*

A) no keypoint if $\mathbf{p} \in \overline{\mathfrak{R}}$*,*
B) a keypoint in $(0,0)$ *if* $x < 0$*,*
C) a keypoint only *in* (x, y) *if*[4]
  C1) $\mathbf{p} \in \overline{\mathfrak{R}}^c$ *and* $x \geq 2$*,*
  C2) $\mathbf{p} \in \overline{\mathfrak{R}}^c$ *and* $0 \leq x < 2$ *and*
  $|y| \leq -ix\, E\left(i \operatorname{arcsinh}\left(\frac{x}{\sqrt{4-x^2}}\right), \frac{x^2-4}{x^2}\right)$*, where* $E(z,m)$ *denotes the Elliptic integral of the second kind.*

Remark 4 In case A, γ_+ is an optimal geodesic in $(\mathbb{M}, d_{\mathcal{F}_0})$ as well. In case B, γ_+ departs from a cusp. In case C, γ^+ is a concatenation of an optimal geodesic in $(\mathbb{M}, d_{\mathcal{F}_0})$ and an in-place rotation. For other endpoints (x, y, θ) for geodesics departing from $\mathbf{e}$ with $0 \leq x < 2$, other than the ones reported in C2 it is not immediately clear what happens, due to [21, Thm.9]. Also points with $x < 0$ may have keypoints at the end as well. See Fig. 6 where various cases of minimizing geodesics in $(\mathbb{M}, d_{\mathcal{F}_0^+})$ are depicted.

[4] Here $\overline{\mathfrak{R}}^c = \mathbb{M} \setminus \overline{\mathfrak{R}}$ denotes the complement of the closure $\overline{\mathfrak{R}}$ of $\mathfrak{R}$, and $E(z,m) = \int_0^z \sqrt{1 - m \sin^2 v}\, \mathrm{d}v$.

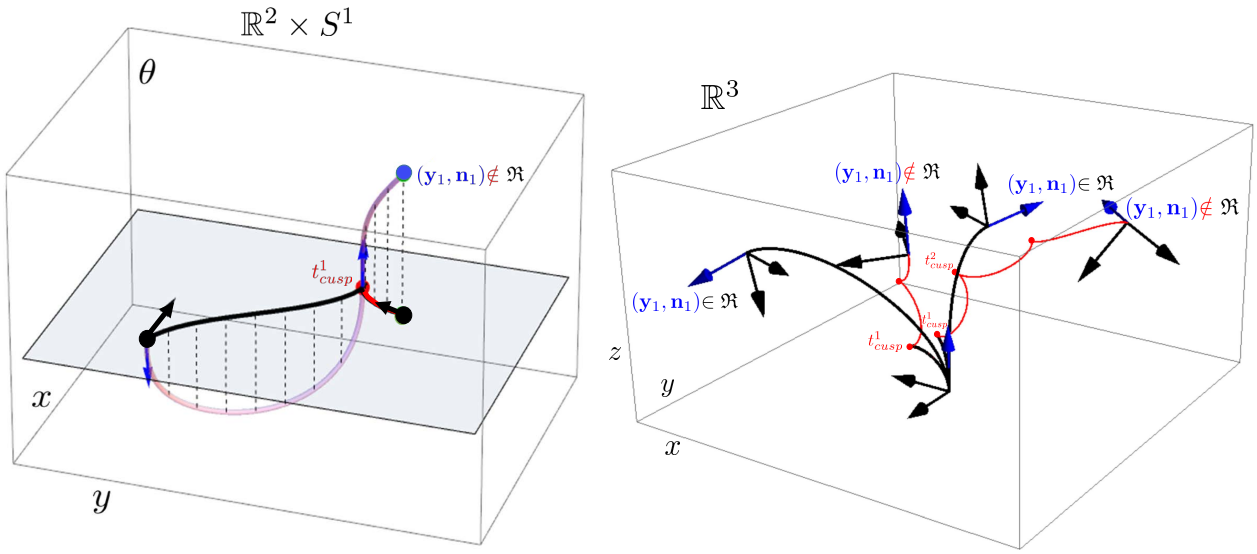

Fig. 4 Illustration of cusps in symmetric distance minimizers in $\mathbb{M} = \mathbb{R}^d \times S^{d-1}$. Left: cusps in spatial projections $\mathbf{x}(\cdot)$ of symmetric SR distance ($\varepsilon = 0$) minimizers $\boldsymbol{\gamma}(\cdot) = (\mathbf{x}(\cdot), \mathbf{n}(\cdot))$ for $d = 2$, right: cusps (red dots) appearing in spatial projections of symmetric SR distance geodesics for $d = 3$. In the 3D case we indicate the corresponding rotations $\mathbf{R}_{\mathbf{n}_1}$ via a local 3D frame.

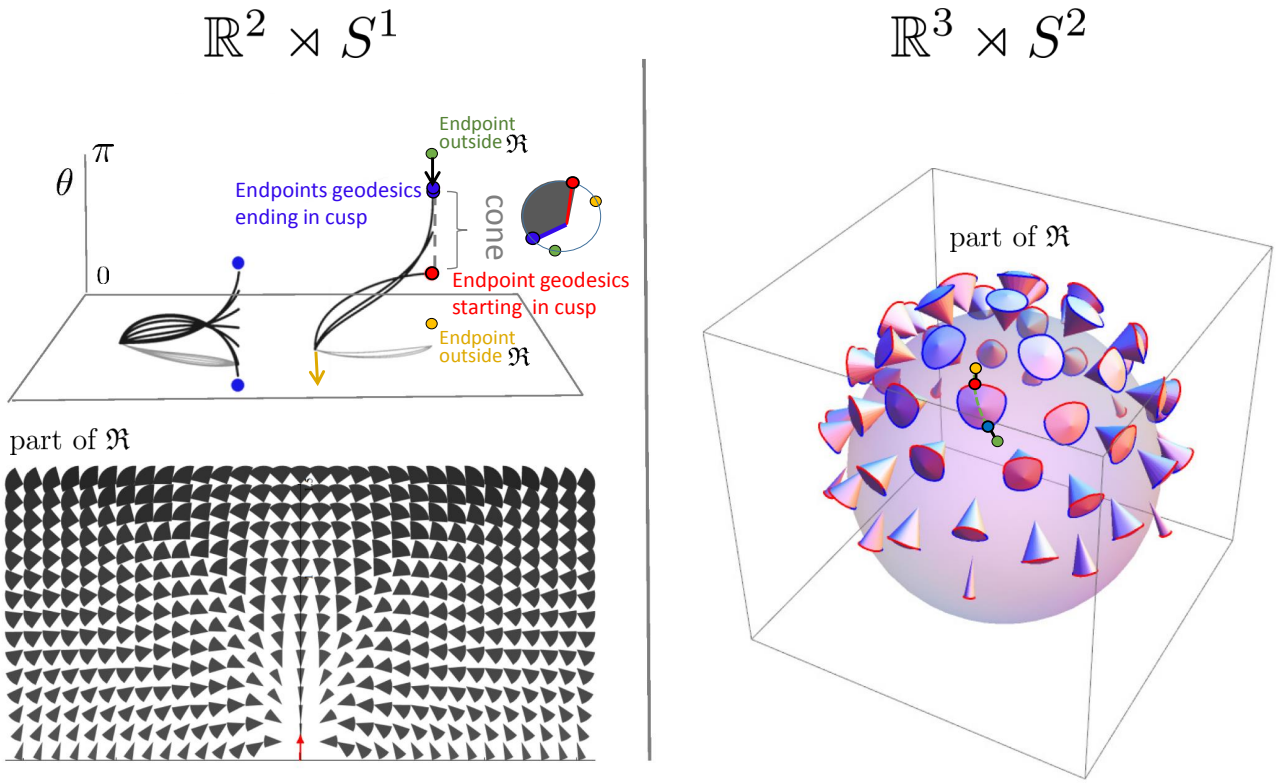

Fig. 5 The set $\mathfrak{R}$ of endpoints reachable from the origin $\mathbf{e}$ (recall (11)) via SR geodesics whose spatial projections do not exhibit cusps has been studied for the case $d = 2$ (left), and for the case $d = 3$ (right). For $d = 2$ it is contained in $x \geq 0$ and for $d = 3$ it is contained in $z \geq 0$. The boundary of this set contains of endpoints of geodesics departing at a cusp (in red) or of endpoints of geodesics ending in a cusp (in blue). If an endpoint $(\mathbf{x}, \mathbf{n})$ is placed outside $\mathfrak{R}$ (e.g. the green points above) then following the approach in Theorem 4, depending on its initial spatial location it first connects to a blue point $(\mathbf{x}, \mathbf{n}_{new})$ via a spherical geodesic end then connects to the origin $\mathbf{e}$ via a SR geodesic. Then it has a keypoint at the endpoint. For other locations spatial locations (orange points), the geodesic has the keypoint in the origin, or even at both boundaries, cf. Fig. 6.

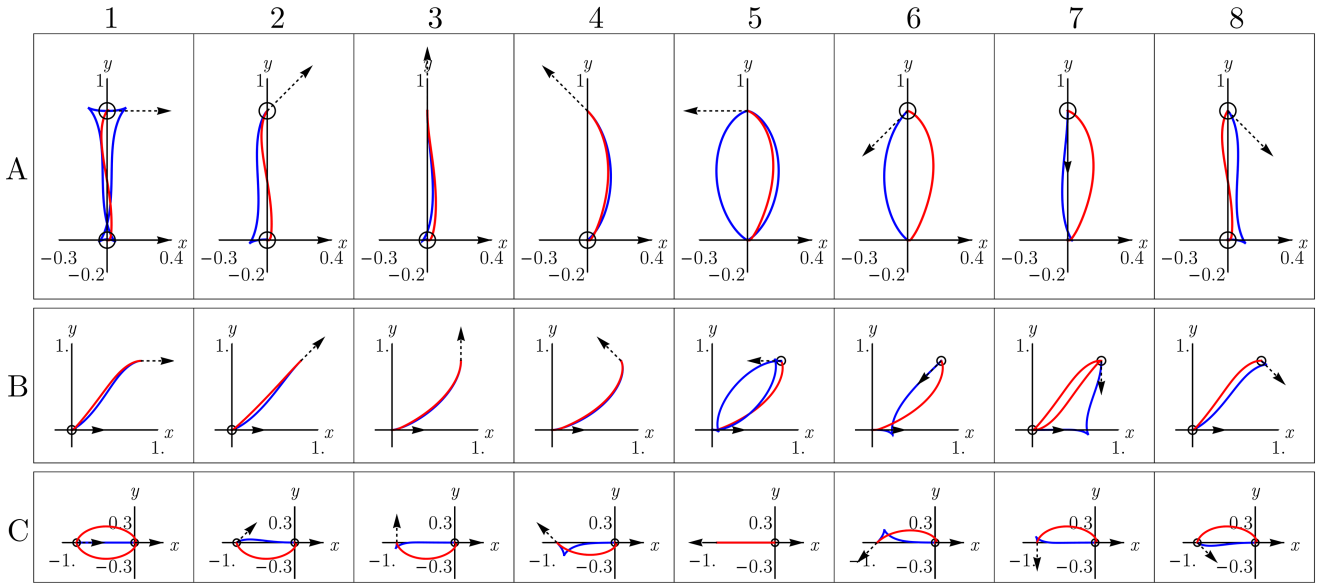

Fig. 6 Shortest paths for $d = 2$ using the Finsler functions $\mathcal{F}_0$ (blue) and $\mathcal{F}_0^+$ (red), with point source $\mathbf{p}_S = (0,0,0)$ and varying end conditions. Row A: $\mathbf{p} = (0, 0.8, \pi n/4)$. Row B: $\mathbf{p} = (0.8, 0.8, \pi n/4)$. Row C: $\mathbf{p} = (-0.8, 0, \pi n/4)$. Here $n = 1, \ldots, 8$, corresponding to the columns. When there are two optimal geodesics, both are drawn. Circles around the begin or end point indicate in-place rotation of the red curve at that point. We see that whenever the blue geodesic has a cusp, the red geodesic has at least one in-place rotation (keypoint). This numerically supports our statements in Theorem 3 considering cusps and keypoints. For high accuracy we applied the relatively slow iterative PDE approach [7] on a $101 \times 101 \times 64$-grid in $\mathbb{M}$ to compute $d_{\mathcal{F}_0}(\mathbf{p}, \mathbf{p}_S)$ and $d_{\mathcal{F}_0^+}(\mathbf{p}, \mathbf{p}_S)$, see Appendix B.

Remark 5 It is also interesting to study the effect of $\varepsilon \geq 0$ on the removal (or rather smoothing out in practice) of cusps on *non-optimal* geodesics in $(\mathbb{M}, d_{\mathcal{F}_\varepsilon})$ and keypoints in $(\mathbb{M}, d_{\mathcal{F}_\varepsilon^+})$ when ε moves away from 0. See Fig. 7, where such non-optimal geodesics are obtained via Euler-Lagrange formalism (or equivalently by integration of the canonical equations in the Pontryagin Maximum principle).

2.5 The Eikonal PDE Formalism

As briefly discussed in Section 1.3, continuous metrics like $\mathcal{F}_\varepsilon$ and $\mathcal{F}_\varepsilon^+$ for any $\varepsilon > 0$, allow to use the standard theory of viscosity solutions of eikonal PDEs, and thus to design provable and efficient numerical schemes for the computation of distance maps and minimal geodesics. More precisely, consider a continuous Finsler function $\mathcal{F} \in C^0(T(\mathbb{M}), \mathbb{R}^+)$, and define the dual Finsler function $\mathcal{F}^*$ on the co-tangent bundle as follows: for all $(\mathbf{p}, \hat{\mathbf{p}}) \in T^*(\mathbb{M})$

$$\mathcal{F}^*(\mathbf{p}, \hat{\mathbf{p}}) := \sup_{\dot{\mathbf{p}} \in T_{\mathbf{p}}\mathbb{M} \setminus \{0\}} \frac{\langle \hat{\mathbf{p}}, \dot{\mathbf{p}} \rangle}{\mathcal{F}(\mathbf{p}, \dot{\mathbf{p}})}. \tag{20}$$

The distance map $U = d_{\mathcal{F}}(\mathbf{p}_S, \cdot)$ from a given source point $\mathbf{p}_S \in \mathbb{M}$ is the unique solution, in the sense of viscosity solutions, of the static Hamilton Jacobi equation:

$$U(\mathbf{p}_S) = 0, \text{ and for all } p \in \mathbb{M}$$

$$\mathcal{F}^*(\mathbf{p}, \mathrm{d}U(\mathbf{p})) = 1. \tag{21}$$

Furthermore, if γ is a minimal geodesic from $\mathbf{p}_S$ to some $\mathbf{p} \in \mathbb{M}$, then it obeys the ordinary differential equation (ODE):

$$\begin{cases} \dot{\gamma}(t) = L \ \mathrm{d}_{\hat{\mathbf{p}}} \mathcal{F}^*(\gamma(t), \mathrm{d}U(\gamma(t))), \ L := d_{\mathcal{F}}(\mathbf{p}_S, \mathbf{p}) \\ \gamma(0) = \mathbf{p}_S, \quad \gamma(1) = \mathbf{p}. \end{cases} \tag{22}$$

for any $t \in [0, 1]$ such that the differentiability of U and $\mathcal{F}^*$ holds at the required points. The proof of the ODE (22) is for completeness derived in Proposition 5 of Appendix C, where we also discuss in Remark 14 the common alternative formalism based on the Hamiltonian. We denoted by $\mathrm{d}_{\hat{\mathbf{p}}} \mathcal{F}^*$ the differential of the dual metric $\mathcal{F}^*$ with respect to the second variable $\hat{\mathbf{p}}$, hence $\mathrm{d}_{\hat{\mathbf{p}}} \mathcal{F}^*(\mathbf{p}, \hat{\mathbf{p}}) \in T^{**}_{\mathbf{p}}(\mathbb{M}) \cong T_{\mathbf{p}}(\mathbb{M})$ is indeed a tangent vector to $\mathbb{M}$, for all $(\mathbf{p}, \hat{\mathbf{p}}) \in T^*\mathbb{M}$.

In the rest of this section, we specialize (21) and (22) to the metrics $\mathcal{F}_\varepsilon$ and $\mathcal{F}_\varepsilon^+$. Our first result provides explicit expressions for the dual metrics (required for the eikonal equation).

Proposition 1 *For any $0 < \varepsilon \leq 1$, the duals to the approximate Reeds-Shepp metrics $\mathcal{F}_\varepsilon$ and $\mathcal{F}_\varepsilon^+$ are: for*

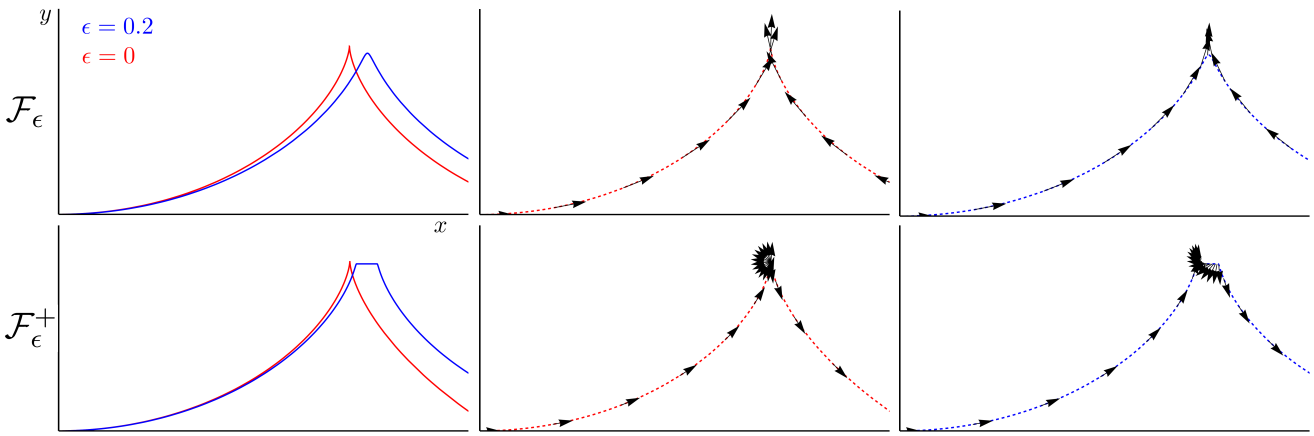

Fig. 7 Non-optimal geodesics in the special case $\mathcal{C} = 1$ and $d = 2$. In particular in the case $\mathcal{F}_0$, keypoints do not appear in the interior of globally optimal curves, only at the end, cf. Theorem 1. We also observe that cusps disappear when $\varepsilon > 0$, cf. Theorem 3. The red curves are spatially very similar, but the part after the cusp/keypoint is traversed with a different orientation. Similar behavior can be observed for the blue curves.

all $(\mathbf{p}, \hat{\mathbf{p}}) \in T^*(\mathbb{M})$, *with* $\mathbf{p} = (\mathbf{x}, \mathbf{n})$ *and* $\hat{\mathbf{p}} = (\hat{\mathbf{x}}, \hat{\mathbf{n}})$

$$\begin{aligned}
\mathcal{F}_\varepsilon^*(\mathbf{p}, \hat{\mathbf{p}})^2 &= (\mathcal{C}_2(\mathbf{p}))^{-2}\|\hat{\mathbf{n}}\|^2 + (\mathcal{C}_1(\mathbf{p}))^{-2}(|\hat{\mathbf{x}} \cdot \mathbf{n}|^2 \\
&\qquad + \varepsilon^2\|\hat{\mathbf{x}} \wedge \mathbf{n}\|^2) \\
\mathcal{F}_\varepsilon^{+*}(\mathbf{p}, \hat{\mathbf{p}})^2 &= (\mathcal{C}_2(\mathbf{p}))^{-2}\|\hat{\mathbf{n}}\|^2 + (\mathcal{C}_1(\mathbf{p}))^{-2}(|\hat{\mathbf{x}} \cdot \mathbf{n}|^2 \\
&\qquad + \varepsilon^2\|\hat{\mathbf{x}} \wedge \mathbf{n}\|^2 - (1 - \varepsilon^2)(\hat{\mathbf{x}} \cdot \mathbf{n})_-^2) \\
&= (\mathcal{C}_2(\mathbf{p}))^{-2}\|\hat{\mathbf{n}}\|^2 + (\mathcal{C}_1(\mathbf{p}))^{-2}((\hat{\mathbf{x}} \cdot \mathbf{n})_+^2 \\
&\qquad + \varepsilon^2(\hat{\mathbf{x}} \cdot \mathbf{n})_-^2 + \varepsilon^2\|\hat{\mathbf{x}} \wedge \mathbf{n}\|^2)
\end{aligned} \tag{23}$$

In order to relate the Finslerian HJB equation (21) and backtracking equation (22) to some more classical Riemannian counterparts, we introduce two Riemannian metric tensor fields on $\mathbb{M}$. The first is defined as the polarisation of the symmetric Finsler norm $\mathcal{F}_\varepsilon(\mathbf{p}, \cdot)$

$$\begin{aligned}
\mathcal{G}_{\mathbf{p};\varepsilon}(\dot{\mathbf{p}}, \dot{\mathbf{p}}) &= |\mathcal{F}_\varepsilon(\mathbf{p}, \dot{\mathbf{p}})|^2 \\
&= \mathcal{C}_1^2(\mathbf{p})((\dot{\mathbf{x}} \cdot \mathbf{n})^2 + \varepsilon^{-2}\|\dot{\mathbf{x}} \wedge \mathbf{n}\|^2) \\
&\qquad + \mathcal{C}_2^2(\mathbf{p})\|\dot{\mathbf{n}}\|^2 \ ,
\end{aligned} \tag{24}$$

where $\dot{\mathbf{p}} = (\dot{\mathbf{x}}, \dot{\mathbf{n}})$, and then one can also rely on gradient fields $\mathcal{G}_{\mathbf{p};\varepsilon}^{-1}\mathrm{d}U$ relative to this metric. This has benefits if it comes to geometric understanding of the eikonal equation and its tracking. Even in the analysis of the non-symmetric case –where one does not have a single metric tensor– this notion plays a role, as we will see in the next main theorem. To this end, in the non-symmetric case, we shall rely on a second spatially isotropic metric tensor given by:

$$\widetilde{\mathcal{G}}_{\mathbf{p};\varepsilon}(\dot{\mathbf{p}}, \dot{\mathbf{p}}) := \mathcal{C}_1^2(\mathbf{p})\varepsilon^{-2}\|\dot{\mathbf{x}}\|^2 + \mathcal{C}_2^2(\mathbf{p})\|\dot{\mathbf{n}}\|^2. \tag{25}$$

We denote by $\nabla_{\mathbb{S}^{d-1}}$ the gradient operator on $\mathbb{S}^{d-1}$ with respect to the inner product induced by the embedding $\mathbb{S}^{d-1} \subset \mathbb{R}^d$, and by $\nabla_{\mathbb{R}^d}$ the canonical gradient operator on $\mathbb{R}^d$.

Corollary 1 *Let $\varepsilon \geq 0$. Then the eikonal PDE (5) for the case $(\mathbb{M}, \mathcal{F}_\varepsilon)$ now takes the form*

$$\begin{gathered}
\sqrt{\frac{\|\nabla_{S^{d-1}} U(\mathbf{p},r)\|^2}{\mathcal{C}_2^2(\mathbf{p})} + \frac{\varepsilon^2\|\nabla_{\mathbb{R}^d} U(\mathbf{p},r)\|^2 + (1-\varepsilon^2)|\,\mathbf{n}\cdot\nabla_{\mathbb{R}^d} U(\mathbf{p},r)\,|^2}{\mathcal{C}_1^2(\mathbf{p})}} = 1, \\
\Leftrightarrow \\
\mathcal{G}_{\mathbf{p};\varepsilon}|_{\mathbf{p}}\left(\mathcal{G}_{\mathbf{p};\varepsilon}^{-1}\mathrm{d}U(\mathbf{p}), \mathcal{G}_{\mathbf{p};\varepsilon}^{-1}\mathrm{d}U(\mathbf{p})\right) = 1
\end{gathered}$$

i.e. the Euclidean norm of the intrinsic gradient equals 1, for $\mathbf{p}$ *where* U *is differentiable.*
The eikonal PDE (5) for the case $(\mathbb{M}, \mathcal{F}_\varepsilon^+)$ now takes the explicit form

$$\begin{gathered}
\sqrt{\frac{\|\nabla_{S^{d-1}} U^+(\mathbf{p},r)\|^2}{\mathcal{C}_2^2(\mathbf{p})} + \frac{\varepsilon^2\|\nabla_{\mathbb{R}^d} U^+(\mathbf{p},r)\|^2 + (1-\varepsilon^2)|\,(\,\mathbf{n}\cdot\nabla_{\mathbb{R}^d} U^+(\mathbf{p},r)\,)_+\,|^2}{\mathcal{C}_1^2(\mathbf{p})}} = 1 \\
\Leftrightarrow \\
\begin{cases}
\mathcal{G}_{\mathbf{p};\varepsilon}|_{\mathbf{p}}\left(\mathcal{G}_{\mathbf{p};\varepsilon}^{-1}\mathrm{d}U^+(\mathbf{p}), \mathcal{G}_{\mathbf{p};\varepsilon}^{-1}\mathrm{d}U^+(\mathbf{p})\right) = 1, \\
\qquad \textit{if } \mathbf{p} \in \mathbb{M}_+ := \{\mathbf{p} \in \mathbb{M} \mid \langle \mathrm{d}U^+(\mathbf{p}), \mathbf{n}\rangle > 0\}, \\
\widetilde{\mathcal{G}}_{\mathbf{p};\varepsilon}|_{\mathbf{p}}\left(\widetilde{\mathcal{G}}_{\mathbf{p};\varepsilon}^{-1}\mathrm{d}U^+(\mathbf{p}), \widetilde{\mathcal{G}}_{\mathbf{p};\varepsilon}^{-1}\mathrm{d}U^+(\mathbf{p})\right) = 1, \\
\qquad \textit{if } \mathbf{p} \in \mathbb{M}_- := \{\mathbf{p} \in \mathbb{M} \mid \langle \mathrm{d}U^+(\mathbf{p}), \mathbf{n}\rangle < 0\}.
\end{cases}
\end{gathered}$$

for those $\mathbf{p} \in \mathbb{M}_+ \cup \mathbb{M}_-$ *where* U^+ *is differentiable*[5].

The proof of Proposition 1 and Corollary 1 can be found in Section 5.

We finally specialize the geodesic ODE (22) to the models of interest. Note that in the case of $\mathcal{F}_\varepsilon^+$,

[5] On $\partial M_\pm$ distance function U^+ is not differentiable

the backtracing switches between qualitatively distinct modes, respectively almost sub-Riemannian and almost purely angular, in the spirit of Theorem 3. Given $\varepsilon > 0$ and $\mathbf{n} \in \mathbb{S}^{d-1}$ let $D^{\varepsilon}_{\mathbf{n}}$ denote the $d \times d$ symmetric positive definite matrix with eigenvalue 1 in the direction $\mathbf{n}$, and eigenvalue ε^2 in the orthogonal directions :

$$D^{\varepsilon}_{\mathbf{n}} := \mathbf{n} \otimes \mathbf{n} + \varepsilon^2 (\mathrm{Id} - \mathbf{n} \otimes \mathbf{n}). \tag{26}$$

Theorem 4 (Back-tracking) *Let $0 < \varepsilon < 1$. Let $\mathbf{p}_{\mathrm{S}} \in \mathbb{M}$ be a source point. Let $U(\mathbf{p}) := d_{\mathcal{F}_\varepsilon}(\mathbf{p}, \mathbf{p}_s)$, $U^+(\mathbf{p}) := d_{\mathcal{F}^+_\varepsilon}(\mathbf{p}, \mathbf{p}_s)$ be distance maps from $\mathbf{p}_s$, w.r.t. Finsler function $\mathcal{F}_\varepsilon$, and $\mathcal{F}^+_\varepsilon$. Let $\gamma, \gamma^+ : [0,1] \to \mathbb{M}$ be normalized geodesics of length L starting at $\mathbf{p}_s$ in $(\mathbb{M}, d_{\mathcal{F}_\varepsilon})$ resp. $(\mathbb{M}, d_{\mathcal{F}^+_\varepsilon})$.*

Given a time $t \in [0,1]$, one has provided that U respectively U^+ are differentiable at $\gamma(t) = (\mathbf{x}(t), \mathbf{n}(t))$ resp. $\gamma^+(t) = (\mathbf{x}^+(t), \mathbf{n}^+(t))$ that

$$\begin{array}{c} \dot{\gamma}(t) = L\, \mathcal{G}^{-1}_{\gamma(t);\varepsilon} \mathrm{d}U(\gamma(t)) \\ \Leftrightarrow \\ \begin{cases} \dot{\mathbf{n}}(t) = L\, \mathcal{C}_2(\gamma(t))^{-1}\, \nabla_{\mathbb{S}^{d-1}} U(\gamma(t)), \\ \dot{\mathbf{x}}(t) = L\, \mathcal{C}_1(\gamma(t))^{-1}\, D^{\varepsilon}_{\mathbf{n}(t)} \nabla_{\mathbb{R}^d} U(\gamma(t)), \end{cases} \end{array} \tag{27}$$

for the Riemannian approximation paths of the Reeds-Shepp care, and

$$\dot{\gamma}^+(t) = L \begin{cases} \mathcal{G}^{-1}_{\gamma^+(t);\varepsilon} \mathrm{d}U^+(\gamma^+(t)) \text{ if } \gamma^+(t) \in \mathbb{M}_+, \\ \widetilde{\mathcal{G}}^{-1}_{\gamma^+(t);\varepsilon} \mathrm{d}U^+(\gamma^+(t)) \text{ if } \gamma^+(t) \in \mathbb{M}_-, \end{cases} \tag{28}$$

with $\widetilde{\mathcal{G}}_{\mathbf{p};\varepsilon}(\dot{\mathbf{p}}, \dot{\mathbf{p}})$ given by (25), with $\dot{\mathbf{p}} = (\dot{\mathbf{x}}, \dot{\mathbf{n}})$, and with disjoint Riemannian manifold splitting $\mathbb{M} = \mathbb{M}_+ \cup \mathbb{M}_- \cup \partial\mathbb{M}_\pm$, where $\mathbb{M}_+$ is equipped with metric tensor $\mathcal{G}_\varepsilon$, $\mathbb{M}_-$ is equipped with metric tensor $\widetilde{\mathcal{G}}_\varepsilon$ and

$$\partial\mathbb{M}_\pm := \overline{\mathbb{M}_+} \setminus \mathbb{M}_+ = \overline{\mathbb{M}_-} \setminus \mathbb{M}_- \tag{29}$$

denotes the transition surface (surface of key-points), for the Riemannian approximation paths of the Reeds-Shepp care without reverse gear.

Remark 6 The general abstract formula (28) reflects that the backtracking in $(\mathbb{M}, \mathcal{F}^+)$ is a combined gradient descent flow on the distance map U^+ on a splitting of $\mathbb{M}$ into two (symmetric) Riemannian manifolds. Its explicit form (likewise (27)) is

$$\begin{cases} \dot{\mathbf{n}}^+(t) = L\, \mathcal{C}_2(\gamma^+(t))^{-1}\, \nabla_{\mathbb{S}^{d-1}} U^+(\gamma^+(t)), \\ \dot{\mathbf{x}}^+(t) = L \begin{cases} \mathcal{C}_1(\gamma^+(t))^{-1}\, D^{\varepsilon}_{\mathbf{n}(t)} \nabla_{\mathbb{R}^d} U^+(\gamma^+(t)) \\ \qquad \text{if } \gamma^+(t) \in \mathbb{M}_+, \\ \varepsilon^2\, \mathcal{C}_1(\gamma^+(t))^{-1}\, \nabla_{\mathbb{R}^d} U^+(\gamma^+(t)) \\ \qquad \text{if } \gamma^+(t) \in \mathbb{M}_-, \end{cases} \end{cases} \tag{30}$$

Note that for the (less useful) isotropic case $\varepsilon = 1$, models $\mathcal{F}_1$ and $\mathcal{F}^+_1$ coincide and geodesics consist of straight lines $\mathbf{x}(\cdot)$ in $\mathbb{R}^d$ and great circles $\mathbf{n}(\cdot)$ in S^d that do not influence each other.

Remark 7 In Theorem 4, we assumed distance maps U and U^+ to be differentiable along the path, which is not always the case. In points where the distance map is not differentiable, one can take any sub-gradient in the sub-differential $\partial U(\mathbf{p})$ in order to identify Maxwell points (and Maxwell strata). In particular, in SR geometry, the set of points where the squared distance function $(d_{\mathcal{F}_0}(\cdot, e))^2$ is smooth is open and dense in any compact subset of $\mathbb{M}$, see [1, Thm. 11.15]. The points where it is non-smooth are rare and meaningful: they are either first Maxwell points, conjugate points or abnormal points. The last type does not appear here, because we have a 2-bracket generating distribution, see e.g. [23, Remark 4] and [1, Ch. 20.5.1.]. At points in the closure of the first Maxwell set, two geodesically equidistant wavefronts collide for the first time, see for example [7, Fig.3, Thm 3.2] for the case $d = 2$ and $\mathcal{C} = \mathcal{C}_1 = \mathcal{C}_2 = 1$. See also Fig. 6, where for some end-conditions 2 optimally back-tracked geodesics end with the same length in such a first Maxwell point. The conjugate points are points where local optimality is lost, for a precise definition see e.g. [1, Def. 8.43].

Remark 8 Recall the convergence result from Theorem 2, and the non-local controllability for the model $(\mathbb{M}, d_{\mathcal{F}^+_0})$. From this we see that the convergence holds pointwise but not uniformly (otherwise the limit distance $d_{\mathcal{F}^+_0}$ was continuous). Nevertheless the minimal paths converge strongly as $\varepsilon \downarrow 0$, and we see that the spatial velocity tends to 0 in (30) if $\varepsilon \downarrow 0$ if $\gamma^*_\varepsilon(t) \in \mathbb{M}_-$. Thereby only in the SR case $\varepsilon = 0$ the gradient flows themselves fit continuously as only there the interface is reached with $\dot{\mathbf{n}} = 0$. See Fig. 7, to see what this means in practice for $\mathbf{n}(t)$ along a SR geodesic in $(\mathbb{M}, \mathcal{F}^+_0)$ with uniform cost. See also the corollary below. See also the corollary below.

Theorem 4 can be extended to the Sub-Riemannian case.

Corollary 2 (SR Backtracking) *Let the cost $\mathcal{C}_1, \mathcal{C}_2$ be smooth, let the source $\mathbf{p}_S \in \mathbb{M}$ and $\mathbf{p} \neq \mathbf{p}_S \in \mathbb{M}$ be such that they can be connected by a unique smooth minimizer γ^*_ε in $(\mathbb{M}, \mathcal{F}_\varepsilon)$ and γ^*_0 in $(\mathbb{M}, \mathcal{F}_0)$, such that $\gamma^*_\varepsilon(t)$ is not a conjugate point for all $t \in [0,1]$ and all sufficiently small $\varepsilon > 0$, say $\varepsilon < \varepsilon_0$, for some $\varepsilon_0 > 0$. Define $U_\varepsilon(\mathbf{p}) := d_{\mathcal{F}_\varepsilon}(\mathbf{p}_s, \mathbf{p})$. Then*

$$\dot{\gamma}^*_0(t) = U_0(\mathbf{p}) \mathcal{G}^{-1}_{\gamma^*_0(t);0}\, \mathrm{d}U_0(\gamma^*_0(t)), \qquad t \in [0,1],$$

with $U_0(\mathbf{p}) = d_{\mathcal{F}_0}(\mathbf{p}_S, \mathbf{p})$ differentiable at $\gamma^*_0(t)$, and U_0 satisfying the eikonal equation:

$$\sqrt{\mathcal{G}_{g;0}\left(\mathcal{G}^{-1}_{g;0} \mathrm{d}U_0(g), \mathcal{G}^{-1}_{g;0} \mathrm{d}U_0(g)\right)} = 1.$$

Proof. From our assumptions on $\mathbf{p}$ and $\gamma_\varepsilon^*(t)$ for $\varepsilon < \varepsilon_0$, we have, recall Remark 7, that $(U_\varepsilon(\cdot))^2$ is differentiable at $\gamma_\varepsilon^*(t)$ for all $0 \leq t \leq 1$ and $0 \leq \varepsilon < \varepsilon_0$. This implies that U_ε is differentiable at $\{\gamma_\varepsilon^*(t) \mid 0 < t \leq 1\}$, for all $\varepsilon < \varepsilon_0$.

From Theorem 2 we have pointwise convergence $U_\varepsilon(\mathbf{p}) \to U_0(\mathbf{p})$ and uniform convergence $\gamma_\varepsilon^* \to \gamma_0^*$ as $\varepsilon \downarrow 0$. Moreover, as γ_ε^* and γ_0^* are solutions of the canonical ODEs of Pontryagin's Maximum Principle, the trajectories are continuously depending on $\varepsilon > 0$, and so are the derivatives $\dot{\gamma}_\varepsilon^*$. As a result, we can apply the backtracking Theorem 4 for $\varepsilon > 0$ and take the required limits:

$$\begin{aligned}\dot{\gamma}_0^*(t) &= \lim_{\varepsilon\downarrow 0} \dot{\gamma}_\varepsilon^*(t) \\ &\overset{\text{Thm. 4}}{=} \lim_{\varepsilon\downarrow 0} U_\varepsilon(\mathbf{p})\, (\mathcal{G}^{-1}_{\gamma_\varepsilon^*(t);\varepsilon} \mathrm{d}U_\varepsilon)(\gamma_\varepsilon^*(t)) \\ &= U_0(\mathbf{p}) \left(\lim_{\varepsilon\downarrow 0} \mathcal{G}^{-1}_{\gamma_\varepsilon^*(t);\varepsilon}\right) \left(\lim_{\varepsilon\downarrow 0} (\mathrm{d}U_\varepsilon(\gamma_\varepsilon^*(t)))\right) \\ &\overset{\text{Thm. 2}}{=} U_0(\mathbf{p})\, \mathcal{G}^{-1}_{\gamma_0^*(t);0} (\mathrm{d}U_0)(\gamma_0^*(t)).\end{aligned} \tag{31}$$

Furthermore,

$$\begin{aligned}1 &= \lim_{\varepsilon\downarrow 0} \sqrt{\mathcal{G}_{g;\varepsilon}\left(\mathcal{G}^{-1}_{g;\varepsilon}\mathrm{d}U_\varepsilon(g), \mathcal{G}_{g;\varepsilon}\mathrm{d}U_\varepsilon(g)\right)} \\ &= \sqrt{\mathcal{G}_{g;0}\left(\mathcal{G}^{-1}_{g;0}\mathrm{d}U_0(g), \mathcal{G}^{-1}_{g;0}\mathrm{d}U_0(g)\right)}\end{aligned}$$

where we recall Corollary 1. Here due to our assumptions, U_ε and U_0 are both differentiable at $\mathbf{p}$. Note that the limit for the inverse metric $\mathcal{G}^{-1}_{\mathbf{p},\varepsilon}$ as $\varepsilon \downarrow 0$ exists, recall Cor. 1. □

Now that we stated our 4 main theoretical results we will prove them in the subsequent sections (and Appendix A).

3 Controllability Properties: Proof of Theorem 1, and Maxwell-points in $(\mathbb{M}, d_{\mathcal{F}_0^+})$

(Global controllability) The two considered Reeds-Shepp models (or metric spaces) $(\mathbb{M}, d_{\mathcal{F}_0})$ and $(\mathbb{M}, d_{\mathcal{F}_0^+})$ are globally controllable, in the sense that the distance maps $d_{\mathcal{F}_0}$ and $d_{\mathcal{F}_0^+}$ take finite values on $\mathbb{M} \times \mathbb{M}$. This easily follows from the observation that any path $\mathbf{x} : [0,1] \to \mathbb{R}^d$, Lipschitz and with non-vanishing speed, can be lifted into a path $\gamma : [0,1] \to \mathbb{M}$ of finite length w.r.t. $\mathcal{F}_0$ and $\mathcal{F}_0^+$, defined by $\gamma(t) := (\mathbf{x}(t), \dot{\mathbf{x}}(t)/\|\dot{\mathbf{x}}(t)\|)$ for all $t \in [0,1]$. The fact that the infimum in (1) is actually a minimum for $\mathcal{F} = \mathcal{F}_0^+$ follows by Corollary 3 in App. A and (8), and the fact that the pseudo-distances take finite values.

(Local controllability) In order to show that the model $(\mathbb{M}, d_{\mathcal{F}_0^+})$ is *not* locally controllable, we need the following lemma.

Lemma 2 *Let $\mathbf{n} : [0,\pi] \to \mathbb{S}^{d-1}$ be strictly 1-Lipschitz. Then $\int_0^\pi \mathbf{n}(0) \cdot \mathbf{n}(t)\,\mathrm{d}t > 0$. Let $\mathbf{n} : \mathbb{R} \to \mathbb{S}^{d-1}$ be strictly 1-Lipschitz and 2π-periodic. Then all points $\mathbf{n}(t)$ lay in a common strict hemisphere. In particular $\mathbf{0} \notin$ Hull$\{\mathbf{n}(t) \mid t \in [0, 2\pi]\}$.*

Proof. The first assumption implies $\mathbf{n}(0) \cdot \mathbf{n}(t) > \cos(t)$ for all $t \in (0,\pi]$ so $\int_0^\pi \mathbf{n}(0) \cdot \mathbf{n}(t)\,\mathrm{d}t > 0$.

Let $\mathbf{n} : \mathbb{R} \to \mathbb{S}^{d-1}$ be strictly 1-Lipschitz and 2π-periodic. Set $\mathbf{M} := \int_0^{2\pi} \mathbf{n}(t)\,\mathrm{d}t$. Then for any $t_0 \in [0, 2\pi]$ one has by the two assumptions

$$\mathbf{n}(t_0)\cdot\mathbf{M} = \int_0^\pi \mathbf{n}(t_0)\cdot\mathbf{n}(t_0+t)\,\mathrm{d}t + \int_0^\pi \mathbf{n}(t_0)\cdot\mathbf{n}(t_0-t)\,\mathrm{d}t > 0,$$

so the image of $\mathbf{n}(\cdot)$ is contained in $\{\mathbf{n} \in \mathbb{S}^{d-1} \mid \mathbf{n} \cdot \mathbf{M} > 0\}$. □

Now the statement that $(\mathbb{M}, d_{\mathcal{F}_0^+})$ is not locally controllable is shown in two steps.
Step 1: we show in the case of a constant cost function $\mathcal{C}_2 = \delta$ one has $\limsup_{\mathbf{p}'\to\mathbf{p}} d_{\mathcal{F}_0^+}(\mathbf{p}, \mathbf{p}') \leq 2\pi\delta$, for any $\mathbf{p} \in \mathbb{M}$. Indeed, one can design an admissible curve in $(\mathbb{M}, \mathcal{F}_0^+)$ as the concatenation of an in-place rotation, a straight line, and an in-place rotation. The length of the straight-line is $\mathcal{O}(\|\mathbf{p}' - \mathbf{p}\|)$ and vanishes when $\mathbf{p}' \to \mathbf{p}$, and the in-place rotations each have maximum cost $\pi\delta$.
Step 2: we prove the lower bound $\lim_{\mu\downarrow 0} d_{\mathcal{F}_0^+}((\mathbf{x},\mathbf{n}), (\mathbf{x} - \mu\mathbf{n}, \mathbf{n})) \geq 2\pi\delta$, for any $(\mathbf{x},\mathbf{n}) \in \mathbb{M}$. This and the above established upper bound implies the required result. As $\mathcal{C}_1, \mathcal{C}_2 \geq \delta$, we can restrict ourselves to the case of uniform cost $\mathcal{C}_1 = \mathcal{C}_2 = \delta = 1$ and just show equality (13), as the estimate (12) follows by scaling with δ.

Consider a Lipschitz regular path $\gamma(t) = (\mathbf{x}(t), \mathbf{n}(t))$, with $\dot{\mathbf{x}} \propto \mathbf{n}$ and $\dot{\mathbf{x}} \cdot \mathbf{n} \geq 0$, from $(\mathbf{x},\mathbf{n})$ to $(\mathbf{x} - \mu\mathbf{n}, \mathbf{n})$. Then

$$\mathbf{0} = \mu\mathbf{n} + \int_0^1 \dot{\mathbf{x}}(t)\mathrm{d}t = \mu\mathbf{n}(0) + \int_0^1 \|\dot{\mathbf{x}}(t)\|\mathbf{n}(t)\mathrm{d}t,$$

so $\mathbf{0} \in$ Hull$\{\mathbf{n}(t);\, 0 \leq t \leq 1\}$. Let $\mathbf{m} : [0,1] \to \mathbb{S}^{d-1}$ be a constant speed parametrization of $\mathbf{n}$. Let $\tilde{\mathbf{m}} : \mathbb{R} \to \mathbb{S}^{d-1}$ be defined by $\tilde{\mathbf{m}}(2\pi t) = \mathbf{m}(t)$ for all $t \in [0, 2\pi]$, and extended by 2π-periodicity. If $\tilde{\mathbf{m}}(\cdot)$ were strictly 1-Lipschitz then by Lemma 2 we would get $\mathbf{0} \notin$ Hull$\{\tilde{\mathbf{m}}(t) \mid t \in [0, 2\pi]\}$ = Hull$\{\mathbf{n}(t) \mid t \in [0,1]\}$ and a contradiction. Hence there exists a $t_0 \in \mathbb{R}$ such that

$\|\dot{\tilde{\mathbf{m}}}(t_0)\| \geq 1$ and via the constant speed parametrization assumption we get the required coercivity:

$$1 \leq \|\dot{\tilde{\mathbf{m}}}(t_0)\| = \frac{1}{2\pi}\int_0^1 \|\dot{\mathbf{n}}(t)\|\,\mathrm{d}t \Rightarrow$$
$$\int_0^1 \mathcal{F}_0^+(\gamma(t),\dot{\gamma}(t))\,\mathrm{d}t \geq \int_0^1 \mathcal{C}_2(\gamma(t))\,\|\dot{\mathbf{n}}(t)\|\,\mathrm{d}t \geq 2\pi\delta.$$

To prove local controllability of the model $(\mathbb{M}, d_{\mathcal{F}_0})$, we apply the logarithmic approximation for weighted sub-coercive operators on Lie groups, cf. [51] applied to the Lie group $SE(d) = \mathbb{R}^d \rtimes SO(d)$, in which the space of positions and orientations is placed via a Lie group quotient $SE(d)/(\{0\} \times SO(d-1))$. One obtains a sharp estimate[6], where the weights of allowable (horizontal) vector fields is 1, whereas the remaining spatial vector fields orthogonal to $\mathbf{n}\cdot\nabla_{\mathbb{R}^d}$ get weight 2, as they follow by a single commutator of allowable vector fields. Relaxing all spatial weights to 2 and continuity of costs $\mathcal{C}_1, \mathcal{C}_2$, yields (14). □

Remark 9 Alternatively, the local controllability of $(\mathbb{M}, d_{\mathcal{F}_0})$ can also be proven using a standard estimate. The commutators of allowable directions in the tangent bundle $T(\mathbb{M})$ (spanned by the specific vector field $\mathbf{n}\cdot\nabla_{\mathbb{R}^d}$ and the velocity vector fields acting only on the angular $\mathbb{S}^{d-1}$-part) span $T(\mathbb{M})$. Then one can apply the 'ball-box theorem' [29,8].

Remark 10 In view of the above one might expect that the point $(\mathbf{x}-\mu\mathbf{n},\mathbf{n})$ is reached by a geodesic that consists of a concatenation of 1. an in-place rotation by π, 2. a straight line, 3. an in-place rotation by π. However, this is not the case as can be observed in the very lower left corner in Fig. 6, where the *two* minimizing red curves show a very different behavior. This is explained by the next lemma.

Lemma 3 *Let $\mu > 0$, and $\mathcal{C}_1 = \mathcal{C}_2 = \delta$. Let $\mathbf{R}_\theta$ denote the (counter-clockwise) rotation matrix about the origin by angle θ. The endpoint $(\mathbf{x}-\mu\mathbf{n},\mathbf{n})$ for each $\mu \geq 0$ is a Maxwell point w.r.t. $(\mathbf{x},\mathbf{n})$, since there are two minimizing geodesics in $(\mathbb{M}, d_{\mathcal{F}_0^+})$ that are a concatenation*

1. *an in-place rotation from $(\mathbf{x},\mathbf{n})$ to $(\mathbf{x},\mathbf{R}_{\pm\frac{\pi}{2}}\mathbf{n})$,*
2. *a full U-curve departing from and ending in a cusp from $(\mathbf{x},\mathbf{R}_{\pm\frac{\pi}{2}}\mathbf{n})$ to $(\mathbf{x}-\mu\mathbf{n},\mathbf{R}_{\mp\frac{\pi}{2}}\mathbf{n})$*
3. *an in-place rotation from $(\mathbf{x}-\mu\mathbf{n},\mathbf{R}_{\mp\frac{\pi}{2}}\mathbf{n})$ to $(\mathbf{x}-\mu\mathbf{n},\mathbf{n})$.*

We have the limit $\lim_{\mu\downarrow 0} d_{\mathcal{F}_0^+}((\mathbf{x},\mathbf{n}),(\mathbf{x}-\mu\mathbf{n},\mathbf{n})) = 2\pi$.

Proof. By rotation and translation covariance, we can restrict ourselves to $\mathbf{x} = \mathbf{0}$, $\mathbf{n} = \mathbf{a}$, and by the coplanarity result in [23, Cor.6, Thm.8], we only need to consider $d = 2$ and $\mathbf{a} = (1,0)^T$.

From Theorem 3 (that we prove later) we know that keypoints only occur at the endpoints of minimal paths. Since cuspless geodesics stay in the positive half-space set by their initial orientation, recall Remark 3, the optimal path from $(\mathbf{0},\mathbf{a})$ to $(-\mu\mathbf{a},\mathbf{a})$ starts with a rotation by at least a $\frac{\pi}{2}$ angle. For the same reason, it ends with a rotation by at least a $\frac{\pi}{2}$ angle. There exists a U-curve, starting and ending in a cusp, optimally connecting $(\mathbf{0},\mathbf{R}_{\frac{\pi}{2}}\mathbf{a})$ with $(-\mu\mathbf{a},\mathbf{R}_{-\frac{\pi}{2}}\mathbf{a})$ [21]. Hence the concatenation of curves as described points 1.-3. is optimal, and has the same length as the alternative (with rotations in the opposite direction).

For the total distance by such a curve we use [7] [21, Cor.2]:

$$d_{\mathcal{F}_0^+}((\mathbf{x},\mathbf{n}),(\mathbf{x}-\mu\mathbf{n},\mathbf{n})) =$$
$$\frac{\pi}{2} + \int_0^{s_{max}(1,\mu)} \frac{1}{\sqrt{1-|\mu\sinh s+\cosh s|^2}}\,\mathrm{d}s + \frac{\pi}{2},$$

with $s_{max}(1,\mu)$ the first positive root of the denominator of the integrand. Letting $\mu \downarrow 0$ we get $\lim_{\mu\downarrow 0} d_{\mathcal{F}_0^+}((\mathbf{x},\mathbf{n}),(\mathbf{x}-\mu\mathbf{n},\mathbf{n})) = 2\pi$.

□

Remark 11 Consider the case $d = 2$, $\mathcal{C}_1 = \mathcal{C}_2 = \delta$, and source point $\mathbf{p}_S = (\mathbf{x},\mathbf{n}) = \mathbf{e} = (0,0,\theta = 0)$. The end-points $(\mathbf{x}-\mu\mathbf{n},\mathbf{n}) = (-\mu,0,0)$, with $\mu > 0$ sufficiently small, are 1st Maxwell-points in $(\mathbb{M}, d_{\mathcal{F}_0^+})$ where geodesically equidistant wavefronts departing from the source point collide for the first time. See Fig. 8. The distance mapping $d^+_{\mathcal{F}_0}(\mathbf{p}_S,\cdot)$ is not continuous, but the asymmetric distance spheres $\mathcal{S}_R := \{\mathbf{p}\in\mathbb{M} \mid d^+_{\mathcal{F}_0}(\mathbf{p}_S,\mathbf{p}) = R\}$ are connected and compact, and they collide at $R = 2\pi$ in such a way that the origin $\mathbf{p}_s$ becomes an interior point in the asymmetric balls of radius $R > 2\pi$.

4 Cusps and Keypoints: Proof of Theorem 3

In this section we provide a proof of Theorem 3 on the occurrence of cusps and keypoints. For the uniform cost case $\mathcal{C}_1 = \mathcal{C}_2 = 1$ for $d = 2$, our curve-optimization problem (1) $(\mathbb{M}, d_{\mathcal{F}_0})$ in consideration, boils down to a standard left-invariant curve optimization in the roto-translation group $SE(2) = \mathbb{R}^2 \rtimes SO(2)$. As we will apply tools from previous works [21,10,9,46], we will make

[6] For specific sharp estimates for $d = 3$, in the context of heat-kernels estimation, see [43, ch.5.1].

[7] In [21, Cor.2] one must set $z(0) = z(L) = 1$ and $\dot{z}(0) = \chi \downarrow 0$

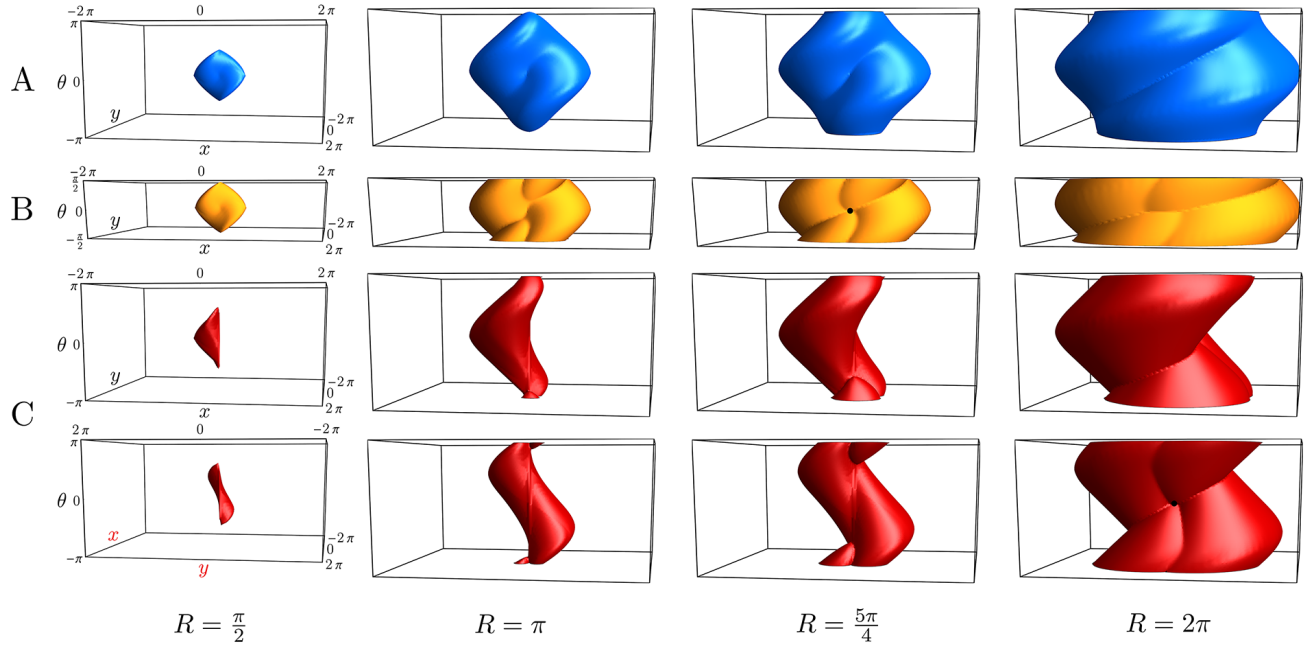

Fig. 8 The development of spheres centered around $\mathbf{e} = (0,0,0)$ with increasing radius R. **A:** the normal SR spheres on $\mathbb{M}$ given by $\{\mathbf{p} \in \mathbb{M} \mid d_{\mathcal{F}_0}(\mathbf{p},\mathbf{e}) = R\}$ where the folds reflect the 1st Maxwell sets [7,46]. **B:** the SR spheres with identification of antipodal points given by $\{\mathbf{p} \in \mathbb{M} \mid \min\{\, d_{\mathcal{F}_0}(\mathbf{p},\mathbf{e}), d_{\mathcal{F}_0}(\mathbf{p}+(0,0,\pi),\mathbf{e})\,\} = R\}$ with additional folds (1st Maxwell sets) due to π-symmetry. **C:** the asymmetric Finsler norm pseudo spheres given by $\{\mathbf{p} \in \mathbb{M} \mid d_{\mathcal{F}_0^+}(\mathbf{p},\mathbf{e}) = R\}$ visualized from two perspectives with extra folds (1st Maxwell sets) at the back $(-\mu,0,0)$. The black dots indicate points with two folds. In the case of B, this is a Maxwell-point with 4 geodesics merging. In the case of C, this is just the origin itself reached from behind at $R = 2\pi$, recall Lemma 3. Although not depicted here, if the radius $R > 2\pi$ the origin becomes an interior point of the corresponding pseudo ball.

use of the following notations for expansion[8] of velocity and momentum in the left-invariant (co)-frame:

$$\begin{cases} \mathcal{A}_1 := \cos\theta\,\partial_x + \sin\theta\,\partial_y, \\ \mathcal{A}_2 := -\sin\theta\,\partial_x + \cos\theta\,\partial_y, \\ \mathcal{A}_3 := \partial_\theta, \end{cases}$$

$$\begin{cases} \omega^1 := \cos\theta\,\mathrm{d}x + \sin\theta\,\mathrm{d}y, \\ \omega^2 := -\sin\theta\,\mathrm{d}x + \cos\theta\,\mathrm{d}y, \\ \omega^3 := \mathrm{d}\theta, \end{cases}$$

$$\dot\gamma(t) = \sum_{i=1}^{3} u^i(t)\ \mathcal{A}_i|_{\gamma(t)} \in T_{\gamma(t)}(\mathbb{M}),$$

$$\hat{\mathbf{p}}(t) = \sum_{i=1}^{3} \hat p_i(t)\ \omega^i\big|_{\gamma(t)} \in T^*_{\gamma(t)}(\mathbb{M}),$$

where the indexing of the left-invariant frame is different here, in order to stick to the ordering (x,y,θ) applied in this article. Note that for the case $\varepsilon = 0$ admissible smooth curves γ in $(\mathbb{M}, d_{\mathcal{F}_0})$ satisfy the horizontality constraint $\dot\gamma(t) \in \mathrm{Span}\{\,\mathcal{A}_1|_{\gamma(t)}\,,\,\mathcal{A}_3|_{\gamma(t)}\}$.

Proof of the statements regarding cusps:

– We can describe our curve optimization problem (1) using a Hamiltonian formalism, with Hamiltonian $H(\hat{\mathbf{p}}) = \frac{1}{2}\left(\hat p_1^2 + \hat p_3^2\right) = \frac{1}{2}$ [39]. By Pontryagin's Maximum Principle, geodesics adhere to the following Hamilton equations:

$$\begin{cases} \dot p_1 = u^1 = \hat p_1, \\ \dot p_2 = u^2 = 0, \\ \dot p_3 = u^3 = \hat p_3, \end{cases} \quad , \quad \begin{cases} \frac{d\hat p_1}{dt} = \hat p_2 \hat p_3, \\ \frac{d\hat p_2}{dt} = -\hat p_1 \hat p_3, \\ \frac{d\hat p_3}{dt} = -\hat p_1 \hat p_2. \end{cases} \tag{32}$$

For fixed initial momentum $\hat{\mathbf{p}}(0)$, these equations uniquely determine a geodesic. Moreover, cuspless SR geodesics are contained within the (co-adjoint) orbits

$$(\hat p_1(t))^2 + (\hat p_2(t))^2 = (\hat p_1(0))^2 + (\hat p_2(0))^2. \tag{33}$$

The parameter t in the system (32) is SR arc length, but by reparametrizing (possible as long as u^1 does not change sign) to spatial arc length parameter s, with $\frac{ds}{dt} = \hat p_1$, we get a partially linear system. Combining (32) and (33), we find orbits in the (hyper-

[8] Note that we use upper-indices for the control's (velocity components) as they are contra-variant.

bolic) phase portrait induced by

$$\begin{cases} \frac{d}{ds}\hat{p}_2 = -\hat{p}_3 \\ \frac{d}{ds}\hat{p}_3 = -\hat{p}_2 \end{cases} \Longrightarrow$$
$$\begin{cases} \hat{p}_2(s) = \hat{p}_2(0)\cosh s - \hat{p}_3(0)\sinh s \\ \hat{p}_3(s) = -\hat{p}_2(0)\sinh s + \hat{p}_3(0)\cosh s \end{cases}$$

Hence $|\hat{p}_3(s)| = 1$ always has a solution for some finite (possibly negative) s, except when $\hat{p}^2(0) = \hat{p}_3(0) = 0$, in which case the solutions are straight lines. Preservation of the Hamiltonian then implies that $\hat{p}_1 = u^1 = 0$. We conclude that every SR geodesic (with unconstrained time $t \in \mathbb{R}$) in $(\mathbb{M}, d_{\mathcal{F}_0})$ which is not a straight line admits a cusp.

– We now consider $(\mathbb{M}, d_{\mathcal{F}_\varepsilon})$, $\varepsilon > 0$. To have a cusp, we need $\hat{p}_1(t) = \hat{p}_2(t) = 0$ for some $t \in \mathbb{R}$. The co-adjoint orbit condition (33) then implies that $\hat{p}_1(t) = \hat{p}_2(t) = 0$ for all t, corresponding to a vertical geodesic that has purely angular momentum and no cusp. The same argument holds for $(\mathbb{M}, d_{\mathcal{F}_\varepsilon^+})$. In $(\mathbb{M}, d_{\mathcal{F}_0^+})$ we have the condition that $u^1 \geq 0$, hence by definition it can never switch sign and all geodesics are cuspless.

Proof of the statements regarding keypoints:

– For the cases $(\mathbb{M}, d_{\mathcal{F}_\varepsilon})$ and $(\mathbb{M}, d_{\mathcal{F}_\varepsilon^+})$ with $\varepsilon > 0$ we can use the same line of arguments as above. Also here both spatial controls have to vanish, resulting in vertical geodesics. The spatial projection of such curves is a single keypoint. For $(\mathbb{M}, d_{\mathcal{F}_0})$ we rely on the result that SR geodesics are analytical, and therefore if the control $u^1(t) = 0$ for some open time interval (t_0, t_1), then $u^1(t) = 0$ for all $t \in \mathbb{R}$, again corresponding to purely angular motion.

– Geodesics in $(\mathbb{M}, d_{\mathcal{F}_0^+})$ can have key points only at the boundaries. Suppose a geodesic $\gamma : [0,1] \to \mathbb{M}$ in $(\mathbb{M}, d_{\mathcal{F}_0^+})$ has an internal key point, with a corner of angle $\delta > 0$, at internal time $T_1 \in (0,1)$. Then one can create a local short-cut with a straight-line segment connecting two sufficiently close points before and after the corner with two in-place rotations whose angles add up to δ. With a suitable mollifier this short-cut can be approximated by a curve in Γ. For details see similar arguments in [10].

Next we explain the cases A), B) and C), where we fix initial point $\gamma(0) = \mathbf{e} = (0,0,0)$.

A) Suppose that the endpoint $\mathbf{p} = (x, y, \theta) \in \overline{\mathfrak{R}}$ and $x \geq 0$. Then $\mathbf{p}$ can already be reached by a geodesic in $(\mathbb{M}, d_{\mathcal{F}_0})$ and the positivity constraint (absense reverse gear), which can only increase length, becomes obsolete.

B) Now suppose the end-point $\mathbf{p} = (x, y, \theta)$ lays in the half-space $x < 0$. Then by the half-space property of geodesics in $(\mathbb{M}, d_{\mathcal{F}_0})$, cf.[21, Thm.7], the geodesic in $(\mathbb{M}, d_{\mathcal{F}_0^+})$ must have a key-point. By the preceeding keypoints (where in-place rotations take place) can only be located at the boundaries. If it takes place at the end point only then still the constraint $x < 0$ is not satisfied, thereby it must take place at the origin.

C) In those cases the endpoint $\mathbf{p}$ lays outside the connected cone of reachable angles, which are by [21, Thm.9] bounded (for those end-points) by geodesics ending in a cusp (so not end-points of geodesics starting at a cusp). So for those points optimal geodesics will first move by an in-place rotation (along a spherical geodesic) until it hits the cusp surface $\partial\mathfrak{R}$, after which it is traced back to the origin by a regular geodesic with strictly positive spatial control inside the volume $\mathfrak{R}$.

5 Eikonal equations and backtracking: Proof of Prop. 1, Corr. 1 and Thm. 4

First we shall prove Proposition 1, regarding the duals $\mathcal{F}_\varepsilon$ and $\mathcal{F}_\varepsilon^+$, and Corollary 1, providing explicit expressions for the corresponding eikonal equations. To this end we need a basic Lemma on computing dual norms on $\mathbb{R}^n$, where later we will set $n = 2d-1 = \dim(\mathbb{M})$, and $\mathbf{v}$ equal to the moving frame components of $\dot{\mathbf{p}} \in T_{\mathbf{p}}(\mathbb{M})$ and $\hat{\mathbf{v}} \in (\mathbb{R}^n)^* \equiv \mathbb{R}^n$ equal to the moving frame components of $\hat{\mathbf{p}} \in T^*_{\mathbf{p}}(\mathbb{M})$.

Lemma 4 *Let $\mathbf{w} \in \mathbb{R}^n$ and let $M \in \mathbb{R}^{n\times n}$ be symmetric, positive definite. Define the norm $F_{M,\mathbf{w}} : \mathbb{R}^n \to \mathbb{R}^+$ by*

$$F_{M,\mathbf{w}}(\mathbf{v}) = \sqrt{(M\mathbf{v},\mathbf{v}) + (\mathbf{w},\mathbf{v})_-^2}.$$

Then the corresponding dual norm $F^*_{M,\mathbf{w}} : (\mathbb{R}^n)^* \to \mathbb{R}^+$ equals

$$F^*_{M,\mathbf{w}}(\hat{\mathbf{v}}) = \sqrt{(\hat{\mathbf{v}}, \hat{M}\hat{\mathbf{v}}) + (\hat{\mathbf{v}},\hat{\mathbf{w}})_+^2}, \tag{34}$$

with $\hat{M} = (M + \mathbf{w}\otimes\mathbf{w})^{-1}$ and $\hat{\mathbf{w}} = \frac{M^{-1}\mathbf{w}}{\sqrt{1+(\mathbf{w},M^{-1}\mathbf{w})}}$.

Proof. For $n = 1$ the result is readily verified, and for $\mathbf{w} = \mathbf{0}$ the result is classical. We next turn to the special case $M = \mathrm{Id}$, and $\mathbf{w} = (w_1, \mathbf{0}_{\mathbb{R}^{n-1}})$ is zero except maybe for its first coordinate w_1. Thus for any $\mathbf{v} = (v_1, \mathbf{v}_2) \in \mathbb{R}^n = \mathbb{R}\times\mathbb{R}^{n-1}$ one has the splitting

$$\begin{aligned} F_{M,\mathbf{w}}(v_1,\mathbf{v}_2)^2 &= \left(|v_1|^2 + (w_1 v_1)_-^2\right) + \|\mathbf{v}_2\|^2 \\ &:= F_1(v_1)^2 + F_2(\mathbf{v}_2)^2. \end{aligned} \tag{35}$$

Using the compatibility of norm duality with such splittings, and the special cases $n = 1$ and $\mathbf{w} = 0$ mentioned above, we obtain

$$F^*_{M,\mathbf{w}}(\hat{v}_1, \hat{\mathbf{v}}_2)^2 = F^*_1(\hat{v}_1)^2 + F^*_2(\hat{\mathbf{v}}_2)^2 = \frac{|\hat{v}_1|^2 + (w_1\hat{v}_1)^2_+}{1 + |w_1|^2} + \|\hat{\mathbf{v}}_2\|^2,$$

which is exactly of the form (34). The general case for arbitrary $\mathbf{w}$ and symmetric positive definite M follows from affine invariance. Indeed let A be an invertible $n \times n$ matrix, and let $M' = A^{\mathrm{T}} M A$ and $\mathbf{w}' = A^{\mathrm{T}}\mathbf{w}$. Let $F = F_{M,\mathbf{w}}$ and $F' = F_{M',\mathbf{w}'}$, so that $F'(\mathbf{v}) = F(A\mathbf{v})$ for all $\mathbf{v} \in \mathbb{R}^n$. Let F^*, $\hat{M}$, $\hat{\mathbf{w}}$, and F'^*, $\hat{M}'$, $\hat{\mathbf{w}}'$, be respectively the dual norms and the matrices defined by the explicit formulas above. Then denoting $B := (A^{\mathrm{T}})^{-1}$ one has by the definition of dual norms that $F'^*(\hat{\mathbf{v}}) = F^*(B\hat{\mathbf{v}})$ for all $\hat{\mathbf{v}} \in \mathbb{R}^n$, and by the explicit formulas $\hat{M}' = B^{\mathrm{T}}\hat{M}B$, $\mathbf{w}' = B^{\mathrm{T}}\mathbf{w}$. Thus, $F^* = F^*_{M,\mathbf{w}}$ holds if and only if $F'^* = F^*_{M',\mathbf{w}'}$. Since for any $M, \mathbf{w}$, there exists a linear change of variables A such that $M' = \mathrm{Id}$ and $\mathbf{w}'$ is zero except maybe for its first coordinate, the proof is complete. □

Now Proposition 1 follows from Lemma 4 by writing out the dual norm, using for each $\mathbf{p} \in \mathbb{M}$:

$$M_{\mathbf{p}} = (\mathcal{C}_1(\mathbf{p}))^2 (D^{\varepsilon}_{\mathbf{n}})^{-1} \oplus (\mathcal{C}_2(\mathbf{p}))^2 I_d \quad \text{and} \quad \mathbf{w}_{\mathbf{p}} = \begin{cases} \mathcal{C}_1(\mathbf{p})\sqrt{\varepsilon^{-2} - 1}\,(\mathbf{n}, \mathbf{0}), & \text{for } \mathcal{F}^+_{\varepsilon}, \\ \mathbf{0}, & \text{for } \mathcal{F}_{\varepsilon}, \end{cases} \tag{36}$$

with $D^{\varepsilon}_{\mathbf{n}}$ as in (26). Corollary 1 then follows by setting the momentum covector $\hat{\mathbf{p}} = \mathrm{d}U(\mathbf{p})$ equal to the derivative of the value function evaluated at $\mathbf{p}$.

Now that we have derived the eikonal equations, we obtain the backtracking Theorem 4 by Proposition 5 in App. C, which shows us that level sets of solutions of the eikonal equations are geodesically equidistant surfaces and that geodesics are found by an instrinsic gradient descent.

However, to obtain the explicit backtracking formulas we differentiate the Hamiltonian, rather than the dual metric, which is equivalent thanks to (59) (Remark 14 in App. C) and is simpler due to the lack of square root. We focus below on the model $\mathcal{F}^+_{\varepsilon}$ without reverse gear, since the other case is similar and simpler. Let $\mathbf{p} \in \mathbb{M}$, let $F := \mathcal{F}^+_{\varepsilon}(\mathbf{p}, \cdot)$, and let $\hat{\mathbf{p}} = (\hat{\mathbf{x}}, \hat{\mathbf{n}}) \in T^*_{\mathbf{p}}(\mathbb{M})$. Then differentiating w.r.t. $\hat{\mathbf{n}}$ we obtain

$$\mathrm{d}_{\hat{\mathbf{n}}} F^*(\hat{\mathbf{x}}, \hat{\mathbf{n}})^2 = \mathcal{C}_2(\mathbf{p})^{-2}\,\mathrm{d}_{\hat{\mathbf{n}}}\|\hat{\mathbf{n}}\|^2 = 2\,\mathcal{C}_2(\mathbf{p})^{-2}\hat{\mathbf{n}},$$

where $\|\cdot\|$ is the Riemannian metric induced by the embedding $\mathbb{S}^{d-1} \subset \mathbb{R}^d$. Differentiating w.r.t. $\hat{\mathbf{x}}$ we obtain on the other hand

$$\mathrm{d}_{\hat{\mathbf{x}}} F^*(\hat{\mathbf{x}}, \hat{\mathbf{n}})^2 = \mathcal{C}_1(\mathbf{p})^{-2}\,\mathrm{d}_{\hat{\mathbf{x}}}(\hat{\mathbf{x}} \cdot D^{\varepsilon}_{\mathbf{n}}\hat{\mathbf{x}} - (1 - \varepsilon^2)(\hat{\mathbf{x}} \cdot \mathbf{n})^2_-) \tag{37}$$

$$= 2\,\mathcal{C}_1(\mathbf{p})^{-2} \begin{cases} D^{\varepsilon}_{\mathbf{n}}\hat{\mathbf{x}} & \text{if } \hat{\mathbf{x}} \cdot \mathbf{n} \geq 0, \\ \varepsilon^2\,\mathrm{Id}\,\hat{\mathbf{x}} & \text{if } \hat{\mathbf{x}} \cdot \mathbf{n} \leq 0. \end{cases} \tag{38}$$

The announced result (30), which is equivalent to its more concise abstract form (27), follows by choosing $\hat{\mathbf{x}} := \nabla_{\mathbb{R}^d} U(\gamma(t))$ and $\hat{\mathbf{n}} := \nabla_{\mathbb{S}^{d-1}} U(\gamma(t))$ and a basic re-scaling $[0, L] \ni t \mapsto t/L \in [0, 1]$.

Remark 12 The computation of the dual norms can be simplified by expressing velocity (entering the Finsler metric) and momentum (entering the dual metric) in a (left-invariant) local, orthogonal, moving frame of reference, attached to the point $\mathbf{p} = (\mathbf{x}, \mathbf{n}) \in \mathbb{M}$:

$$\dot{\mathbf{p}} = \sum_{i=1}^{2d-1} u^i\, \mathcal{A}_i\big|_{\mathbf{p}}\,, \quad \hat{\mathbf{p}} = \sum_{i=1}^{2d-1} \hat{p}_i\; \omega^i\big|_{\mathbf{p}} \tag{39}$$

where a[9] moving frame of reference is chosen such that

$$\begin{cases} u^d = \mathbf{n} \cdot \dot{\mathbf{x}}, \\ \sum\limits_{i=1}^{d-1} (u^i)^2 = \|\dot{\mathbf{x}}\|^2 - (\mathbf{n} \cdot \dot{\mathbf{x}})^2, \\ \sum\limits_{i=1}^{d-1} (u^{d+i})^2 = \|\dot{\mathbf{n}}\|^2, \end{cases}$$

inducing a corresponding dual frame $\{\omega^i\big|_{\mathbf{p}}\}$ via

$$\langle \omega^i\big|_{\mathbf{p}}\,, \mathcal{A}_j\big|_{\mathbf{p}} \rangle = \delta^i_j, \text{ for all } i, j = 1, \ldots, 2d-1. \tag{40}$$

W.r.t. the left-invariant frame the matrices $D^{\varepsilon}_{\mathbf{n}}$, $M_{\mathbf{p}}$ as in (36) and $\hat{M}_{\mathbf{p}}$ all become diagonal matrices, and the dual can be computed straightforwardly. Furthermore, in this formulation we can see from the expression for the dual $(\mathcal{F}^+_0)^*$, i.e. in the limit $\varepsilon \downarrow 0$, that the positive spatial control u^d constraint results in a positive momentum $\hat{p}_d$ constraint:

$$\big((\mathcal{F}^+_0)^*(\mathbf{p}, \hat{\mathbf{p}})\big)^2 = \mathcal{C}_1^{-2}(\mathbf{p})(\hat{p}_d)^2_+ + \mathcal{C}_2^{-2}(\mathbf{p}) \sum_{i=d+1}^{2d-1} (\hat{p}_i)^2. \tag{41}$$

[9] For $d > 2$ there exist infinitely many of such frames [23]. In fact, each left-invariant frame in $SE(3)$ acting transitively on $\mathbb{M}$, depending on an extra angle α, gives rise to such a frame in $\mathbb{R}^3 \rtimes S^2 = SE(3)/(\{\mathbf{0}\} \times SO(2))$.

6 Discretization of the Eikonal PDEs

6.1 Causal operators and the fast marching algorithm

The fast marching algorithm is an efficient numerical method [53] for numerically solving the static first order Hamilton-Jacobi-Bellman (or simply eikonal) PDE (5) which characterizes the distance map U to a fixed source point $\mathbf{p}_{\mathrm{S}}$. Fast marching is tightly connected with Dijkstra's algorithm on graphs, an in particular it shares the $\mathcal{O}(KN \ln N)$ complexity, where $N = \#(X)$ is the cardinality of the discrete domain $X \subset \mathbb{M}$, $X \ni \mathbf{p}_{\mathrm{S}}$, and K is the average number of neighbors for each point. Both fast marching and Dijkstra's algorithms can be regarded as specialized solvers of non-linear fixed point systems of equations $\Lambda u = u$, where the unknown $u \in \mathbb{R}^X$ is a discrete map representing the front arrival times, which rely on the a-priori assumption that the operator $\Lambda : \mathbb{R}^X \to \mathbb{R}^X$ is *causal* (and monotone, but this second assumption is not discussed here). Causality informally means that the estimated front arrival time $\Lambda u(\mathbf{p})$ at a point $\mathbf{p} \in X$ depends on the given arrival times $u(\mathbf{q})$, $\mathbf{q} \in X$, prior to $\Lambda u(\mathbf{p})$, but not on the simultaneous or the future ones. Formally, one requires that for any $u, v \in \mathbb{R}^X$, $t \in \mathbb{R}$:

$$\begin{aligned} &\text{If } u^{<t} = v^{<t} \text{ then } (\Lambda u)^{\leq t} = (\Lambda v)^{\leq t}, \\ &\quad \text{where } u^{<t}(\mathbf{p}) := \begin{cases} u(\mathbf{p}) & \text{if } u(\mathbf{p}) < t, \\ +\infty & \text{otherwise,} \end{cases} \end{aligned} \tag{42}$$

and where $v^{<t}$, $(\Lambda u)^{\leq t}$ and $(\Lambda v)^{\leq t}$ are defined in a similar fashion.

A semi-Lagrangian scheme. We implemented two discretizations of the eikonal equation (5) which benefit from the causality property. The first one is a semi-lagrangian scheme, inspired by *Bellman's optimality principle* which informally states that any sub-policy of an optimal policy is an optimal policy. Formally, let $\mathcal{F}$ be a Finsler metric, and let $U := d_{\mathcal{F}}(\cdot, \mathbf{p}_{\mathrm{S}})$ be defined as the distance to a given source point $\mathbf{p}_{\mathrm{S}}$. Then for any $\mathbf{p} \in \mathbb{M}$ and any neighborhood V of $\mathbf{p}$ not containing $\mathbf{p}_{\mathrm{S}}$ one has the property

$$U(\mathbf{p}) := \min_{\mathbf{q} \in \partial V} d_{\mathcal{F}}(\mathbf{p}, \mathbf{q}) + U(\mathbf{q}). \tag{43}$$

In the spirit of [53,50] we discretize (43) by introducing for each interior $\mathbf{p} \in X \setminus \{\mathbf{p}_{\mathrm{S}}\}$ a small polygonal neighborhood $V(\mathbf{p})$, which vertices belong to the discrete point set X. The nonlinear operator Λ is defined as

$$\begin{aligned} \Lambda u(\mathbf{p}) := \min_{\substack{\{\mathbf{q}_1, \cdots, \mathbf{q}_n\} \\ \text{facet of } \partial V(\mathbf{p})}} \min_{\xi \in \Xi} \mathcal{F}\left(\mathbf{p}, \sum_{i=1}^n \xi_i \mathbf{q}_i - \mathbf{p}\right) \\ + \sum_{i=1}^n \xi_i u(\mathbf{q}_i), \end{aligned} \tag{44}$$

where $\Xi = \{\xi \in \mathbb{R}^n_+; \sum_{i=1}^n \xi_i = 1\}$. In other words, the boundary point $\mathbf{q} \in \partial V(\mathbf{p})$ in (43) is represented in (44) as the barycentric sum $\mathbf{q} = \sum_{i=1}^n \xi_i \mathbf{q}_i$, the distance $d_{\mathcal{F}}(\mathbf{p}, \mathbf{q})$ is approximated with the norm $\mathcal{F}(\mathbf{p}, \mathbf{q} - \mathbf{p})$, and the value $U(\mathbf{q})$ is approximated with the interpolation $\sum_{i=1}^n \xi_i u(\mathbf{q}_i)$.

We refer to [50,55] for proofs of convergence, and of the following essential property: the operator (44) obeys the causality property (42) iff the chosen stencil $V(\mathbf{p})$ obeys the following generalized acuteness property: for any $\mathbf{q}, \mathbf{q}'$ in a common facet of $V(\mathbf{p})$, one has

$$\langle d_{\hat{\mathbf{p}}} \mathcal{F}(\mathbf{p}, \mathbf{q} - \mathbf{p}), \mathbf{q}' - \mathbf{p} \rangle \geq 0.$$

For the construction of such stencils $V(\mathbf{p})$, $\mathbf{p} \in X$, we rely on the previous works [37,38] and on the following observation: the metrics $\mathcal{F}_\varepsilon$ and $\mathcal{F}_\varepsilon^+$ associated to the Reeds-Shepp car models can be decomposed as

$$\mathcal{F}(\mathbf{p}, (\dot{\mathbf{x}}, \dot{\mathbf{n}}))^2 = \mathcal{F}_1(\mathbf{p}, \dot{\mathbf{x}})^2 + \mathcal{F}_2(\mathbf{p}, \dot{\mathbf{n}})^2, \tag{45}$$

which allows to build the stencils $V(\mathbf{p})$ for $\mathcal{F}$ by combining, as discussed in [37, p. 9], some lower dimensional stencils $V_1(\mathbf{p})$ and $V_2(\mathbf{p})$ built independently for for the spatial $\mathbf{x} \in \mathbb{R}^d$ and spherical $\mathbf{n} \in \mathbb{S}^{d-1}$ variables.

We discretize $\mathbb{S}^1$ uniformly, with the standard choice of stencil. We discretize $\mathbb{S}^2$ by refining uniformly the faces of an icosahedron and projecting their vertices onto the sphere (as performed by the Mathematica® Geodesate function). The resulting triangulation only features acute interior angles, in the classical Euclidean sense, and thus provides adequate stencils since in our applications $\mathcal{F}_2(\mathbf{p}, \dot{\mathbf{n}}) = \mathcal{C}_2(\mathbf{p}) \|\dot{\mathbf{n}}\|^2$ is proportional to the Euclidean norm, see Fig. 9. We typically use 60 discretization points for $\mathbb{S}^1$, and from 200 to 2000 points for $\mathbb{S}^2$.

We discretize $\mathbb{R}^d$ using the cartesian grid $h\mathbb{Z}^d$, where $h > 0$ is the discretization scale. The norm $\mathcal{F}_{\varepsilon,1}(\mathbf{p}, \dot{\mathbf{x}})$ induced by the approximate Reeds-Shepp model $\mathcal{F}_\varepsilon$ on the physical variables $\mathbb{R}^d$, is of Riemannian type, strongly anisotropic and in dimension $d \leq 3$, which is the adequate setting for the adaptive stencils of [37], built using discrete geometry tools known as lattice basis reduction. The norm induced by $\mathcal{F}_\varepsilon^+$ on $\mathbb{R}^d$ is Finslerian (i.e. non-Riemannian) and strongly anisotropic. In dimension $d = 2$, this is the adequate setting for the adaptive stencils of [38], built using an arithmetic object known as the Stern-Brocot tree.

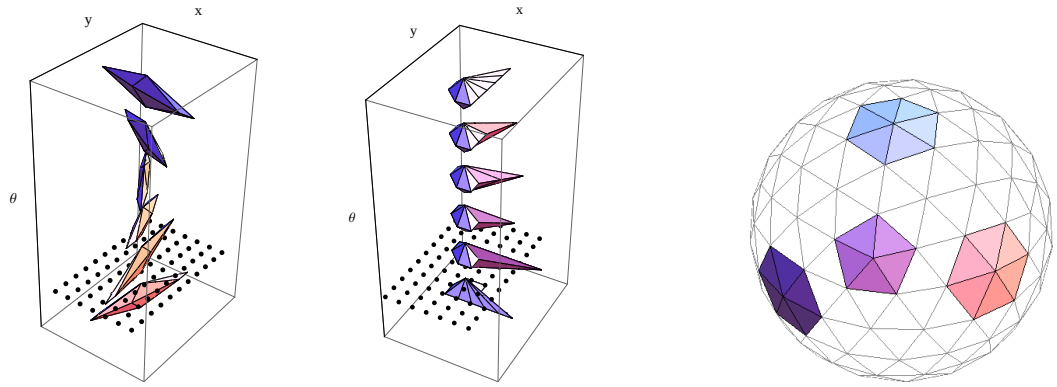

Fig. 9 Left: Stencil used for the metric $\mathcal{F}_\varepsilon$ on $\mathbb{R}^2 \times \mathbb{S}^1$, $\varepsilon = 0.1$, obeying the generalized acuteness property required for the Bellman type discretization (44). See also the control sets in Fig. 1. Center: likewise with $\mathcal{F}_\varepsilon^+$, $\varepsilon = 0.1$. Right: Coarse discretization of $\mathbb{S}^2$ with 162 vertices, used in some experiments posed on $\mathbb{R}^3 \times \mathbb{S}^2$. Some acute stencils (in the classical euclidean sense) shown in color.

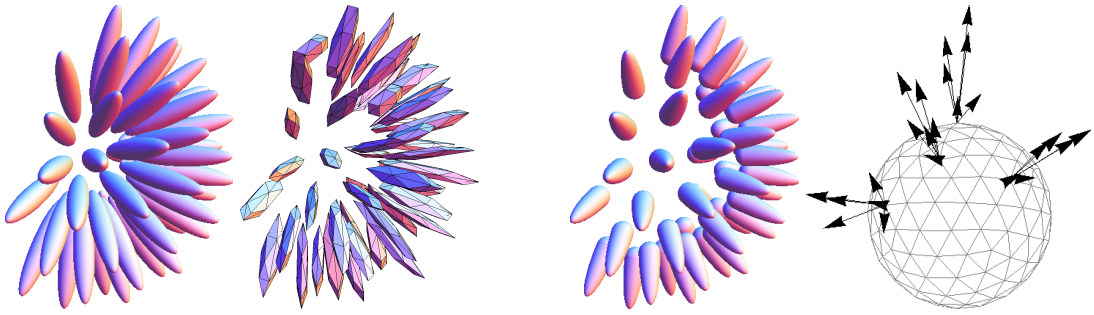

Fig. 10 Left: Slice in $\mathbb{R}^3$ of the control sets for $\mathcal{F}_\varepsilon$ on $\mathbb{R}^3 \times \mathbb{S}^2$, $\varepsilon = 0.2$, for different orientations of $\mathbf{n}$. Stencils obeying the generalized acuteness property required for Bellman type discretizations (44). Right: Slice in $\mathbb{R}^3$ of the control sets for $\mathcal{F}_\varepsilon^+$, $\varepsilon = 0.2$. Offsets used for the finite differences discretization (48), for four distinct orientations $\mathbf{n}$.

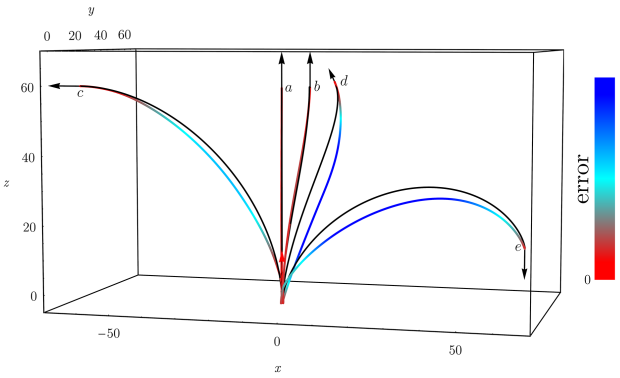

Fig. 11 Comparison of exact geodesics (black curves) and their numerical approximation (colored curves), with $\xi = 1/64$ and $\varepsilon = .1$, for five different end conditions ($a = ((0,0,60),(0,0,1))$, $b = ((6.4,6.4,60),(0,0,1))$, $c = ((-60,0,60),(-1,0,0))$, $d = ((0,60,60),1/\sqrt{6}(-1,2,1))$, $e = ((60,60,10),(0,0,-1))$). The color indicates the error with the exact curve.

Direct approximation of the Hamiltonian. A new approach, not semi-Lagrangian, had to be developed for the model $\mathcal{F}_\varepsilon^+$ in dimension $d = 3$ due to our failure to construct viable (i.e. with a reasonably small number of reasonably small vertices) stencils obeying the generalized acuteness property in this case. This alternative approach is based on the following proposition.

Proposition 2 *Let $\mathbf{n} \in \mathbb{S}^{d-1}$, and let $\mathbf{w}_1, \cdots, \mathbf{w}_k \in \mathbb{R}^d$ and $\alpha_1, \cdots, \alpha_d \in \mathbb{R}^d_+$ be such that*

$$\forall \mathbf{v} \in \mathbb{R}^d,\ \sum_{i=1}^k \alpha_i |\mathbf{w}_i \cdot \mathbf{v}|^2 = |\mathbf{n} \cdot \mathbf{v}|^2 + \varepsilon^2 \|\mathbf{n} \times \mathbf{v}\|^2.$$
$$\forall 1 \le i \le k, \quad (\mathbf{n} \cdot \mathbf{w}_i) \ge 0. \tag{46}$$

Then $\forall \mathbf{v} \in \mathbb{R}^d$ the positive part of the scalar product $\mathbf{n} \cdot \mathbf{v}$ can be approximated as follows

$$(\mathbf{n}\cdot\mathbf{v})_+^2 \le \sum_{i=1}^k \alpha_i (\mathbf{w}_i \cdot \mathbf{v})_+^2 \le (\mathbf{n}\cdot\mathbf{v})_+^2 + \varepsilon^2 \|\mathbf{n}\times\mathbf{v}\|^2. \tag{47}$$

Proof. We may assume that $\alpha_i = 1$, for all $1 \le i \le k$, up to replacing $\mathbf{w}_i$ with $\sqrt{\alpha_i}\mathbf{w}_i$. Denote by $\mathbf{w}_i^\perp := \mathbf{w}_i - \langle \mathbf{w}_i, \mathbf{n}\rangle \mathbf{n}$ the orthogonal projection of $\mathbf{w}_i$ on the hyperplane orthogonal to $\mathbf{n}$. Then by (46)

$$\sum_{1\le i\le k} |\mathbf{n}\cdot\mathbf{w}_i|^2 = 1, \quad \sum_{1\le i\le k} \mathbf{w}_i^\perp \otimes \mathbf{w}_i^\perp = \varepsilon^2 (\mathrm{Id} - \mathbf{n}\otimes\mathbf{n}).$$

Split the proof in two parts, depending on the sign of $(\mathbf{n}\cdot\mathbf{v})$. If $(\mathbf{n}\cdot\mathbf{v})\leq 0$, then $(\mathbf{w}_i\cdot\mathbf{v})\leq(\mathbf{w}_i^{\perp}\cdot\mathbf{w})$ for all $1\leq i\leq k$, thus as announced

$$\sum_{1\leq i\leq k}(\mathbf{w}_i\cdot\mathbf{v})_+^2\leq\sum_{1\leq i\leq k}(\mathbf{w}_i^{\perp}\cdot\mathbf{v})_+^2\leq\sum_{1\leq i\leq k}|\mathbf{w}_i^{\perp}\cdot\mathbf{v}|^2 = \varepsilon^2\|\mathbf{n}\wedge\mathbf{v}\|^2.$$

In contrary if $(\mathbf{n}\cdot\mathbf{v})\geq 0$, then the RHS of (47) is immediate, and in addition $(\mathbf{w}_i\cdot\mathbf{v})_+^2\geq|\mathbf{w}_i\cdot\mathbf{v}|^2-|\mathbf{w}_i^{\perp}\cdot\mathbf{v}|^2$ for any $1\leq i\leq k$. (Indeed, if $(\mathbf{w}_i\cdot\mathbf{v})\geq 0$ then $(\mathbf{w}_i\cdot\mathbf{v})_+^2=|\mathbf{w}_i\cdot\mathbf{v}|^2\geq|\mathbf{w}_i\cdot\mathbf{v}|^2-|\mathbf{w}_i^{\perp}\cdot\mathbf{v}|^2$, and in contrary if $(\mathbf{w}_i\cdot\mathbf{v})\leq 0$ we get $(\mathbf{w}_i\cdot\mathbf{v})_+^2=0\geq|\mathbf{w}_i\cdot\mathbf{v}|^2-|\mathbf{w}_i^{\perp}\cdot\mathbf{v}|^2$.) Hence, we conclude

$$\sum_{1\leq i\leq k}(\mathbf{w}_i\cdot\mathbf{v})_+^2\geq\sum_{1\leq i\leq k}|\mathbf{w}_i\cdot\mathbf{v}|^2-|\mathbf{w}_i^{\perp}\cdot\mathbf{v}|^2=|\mathbf{n}\cdot\mathbf{v}|^2.\ \square$$

We choose *integral* vectors $\mathbf{w}_i\in\mathbb{Z}^d$ obeying (46, left) using the construction of [27], which relies on the concept of obtuse superbase of a lattice. Thus for any smooth $U:\mathbb{R}^d\to\mathbb{R}$, and any $\mathbf{p}=(\mathbf{x},\mathbf{n})\in\mathbb{M}$, one gets the approximation

$$\begin{aligned}&(\mathbf{n}\cdot\nabla_{\mathbb{R}^d}U(\mathbf{p}))_+^2\\&\leq h^{-2}\sum_{i=1}^{k}\alpha_i(U(\mathbf{x},\mathbf{n})-U(\mathbf{x}-h\mathbf{w}_i,\mathbf{n}))_+^2+\mathcal{O}(h)\quad(48)\\&\leq(\mathbf{n}\cdot\nabla_{\mathbb{R}^d}U(\mathbf{p}))_+^2+\varepsilon^2\|\mathbf{n}\times\nabla_{\mathbb{R}^d}U(\mathbf{p})\|^2.\end{aligned}$$

From this point, one easily constructs an expression $\mathfrak{F}_\varepsilon U(\mathbf{p})$ bounded below by $\mathcal{F}_0^{+*}(\mathbf{p},\mathrm{d}U(\mathbf{p}))^2$ and above by $\mathcal{F}_\varepsilon^{+*}(\mathbf{p},\mathrm{d}U(\mathbf{p}))^2$ up to the discretization error $\mathcal{O}(h)$, and involving only the positive part $(U(\mathbf{p})-U(\mathbf{q}))_+$ of finite differences. For any $\mathbf{p}\in X$, the quantity $\mathfrak{F}_\varepsilon U(\mathbf{p})$ is a non-decreasing and piecewise quadratic function $f_{\mathbf{p}}$ of the variable $U(\mathbf{p})$ (other values $U(\mathbf{q})$, $\mathbf{q}\neq\mathbf{p}$, kept constant). In the spirit of [45], we let $\mathit{\Lambda}U(\mathbf{p})$ be the unique solution $\lambda\in\mathbb{R}$ to $f_{\mathbf{p}}(\lambda)=1$, which yields the desired causal scheme. Convergence analysis is postponed to future works for manuscript size reasons. Note that this approach could also be applied in dimension $d=2$, and to the symmetric model featuring a reverse gear.

We present only a single assessment of the numerical performance of our method, see Fig. 11. We compare numerically obtained shortest paths with exact SR geodesics for a small number of end points, that correspond to various types of curves. For fair end conditions (a, b, c) the numerical curves are close the exact curves. For very challenging end conditions inducing torsion (d) or extreme curvature (e) the curves are further from the exact SR geodesics. An extensive evaluation of the performance of the numerics is left for future work.

7 Applications

To show the potential of anisotropic fast marching for path-tracing in 2D and 3D (medical) images we performed experiments on each of the datasets in Fig. 2: a 2D toy example using a map of Centre Pompidou, a 2D retinal image, and two synthetic Diffusion-weighted Magnetic Resonance Imaging (dMRI) datasets. We use the 2D datasets to point out the difference in results when using the metric $\mathcal{F}_\varepsilon$ and $\mathcal{F}_\varepsilon^+$, and to explain the role of the keypoints when using $\mathcal{F}_\varepsilon^+$, that occur instead of (possibly unwanted) cusps.

On the synthetic dMRI datasets we present the first application of our methods to this type of data. We present how a cost function can be extracted from the data, and how this leads to correct tracking of bundles, similar to the 2D case. The benefits of anisotropic metrics compared to isotropic metrics are demonstrated by performing backtracking for various model parameter variations.

The experiments were performed using an anisotropic FM implementation written in C++, for $d=2$ described in [37]. Implementation details for $d=3$ will be described in future work. Mathematica 11.0 (Wolfram Research, Inc., Champaign, IL) was used for further data analysis, applying Wolfram LibraryLink (Wolfram Research, Inc., Champaign, IL) to interface with the FM library.

7.1 Applications in 2D

7.1.1 Shortest Path to the Exit in Centre Pompidou

To illustrate the difference between the models with and without reverse gear and show the role of the keypoints for non-uniform cost, we use a map of Centre Pompidou as a 2D image, see Fig. 12. The walls (in black) have infinite cost, everywhere else the cost is 1. We place end points (black dots) in various places of the museum and look for the shortest path from those points to one of the two exits, regardless of the end orientation. Since there are now two exits, say at $\mathbf{p}_0$ and $\mathbf{p}_1$, the distance $U(\mathbf{p})$ of any point $\mathbf{p}\in\mathbb{M}$ to one of the exits is given by

$$U_{\mathcal{F}}(\mathbf{p})=\min\{d_{\mathcal{F}}(\mathbf{p}_0,\mathbf{p}),d_{\mathcal{F}}(\mathbf{p}_1,\mathbf{p})\}.\quad(49)$$

We use a resolution of $N_x\times N_y\times N_o=706\times441\times60$. The cost in this example is only dependent on position, but constant in the orientation. Moreover, we use $\mathcal{C}_1=\mathcal{C}_2$ and $\varepsilon=1/10$.

On the left of Fig. 12 we see optimal paths (in blue) obtained using the metric $\mathcal{F}_\varepsilon$. The fast marching algorithm succesfully connects all end points to one of

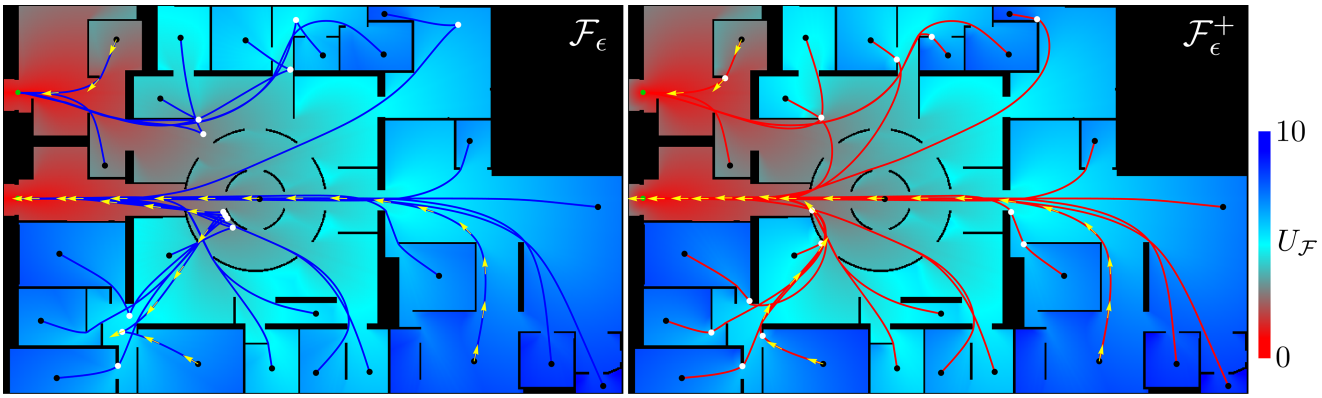

Fig. 12 Comparison between the shortest paths from end points (black) to one of the exits (green) in a model map of Centre Pompidou, for cars with (left, blue lines) and without (right, red lines) reverse gear. The yellow arrows indicate the orientation of the curve. The background colors show the distances at each position, minimized over the orientation. White points left indicate the cusps, white points right indicate the (automatically placed) key points where in-place rotations take place.

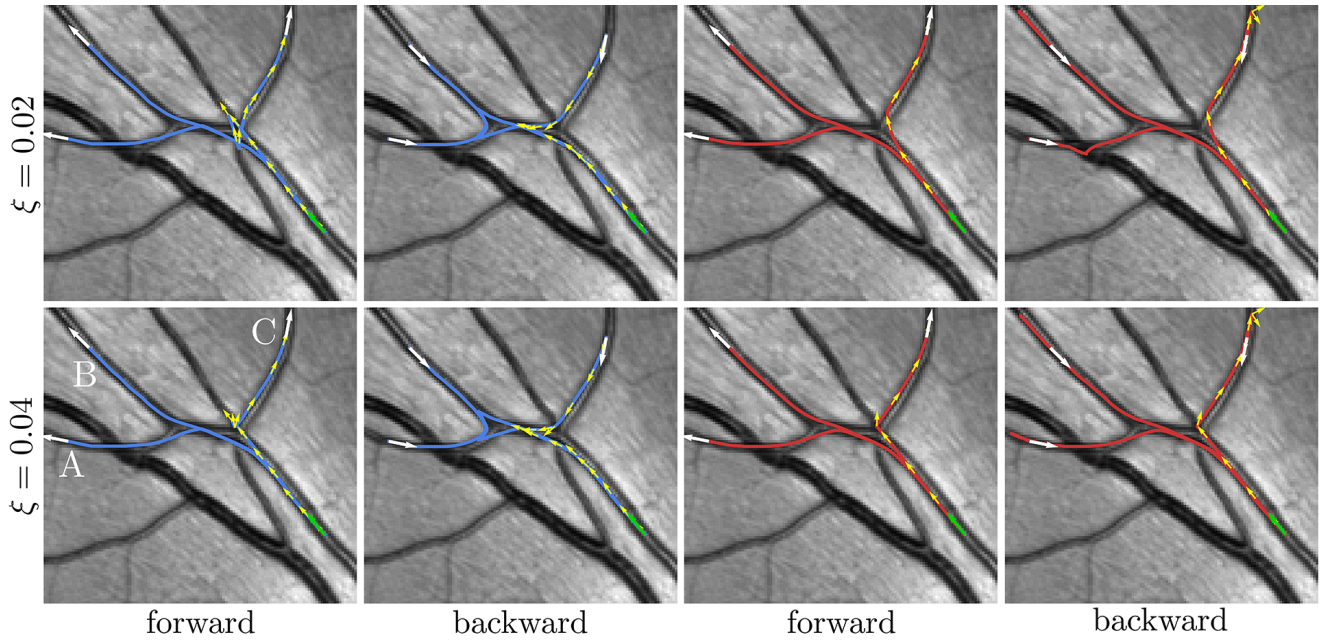

Fig. 13 Left: SR geodesics (in blue) in $(\mathbb{M}, d_{\mathcal{F}_0})$ with given boundary conditions (both forward and backward). Right: SR geodesics (in red) in $(\mathbb{M}, d_{\mathcal{F}_0^+})$ with the same boundary conditions. We recognize one end-condition case where on the left we get a cusp, whereas on the right we have a key-point (with in-place rotation) precisely at the bifurcation.

the exits. Some of the geodesics have cusps, indicated with white points, resulting in backward motion on (a part of) the curve. The colors show the distance $U_{\mathcal{F}_\varepsilon}$ as above, at each position minimized over the orientations.

On the right, the optimal paths using the asymmetric metric $\mathcal{F}_\varepsilon^+$ are shown in red. The curves no longer exhibit cusps, but have in-place rotations (white dots) instead. These keypoints occur in this example on corners of walls. (Due to the fact that ε is small but nonzero, there can still be small sideways motion.) The shortest paths for this model are successions of sub-Riemannian geodesics and of in place rotations, which can be regarded as reinitializations of the former: the orientation is adapted until an orientation is found from which the path can continue in an optimal sub-Riemannian way. Note that the fast marching algorithm has no special treatment for keypoints, which are only detected in a post-processing step. Small differences in the distance maps between $U_{\mathcal{F}_\varepsilon}$ left and $U_{\mathcal{F}_\varepsilon^+}$ right can be observed: the constrained model usually has a slightly higher cost right around corners.

7.1.2 Vessel Tracking in Retinal Images

A more substantial application are retinal images, for which the model with reverse gear and the fast-

marching algorithm have shown to be useful in [7,47]. Although the algorithm works fast and led to successful vessel segmentation in many cases, in some cases, in particular bifurcations of vessels, cusps occur. Fig. 13 shows one such example on the left. The image has resolution $N_x \times N_y \times N_o = 121 \times 114 \times 64$. The cost is constructed as in [7]: the image is first lifted using cake wavelets [22], resulting in an image on $\mathbb{R}^2 \times S^1$. For the lifting and for the computation of the cost function from the lifted image, we rely on their parameter settings. We use $\mathcal{C}_1 = \xi \mathcal{C}_2$, with $\xi = 0.02$ (top) and $\xi = 0.04$, and $\varepsilon = 0.1$. The orientations of the end conditions A, B and C (white arrows) are chosen tangent to the vessel, where we considered both the forward and the backward case. The vessel with end condition C is particularly challenging, since it comes across a bifurcation. For the tracking of this vessel, we indicated the orientation with yellow arrows.

The unconstrained model, corresponding to the blue tracks on the left half of Fig. 13, gives a correct vessel tracking for the forward end conditions of A and B, for both values of ξ. This is obviously the better choice than the backward cases. However, for end condition C, neither the forward or backward with neither values of ξ gives a vessel tracking without cusps. On the other hand, if we use the constrained model, we obtain an in-place rotation or keypoint in the neighborhood of the bifurcation. Typically a higher value of ξ brings these points closer to the bifurcation. Taking the backward end conditions in combination with this model, we see in some cases that end locations are first passed by the vessel tracking algorithm, until it reaches a point where in-place rotation is cheaper, and then returns to the end position.

7.2 Application to Diffusion-Weighted MRI Data

DW-MRI is a magnetic resonance technique for non-invasive measurement of water diffusion in fibrous tissues [40]. In the brain, diffusion is less constrained parallel to white matter fibers (or axons) than perpendicular to them, allowing us to infer the paths of these fibers. The diffusion measurements are distributions $(\mathbf{y}, \mathbf{n}) \mapsto U(\mathbf{y}, \mathbf{n})$ within the manifold $\mathbb{M}$ for $d = 3$. From these measurements a fiber orientation distribution (FOD) can be created, which gives the probability of finding a fiber at a certain position and orientation [54].

Backtracking is performed through forward Euler integration of the backtracking PDE involving the intrinsic gradient, following Theorem 4 and Eq. (27) and Eq. (30). The spatial derivative was implemented as a first-order Gaussian derivative. The angular derivatives are implemented by a first-order spherical harmonic derivative. The latter has the key advantage that in a spherical harmonic basis exact analytic computations can be done. Here, one must rely on two-fold recursions in [26, Lemma 2 & 4], so that the poles due to a standard Euler angle parametrization of $\mathbb{S}^2$ do not appear in exact recursions of Legendre polynomials!

If data-driven factors $\mathcal{C}_1$ and $\mathcal{C}_2$ come in a spherical sampling or if one wants to work in a spherical sampling (e.g. higher order tesselation of the icosahedron) in a fast-marching method, than one can easily perform the pseudo-inverse of the discrete inverse spherical harmonic transform, where one typically keeps the number of spherical harmonics very close to the number of spherical sampling points, so that maximum accuracy order is maintained for computing angular derivatives in the intrinsic gradient descent of Theorem 4.

7.2.1 Construction of the Cost Function

The synthetic dMRI data is created by generating/simulating a Fiber Orientation Density (FOD) of a desired structure. There are sophisticated methods for this, e.g. [15,11], but evaluation on phantom data constructed with these tools is left for future work. Here we use a basic but practical method on two simple configurations of bundles in $\mathbb{R}^3$, the ones on the bottow row in 2. In each voxel inside a bundle, we place a spherical δ-distribution, with the peak in the orientation of the bundle. We convolve each δ-distribution with an FOD kernel that was extracted from real dMRI data and is related to the dMRI signal measured in a voxel with just a single orientation of fibers. Spherical rotation of the FOD kernel is done in the spherical harmonics domain by use of the Wigner D-matrix to prevent interpolation issues. We compose from all distributions an FOD function $W : \mathbb{M} \to \mathbb{R}^+$. This function evaluates to high values in positions/orientations that are inside and aligned with the bundle structure.

We use the FOD W to define the cost function $\frac{1}{1+\sigma} \leq \mathcal{C} \leq 1$ via

$$\mathcal{C}(\mathbf{p}) = \frac{1}{1 + \sigma \left| \frac{W_+(\mathbf{p})}{\|W_+\|_\infty} \right|^p}$$

where $\sigma \geq 0$, $p \in \mathbb{N}$, with $\| \cdot \|_\infty$ the sup-norm and $W_+(\mathbf{p}) = \max\{0, W(\mathbf{p})\}$. The cost function $\mathcal{C}$ is related to the spatial and angular cost functions $(\mathcal{C}_1, \mathcal{C}_2)$ according to

$$\mathcal{C}_1(\mathbf{p}) = \xi \mathcal{C}(\mathbf{p}), \qquad \mathcal{C}_2(\mathbf{p}) = \mathcal{C}(\mathbf{p}).$$

The implementation of nonuniform cost is comparable to the application to fundus images in $d = 2$ by Bekkers et al. [7].

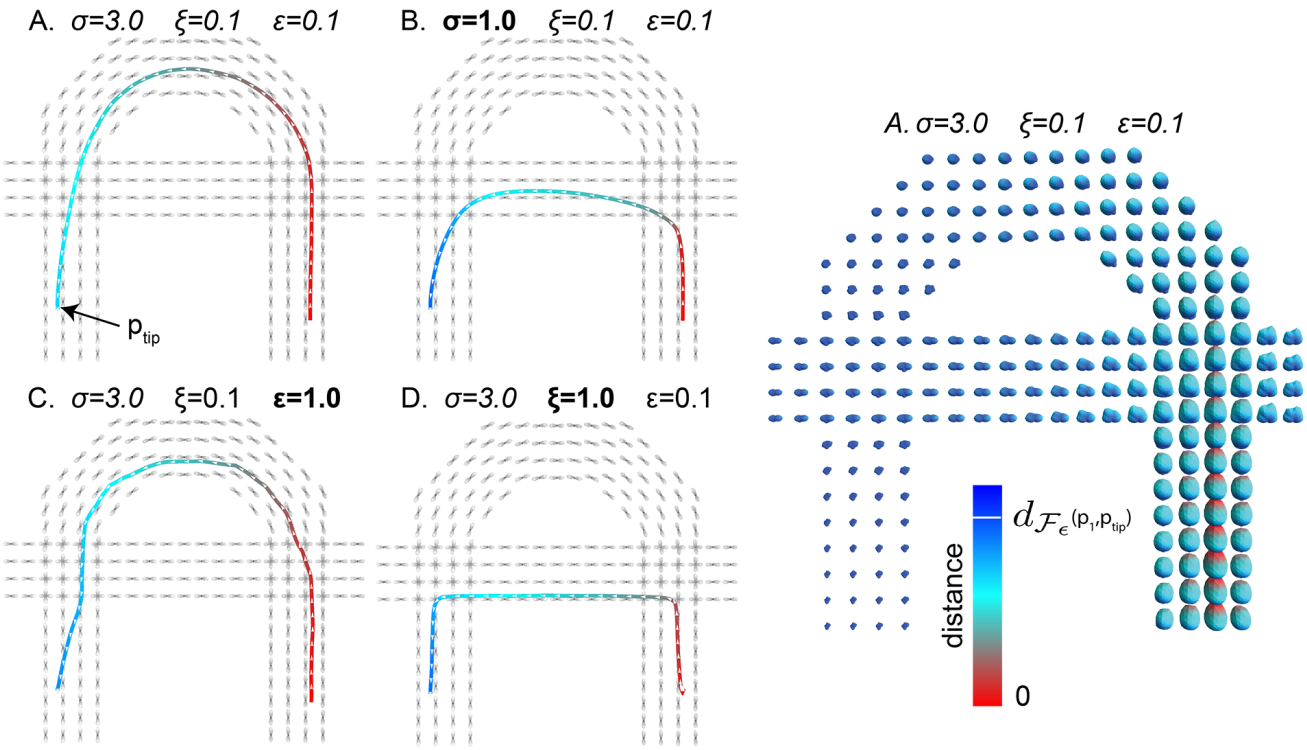

Fig. 14 Comparison of the results of backtracking on a 2D plane in a synthetic dMRI dataset on $\mathbb{M} = \mathbb{R}^3 \times \mathbb{S}^2$. In case A the default parameters for σ, ξ and ε are applied resulting in a global minimizing geodesic (left) and its corresponding distance map (right). Case B reflects the influence of the data-term σ. Case C reflects the isotropic Riemannian case. Case D reflects a high cost for moving spatially and results in curves that resemble a piecewise linear curve. The distance map is illustrated using a glyph visualization in which the size of the glyph corresponds to $exp(-d_{\mathcal{F}_\varepsilon}(\mathbf{p}_1, \mathbf{p}_2)/s)^p$ where $\mathbf{p}_1$ is the seed location, $\mathbf{p}_2$ is a location on a glyph, and s and p are chosen based on visualization clarity.

7.2.2 Influence of model parameters (Synthetic 2D dataset)

The first synthetic dataset consists of a curved and a straight vessel, which cross at two locations as shown in Fig. 14. The experiments demonstrate the effect on the geodesic back-traced from the bottom-left to the seed location at the bottom-right of the curved vessel. A distance map is computed for parameter configuration A (Fig. 14, right) in which suitable values are used for the data-term σ, and the fast-marching parameters ξ and ε. Furthermore, fixed values are used for data sharpening $p = 3$, spatial smoothing $\sigma s = 0.5$, forward-Euler integration step size $\delta t = 0.04$, and a gridscale of 1. By use of these parameters the global minimizing geodesic (Fig. 14.A, left) is shown to take the longer, curved route. In parameter configuration B the data-term σ is lowered, which creates a geodesic that is primarily steered by internal curve-dependent costs and is shown to take the shortcut route (Fig. 14.B). Setting $\varepsilon = 1$ in configuration C leads to a Riemannian case where the geodesic resembles a piecewise linear curve. In configuration D the relative cost of spatial movement relative to angular movement is high, leading to geodesics with corners.

We conclude that configuration **A** with a relatively strong data term, large bending stiffness ($\xi^{-1} = 10$), and a nearly SR geometry ($\varepsilon = 0.1$) yields best results.

7.2.3 Positive control constraint (Synthetic 2D dataset)

For the application of FM to the dMRI application it is desirable that the resulting geodesic is not overly sensitive to the boundary conditions, i.e. the placement and orientation of the geodesic tip. Furthermore, since neural fibers do not form cusps, these are undesirable in the backtracking results. In Fig. 15 the backtracking results are shown for the cases without reverse gear $\mathcal{F}_\varepsilon^+$ (top) and the model with reverse gear $\mathcal{F}_\varepsilon$ (bottom). The distance map for $\mathcal{F}_\varepsilon^+$ was computed by the iterative method implementing the forward Reeds-Shepp car, while for $\mathcal{F}_\varepsilon$ the FM method was used.

We conclude that without the positive control constraint, small changes in tip orientation cause large variations in the traced geodesic in $(\mathbb{M}, d_{\mathcal{F}_\varepsilon})$, whereas the

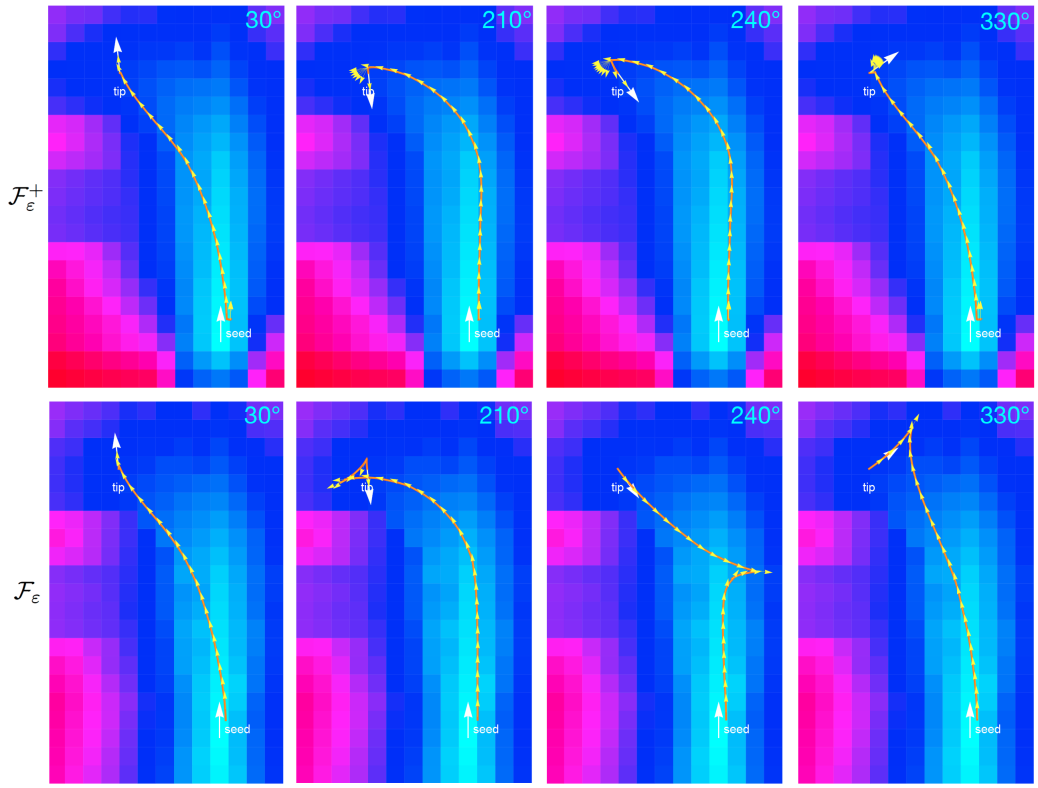

Fig. 15 The backtracking results for optimal geodesics of the model $(\mathbb{M}, d_{\mathcal{F}_\varepsilon^+})$ without reverse gear (top) and the model with reverse gear $(\mathbb{M}, d_{\mathcal{F}_\varepsilon})$ (bottom) using the model parameters of configuration A ($\sigma = 3.0$, $\xi = 0.1$ and $\varepsilon = 0.1$) for various end conditions.

traced geodesic in $(\mathbb{M}, d_{\mathcal{F}_\varepsilon^+})$ is both more stable and more reasonable.

7.2.4 Robustness to neighboring structures (Synthetic 3D dataset)

A pitfall of methods that provide globally optimal curves using a dataterm is that dominant structures in the data attract many of the curves, much like the highway usually has the preference for cars rather than local roads. This phenomenon is to a certain extent unwanted in our applications, and we illustrate with the following example that it can be circumvented using a sub-Riemannian instead of Riemannian metric. We use the dataset as introduced in Fig. 2. It consists of one bundle that has torsion (green), that crosses with another bundle (blue), and a third bundle (red) that is parallel with the first in one part. The cost in these bundles is constructed in the same way as above, but now the cost in the red bundle is twice as low as in the other bundles. A small part of the data is visualized on the left of Fig. 16. This data is used to construct the cost function as explained above.

The resolution of the data is $N_x \times N_y \times N_z \times N_o = 32 \times 32 \times 32 \times 162$. Again we use $\mathcal{C}_1 = \xi \mathcal{C}_2$, with $\xi = 0.1$. To have comparable parameters as in the previous experiment, despite increasing the amplitude in one of the bundles by a factor 2, we choose to construct the cost using parameter $p = 3$, and $\sigma = 3 \cdot 2^p = 24$. From various places inside the green, blue and red bundle, the shortest paths to the end of the bundles computed by the FM algorithm nicely follow the shape of the actual bundles, when we choose $\varepsilon = .1$ small, corresponding to an almost SR geodesic. This is precisely what prevents the geodesic in the green bundle to drift into the (much cheaper) red bundle. We show on the right in Fig. 16 that choosing $\varepsilon = 1$, corresponding to having an isotropic Riemannian metric, this unwanted behavior can occur.

8 Conclusion and Discussion

We have extended the existing methodology for modelling and solving the problem of finding optimal paths for a Reeds-Shepp car to 3D and to a case without reverse gear. We have shown that the use of the constrained model leads to more meaningful shortest paths in some cases and that the extension to 3D has opened up the possibility for tractography in dMRI data.

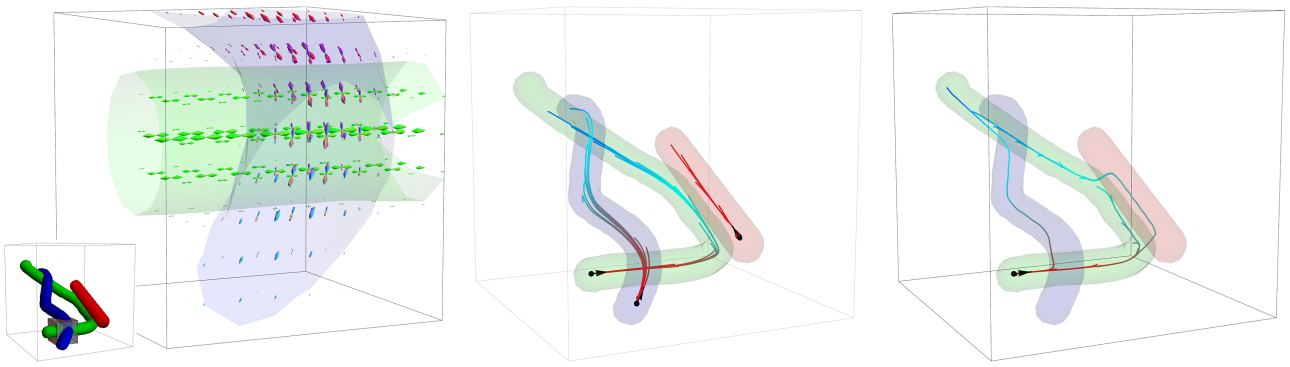

Fig. 16 Left: 3D configuration of bundles and a visualization of part of the synthetic dMRI data. Middle: backtracking of geodesics in $(\mathbb{M}, d_{\mathcal{F}_\varepsilon})$ from several points inside the curves to end points of the bundle is successful when using $\varepsilon = 0.1$. Right: when using $\varepsilon = 1$, the dominant red bundle can cause the paths from the green bundle to deviate from the correct structure.

Instead of using a hard constraint on the curvature as in the original paper by Reeds and Shepp [44], we used Riemannian/Finslerian metrics. We have introduced these metrics, $\mathcal{F}_0$ and $\mathcal{F}_0^+$, for $d = 2, 3$, such that they allow for curves that have a spatial displacement proportional to the orientation, with a positive proportionality constant in the case of $\mathcal{F}_0^+$.

We have captured theoretically some of the nature of the distance maps and geodesics following from the new constrained model. We have shown that both models are globally controllable, but only the unconstrained model is also locally controllable.

We have analyzed cusps in $(\mathbb{M}, d_{\mathcal{F}_0})$ and keypoints in $(\mathbb{M}, d_{\mathcal{F}_0^+})$ which occur on the interface surface $\partial\mathbb{M}_\pm$ given by (29). The analysis, for uniform costs, is summarized in Theorem 3. We have shown that cusps are absent in $(\mathbb{M}, d_{\mathcal{F}_\varepsilon})$ for $\varepsilon > 0$, that keypoints in $(\mathbb{M}, d_{\mathcal{F}_0^+})$ occur only on the boundary, and we provided analysis on how this happens depending on the boundary conditions.

The sub-Riemannian and sub-Finslerian nature is difficult to capture numerically. To this end, we introduced approximating metrics $\mathcal{F}_\varepsilon$ and $\mathcal{F}_\varepsilon^+$, that do allow for numerical approaches. We have shown that as $\varepsilon \to 0$, the distance map converges pointwise and the geodesics converge uniformly, implying that for sufficiently small ε we indeed have a reasonable approximation of the $\varepsilon = 0$ case.

To obtain solutions for the distance maps and optimal paths, we used a Fast-Marching method. By formulating an equivalent problem to the minimization problem for optimal paths in the form of an eikonal equation, the FM method can be used using specific discretization schemes. We briefly compared the numerical solutions using $\mathcal{F}_\varepsilon$ with $\varepsilon \ll 1$ with the exact sub-Riemannian geodesics in SE(2) with uniform cost, which showed sufficient accuracy for not too extreme begin and end conditions.

To show the use of our method in image analysis, we have tested it on two 2D problems and two 3D problems. All four experiments confirm that the combination of the eikonal PDE formulation, the Fast-Marching method and the construction of the non-uniform cost from the images, results in geodesics that follow the desired paths. From the experiment on an image of Centre Pompidou, with constant, finite cost everywhere except for the walls, it followed that instead of having cusps when using the $\mathcal{F}_\varepsilon$ metric, we get keypoints (in-place rotations) when using $\mathcal{F}_\varepsilon^+$. These keypoints turn out to be located on logical places in the image. On the 2D retinal image we showed that the metric $\mathcal{F}_\varepsilon^+$ gives a new tool for tackling vessel tracking through bifurcations. We see that keypoints appear close to the bifurcation, leading to paths that more correctly follow the data.

The basic experiments on 3D show advantages of the model $(\mathbb{M}, d_{\mathcal{F}_\varepsilon})$ with $0 < \varepsilon \ll 1$ over the model $(\mathbb{M}, d_{\mathcal{F}_1})$ in the sense that the optimal geodesics better follow the curvilinear structure and deal with crossings and nearby parallel bundles (even if torsion is present). Furthermore, we have shown the advantage of model $(\mathbb{M}, d_{\mathcal{F}_\varepsilon^+})$ with $0 < \varepsilon \ll 1$, compared to $(\mathbb{M}, d_{\mathcal{F}_\varepsilon})$ in terms of stability, with keypoints instead of cusps.

The strong performance of the Reeds-Shepp car model in 2D vessel tracking and positive first results on artificial dMRI data, encourages us to pursue a more quantitative assessment of the performance in both 3D vessel tracking problems and in actual dMRI data. Such 3D vessel tracking problems are encountered in for example Magnetic Resonance Angiography. In future work we will elaborate on the implementation and evaluation of the fast-marching and the iterative PDE implementation of App. B. Furthermore, we aim to inte-

grate locally adaptive frames [25] into the Finsler functions $\mathcal{F}_\varepsilon$, $\mathcal{F}_\varepsilon^+$, for a more adaptive vessel/fiber tracking.

9 Acknowledgements

The authors gratefully acknowledge dr. G.R. Sanguinetti (industrial design engineer at ASML) for fruitful discussion and ideas leading up to this article. We thank E.J. Bekkers for his assistance with and suggestions for Fig. 13. The research leading to the results of this article has received funding from the European Research Council under the European Communitys 7th Framework Programme (FP7/20072014)/ERC grant agreement No. 335555. This work was partly funded by ANR grant NS-LBR. ANR-13-JS01-0003-01.

A Well-posedness and convergence of the Reeds-Shepp models

We introduce in §A.1 some general elements of control theory, which are specialized in §A.2 to the Reeds-Shepp models and their approximations.

A.1 Closedness of controllable paths

In this section, we introduce the notion of admissible path γ with respect to some controls $\mathfrak{B}$. We state in Theorem 5 a closedness result, slightly generalizing the one from [18], from which we deduce in Corollaries 3 and 4 an existence and a convergence result for a minimum time optimal control problem. The first ingredient of this approach is the notion of Haussdorff distance on a metric space.

Definition 5 Given a metric space $\mathbb{E}$, we let $\mathcal{K}(\mathbb{E})$ be the collection of non-empty compact subsets of $\mathbb{E}$. The distance function $d_A : \mathbb{E} \to \mathbb{R}_+$ and the Haussdorff distance $\mathcal{H}(A,B)$, where $A, B \in \mathcal{K}(\mathbb{E})$, are defined respectively by

$$d_A(x) := \inf_{y\in A} d(x,y)$$
$$\mathcal{H}(A,B) := \max\{\sup_{x\in B} d_A(x),\ \sup_{x\in A} d_B(x)\}.$$

In the following, we fix a closed set $\mathbb{X}$, contained in an euclidean vector space $\mathbb{E}$, or in a complete Riemannian manifold $\mathbb{M}$. In the applications considered in this paper, $\mathbb{X}$ is of the form $\mathbb{X}_0 \times \mathbb{S}^{d-1}$, where $\mathbb{X}_0 \subset \mathbb{R}^d$ is some image domain, see Fig. 13, or the set of accessible points in a map (which excludes the walls), see Fig. 12. The embedding space can be the vector space $\mathbb{E} = \mathbb{R}^d \times \mathbb{R}^d$, which is an acceptable but rather extrinsic point of view, or the Riemannian manifold $\mathbb{M} = \mathbb{R}^d \times \mathbb{S}^{d-1}$, equipped with the metric $\mathcal{G}_\varepsilon$ for some arbitrary but fixed $\varepsilon > 0$, see (24).

We equip the collection of all Lipschitz paths $\Gamma := \mathrm{Lip}([0,1],\mathbb{X})$ with the topology of uniform convergence. We will make use of Ascoli's lemma [4,3], which states that any uniformly bounded and equicontinuous sequence of paths admits a converging sub-sequence. In our case the paths are Lipschitz with a common Lipschitz constant.

Definition 6 Given a normed vector space V, we denote by $\mathfrak{C}(V) \subset \mathcal{K}(V)$ the collection of non-empty compact subsets of V, which are in addition convex and contained in the unit ball.

Remark 13 The restriction to convex subsets is essential. For a uniformly converging sequence of Lipschitz functions $\gamma_n : [0,1] \to \mathbb{M}$ with limit γ_*, with $\dot\gamma_n(t) \in K$ for a.e. $t \in [0,1]$ and K a compact set, we can deduce that $\dot\gamma_* \in \mathrm{Hull(K)}$, for a.e. $t \in [0,1]$. The convexity then guarantees that $\dot\gamma_* \in K = \mathrm{Hull(K)}$.

Definition 7 A family of controls $\mathcal{B}$ on the set $\mathbb{X}$ is an element of the set $\mathfrak{B}$ defined by

- If $\mathbb{X} \subset \mathbb{E}$ an Euclidean vector space, then $\mathfrak{B} := C^0(\mathbb{X}, \mathfrak{C}(\mathbb{E}))$.
- If $\mathbb{X} \subset \mathbb{M}$ a Riemannian manifold, then $\mathfrak{B} := \{\mathcal{B} \in C^0(\mathbb{X}, \mathcal{K}(T\mathbb{M}));\ \forall \mathbf{p} \in \mathbb{X},\ \mathcal{B}(\mathbf{p}) \in \mathfrak{C}(T_{\mathbf{p}}\mathbb{M})\}$.

In both cases, $\mathfrak{B}$ is equipped with the topology of locally uniform convergence.

Definition 8 A path γ is $T\mathcal{B}$-admissible, where $\gamma \in \Gamma$, $T \in \mathbb{R}_+$ and $\mathcal{B} \in \mathfrak{B}$, iff for almost every $t \in [0,1]$

$$\dot\gamma(t) \in T\mathcal{B}(\gamma(t)).$$

We denoted $TB := \{T\mathbf{v};\ \mathbf{v} \in B\}$, where $T \in \mathbb{R}_+$ and B is a subset of a vector space. Note the potential conflict of notation with the tangent space $T\mathbb{M}$ to the embedding manifold $\mathbb{M}$, which should be clear from context. If a path γ is $T\mathcal{B}$-admissible for some controls $\mathcal{B} \in \mathfrak{B}$, then it must be T-Lipschitz. The following result slightly extends, for our convenience, Corollary A.5 in [18].

Theorem 5 *The set* $\{(\gamma, T, \mathcal{B}) \in \Gamma \times \mathbb{R}_+ \times \mathfrak{B};$ γ *is* $T\mathcal{B}$*-admissible*$\}$ *is closed.*

Proof. Let $(\gamma_n, T_n, \mathcal{B}_n)$ be sequences of paths, times and controls converging to $(\gamma_\infty, T_\infty, \mathcal{B}_\infty)$, and such that γ_n is $T_n\mathcal{B}_n$-admissible for all $n \geq 0$. Since the paths γ_n are converging as $n \to \infty$, they lay in a common compact subset $\mathbb{X}'$ of the closed domain $\mathbb{X}$, recall Remark 13. As a result, the restricted controls $\mathcal{B}'_n := (\mathcal{B}_n|_{\mathbb{X}'})$ are uniformly converging as $n \to \infty$. In the case where $\mathbb{X} \subset \mathbb{E}$ an euclidean space, applying Corollary A.5 in [18] to the sequence $(\gamma_n, T_n\mathcal{B}'_n)$ we obtain that γ_∞ is $T_\infty\mathcal{B}_\infty$-admissible as announced.

In the case where $\mathbb{X} \subset \mathbb{M}$ a Riemannian manifold, an additional proof ingredient is required. Let $\mathbb{M}'$ be an open neighborhood of $\mathbb{X}'$ with compact closure in $\mathbb{M}$, and let $\mathcal{I} : \mathbb{M}' \to \mathbb{E}$ be an embedding (i.e. an injective immersion) with bounded distortion of the manifold $\mathbb{M}'$ into a Euclidean space $\mathbb{E}$ of sufficiently high dimension, which by Whitney's embedding theorem is known to exist. Define the set $\mathbb{X}'' := \mathcal{I}(\mathbb{X}')$, the paths $\gamma''_n := \mathcal{I} \circ \gamma_n$, and controls $\mathcal{B}''_n(\mathcal{I}(\mathbf{p})) := \mathrm{d}\mathcal{I}(\mathbf{p}, \mathcal{B}_n(\mathbf{p}))$ for all $\mathbf{p} \in \mathbb{X}'$ and $n \in \mathbb{N} \cup \{\infty\}$. Applying again Corollary A.5 in [18] we obtain that γ''_∞ is $T_\infty\mathcal{B}''_\infty$ admissible, hence that γ_∞ is $T_\infty\mathcal{B}_\infty$-admissible as announced. □

Definition 9 For any $\mathcal{B} \in \mathfrak{B}$, $\mathbf{p}, \mathbf{q} \in \mathbb{X}$, we let

$$T_{\mathcal{B}}(\mathbf{p},\mathbf{q}) := \inf\{T \geq 0;\ \exists \gamma \in \Gamma,\ \gamma(0) = \mathbf{p},\ \gamma(1) = \mathbf{q},\ \text{and } \gamma \text{ is } T\mathcal{B}\text{-admissible}\}. \quad (50)$$

Corollary 3 *If* $\mathcal{B} \in \mathfrak{B}$, $\mathbf{p}, \mathbf{q} \in \mathbb{X}$ *are such that* $T_{\mathcal{B}}(\mathbf{p},\mathbf{q}) < \infty$*, then the inf.* (50) *is attained.*

Proof. Let $T := T_{\mathcal{B}}(\mathbf{p},\mathbf{q})$, and for each $0 < \varepsilon \leq 1$ let γ_ε be a $(T+\varepsilon)\mathcal{B}$-admissible path from $\mathbf{p}$ to $\mathbf{q}$, which is thus $(T+1)$-Lipschitz. By Arzela-Ascoli's lemma [3,4] there exists a converging sequence of paths $\gamma_{\varepsilon_n} \to \gamma_0$ as $n \to \infty$. The limit path γ_0 is $T\mathcal{B}$-admissible by Theorem 5, and the result follows. □

Corollary 4 *For all $\varepsilon \in [0,1]$ let $\mathcal{B}_\varepsilon \in \mathfrak{B}$. Assume that $\mathcal{B}_\varepsilon \to \mathcal{B}_0$ as $\varepsilon \to 0$, and that $\mathcal{B}_\varepsilon(\mathbf{p}) \supset \mathcal{B}_0(\mathbf{p})$ for all $\varepsilon \geq 0$, $\mathbf{p} \in \mathbb{X}$. Then*

$$T_{\mathcal{B}_\varepsilon}(\mathbf{p},\mathbf{q}) \to T_{\mathcal{B}_0}(\mathbf{p},\mathbf{q}), \quad \text{as } \varepsilon \to 0.$$

Let $T_\varepsilon := T_{\mathcal{B}_\varepsilon}(\mathbf{p},\mathbf{q})$ for each $\varepsilon \geq 0$. Assume in addition that there exists a unique $T_0\mathcal{B}_0$-admissible path γ_0 from $\mathbf{p}$ to $\mathbf{q}$, and for each $\varepsilon > 0$ denote by γ_ε an arbitrary path from $\mathbf{p}$ to $\mathbf{q}$ which is $(\varepsilon + T_\varepsilon)\mathcal{B}_\varepsilon$ admissible. Then $\gamma_\varepsilon \to \gamma_0$ as $\varepsilon \to 0$.

Proof. The inclusion $\mathcal{B}_\varepsilon(\mathbf{p}) \subset \mathcal{B}_0(\mathbf{p})$, $\forall \mathbf{p} \in \mathbb{M}$, implies the inequality $T_\varepsilon \leq T_0$, for all $\varepsilon \geq 0$. Denoting $T_* := \limsup T_\varepsilon$ as $\varepsilon \to 0$, we thus observe that $T_* \leq T_0$. For the reverse inequality $T_* \geq T_0$, we apply Arzela-Ascoli lemma to the family of paths $(\gamma_\varepsilon)_{0<\varepsilon\leq 1}$ which are (T_0+1)-Liptschitz by construction, and obtain a converging subsequence of paths $\gamma_{\varepsilon_n} \to \gamma_*$. Theorem 5 implies the admissibility of γ_* with respect to the controls $T_*\mathcal{B}_0$. Thus $T_* \geq T_0$ but since $T_* \leq T_0$, we must have $T_* = T_0$, and $\gamma_* = \gamma_0$ by uniqueness. The result follows. □

More generally, if the infimum (50) is realized by a family $(\gamma_i)_{i\in I}$ of paths, then for any sequence $\varepsilon_n \to 0$ one can find a subsequence such that $\gamma_{\varepsilon_{\varphi(n)}} \to \gamma_i$ as $n \to \infty$ for some $i \in I$.

A.2 Specialization to the Reeds-Shepp models

We begin this section by recalling, and slightly generalizing, the notion of Finsler function introduced in §2.2. We then prove that the Reeds-Shepp metrics $\mathcal{F}_0$ and $\mathcal{F}_0^+$ are indeed Finsler functions in this sense.

Definition 10 A metric on a complete Riemannian manifold $\mathbb{M}$ is a map $\mathcal{F} : T\mathbb{M} \to [0,+\infty]$. With respect to the second variable, it must be 1-homogeneous, convex, and bounded below by $\delta\|\cdot\|$, where δ is a positive constant. In terms of regularity, the sets $\mathcal{B}_\mathcal{F}(\mathbf{p}) := \{\dot{\mathbf{p}} \in T_\mathbf{p}\mathbb{M}; \mathcal{F}(\mathbf{p},\dot{\mathbf{p}}) \leq 1\}$ must be closed and depend continuously on $\mathbf{p} \in \mathbb{M}$ with respect to the Haussdorff distance on $T\mathbb{M}$.

The next proposition provides a dictionary from the language of metrics to and the language of Appendix A.1. It is a direct consequence of (8).

Proposition 3 *With the notations of Definition 10, the sets $\mathbf{p} \in \mathbb{M} \mapsto \mathcal{B}_\mathcal{F}(\mathbf{p})$ form a family of controls on $(\mathbb{M}, \delta\|\cdot\|)$. In addition for all $\mathbf{p},\mathbf{q} \in \mathbb{M}$*

$$d_\mathcal{F}(\mathbf{p},\mathbf{q}) = T_{\mathcal{B}_\mathcal{F}}(\mathbf{p},\mathbf{q}).$$

Proposition 4 *The Reeds-Shepp metrics $(\mathcal{F}_\varepsilon)_{0\leq\varepsilon\leq 1}$ and $(\mathcal{F}_\varepsilon^+)_{0\leq\varepsilon\leq 1}$ are indeed metrics in the sense of Definition 10, for any $\varepsilon \in [0,1]$. The associated controls $\mathcal{B}_\varepsilon := \mathcal{B}_{\mathcal{F}_\varepsilon}$, $\mathcal{B}_\varepsilon^+ := \mathcal{B}_{\mathcal{F}_\varepsilon^+}$ depend continuously on the parameter $\varepsilon \in [0,1]$, and satisfy the inclusions $\mathcal{B}_\varepsilon(\mathbf{p}) \subset \mathcal{B}_{\varepsilon'}(\mathbf{p})$ and $\mathcal{B}_\varepsilon^+(\mathbf{p}) \subset \mathcal{B}_{\varepsilon'}^+(\mathbf{p})$ for any $\mathbf{p} \in \mathbb{M}$ and $0 \leq \varepsilon \leq \varepsilon' \leq 1$.*

Proposition 4 allows to apply the results of §A.1 to the Reeds-Shepp metrics. Theorem 2 then directly follows from Corollary 4. The only remaining non-trivial claim in Proposition 4 is the continuity of the controls on $\mathbb{M}$, recall Definitions 7, and their convergence $\mathcal{B}_\varepsilon \to \mathcal{B}_0$ as $\varepsilon \to 0$, as required in Corollary 4. These two properties are implied by the continuity on $[0,1]\times\mathbb{M}$, that we next prove, of the following maps

$$[0,1]\times\mathbb{M} \ni (\varepsilon,\mathbf{p}) \to \mathcal{B}_\varepsilon(\mathbf{p}) \in \mathfrak{C}(T_\mathbf{p}\mathbb{M}),$$
$$[0,1]\times\mathbb{M} \ni (\varepsilon,\mathbf{p}) \to \mathcal{B}_\varepsilon^+(\mathbf{p}) \in \mathfrak{C}(T_\mathbf{p}\mathbb{M}),$$

with $\mathfrak{C}(T_\mathbf{p}\mathbb{M})$ defined in Definition 6 and equipped with the Haussdorff distance.

Lemma 5 *Let B be a compact subset of a metric space $\mathbb{E}$, and let $\varphi \in C^0(B,\mathbb{E})$. Then*

$$\mathcal{H}(B,\varphi(B)) \leq \sup_{x\in B} d(x,\varphi(x)).$$

This basic lemma, stated without proof, is used in the next lemma to obtain an explicit estimate of the Haussdorf distance between the controls sets of the Reeds-Shepp models.

Lemma 6 *Let $\mathbf{n}_1,\mathbf{n}_2 \in \mathbb{S}^{d-1}$, let $a_1,a_2,b_1,b_2 \geq 1$, and let $\varepsilon_1,\varepsilon_2 \in [0,1]$. For each $i \in \{1,2\}$, let B_i be the collection of all $(\dot{\mathbf{x}},\dot{\mathbf{n}}) \in \mathbb{R}^d\times\mathbb{R}^d$ obeying*

$$\dot{\mathbf{n}}\cdot\mathbf{n}_i = 0,$$
$$\begin{cases} a_i^2\|\dot{\mathbf{n}}\|^2 + b_i^2\left(|\dot{\mathbf{x}}\cdot\mathbf{n}_i|^2 + \varepsilon_i^{-2}\|\dot{\mathbf{x}}\wedge\mathbf{n}_i\|^2\right) \leq 1, & \varepsilon_i > 0 \\ a_i^2\|\dot{\mathbf{n}}\|^2 + b_i^2|\dot{\mathbf{x}}\cdot\mathbf{n}_i|^2 \leq 1 \quad \textit{and} \quad \dot{\mathbf{x}}\wedge\mathbf{n}_i = 0, & \varepsilon_i = 0 \end{cases}$$

Then

$$\mathcal{H}(B_1,B_2) \leq |a_1^{-1}-a_2^{-1}| + |b_1^{-1}-b_2^{-1}| + \sqrt{2(1-\mathbf{n}_1\cdot\mathbf{n}_2)} + |\varepsilon_1-\varepsilon_2|. \tag{51}$$

The same estimate holds for the sets B_i^+, $i \in \{1,2\}$, defined by the inequalities

$$\dot{\mathbf{n}}\cdot\mathbf{n}_i = 0,$$
$$\begin{cases} a_i^2\|\dot{\mathbf{n}}\|^2 + b_i^2\left((\dot{\mathbf{x}}\cdot\mathbf{n}_i)_+^2 + \varepsilon_i^{-2}(\|\dot{\mathbf{x}}\wedge\mathbf{n}_i\|^2 + (\dot{\mathbf{x}}\cdot\mathbf{n}_i)_-^2)\right) \leq 1, & \textit{if } \varepsilon_i > 0, \\ a_i^2\|\dot{\mathbf{n}}\|^2 + b_i^2(\dot{\mathbf{x}}\cdot\mathbf{n}_i)_+^2 \leq 1 \quad \textit{and} \quad \dot{\mathbf{x}}\wedge\mathbf{n}_i = 0, \quad \dot{\mathbf{x}}\cdot\mathbf{n}_i \geq 0, & \textit{if } \varepsilon_i = 0. \end{cases}$$

Proof. It suffices to establish the announced estimate (51) when the tuples $(a_i,b_i,\mathbf{n}_i,\varepsilon_i)$, $i \in \{1,2\}$, differ by a *single* element of the four, and then to use the sub-additivity of the Haussdorff distance. In each case we apply Lemma 5 to a well chosen surjective map $\varphi : B_1 \to B_2$ (resp $\varphi^+ : B_1^+ \to B_2^+$).

- Case $a_1 \neq a_2$. Assume w.l.o.g. that $a_1 < \infty$, and observe that for all $(\dot{\mathbf{x}},\dot{\mathbf{n}}) \in B_1$ one has $a_1\|\dot{\mathbf{x}}\| \leq 1$, hence $\|a_1\dot{\mathbf{x}}/a_2 - \dot{\mathbf{x}}\| \leq |a_1^{-1}-a_2^{-1}|$. Choose $\varphi(\dot{\mathbf{x}},\dot{\mathbf{n}}) := (a_1\dot{\mathbf{x}}/a_2,\dot{\mathbf{n}})$.
- Case $b_1 \neq b_2$. As above, with $\varphi(\dot{\mathbf{x}},\dot{\mathbf{n}}) := (\dot{\mathbf{x}},b_1\dot{\mathbf{n}}/b_2)$, yielding upper bound $|b_1^{-1}-b_2^{-1}|$.
- Case $\mathbf{n}_1 \neq \mathbf{n}_2$. Let R be the rotation of $\mathbb{R}^d$ which maps $\mathbf{n}_1$ onto $\mathbf{n}_2$, in such a way that it maps the space orthogonal to the plane $\mathrm{Span}(\mathbf{n}_1,\mathbf{n}_2)$ onto itself. A simple calculation yields $\|R-\mathrm{Id}\| = 2\sin[\frac{1}{2}\cos^{-1}(\mathbf{n}_1\cdot\mathbf{n}_2)] = \sqrt{2(1-\mathbf{n}_1\cdot\mathbf{n}_2)}$. The result follows by choosing $\varphi(\dot{\mathbf{x}},\dot{\mathbf{n}}) := (R\dot{\mathbf{x}},R\dot{\mathbf{n}})$, so that $\|\varphi(\dot{\mathbf{x}},\dot{\mathbf{n}}) - (\dot{\mathbf{x}},\dot{\mathbf{n}})\| \leq \|R-\mathrm{Id}\|\sqrt{\|\dot{\mathbf{n}}\|^2+\|\dot{\mathbf{x}}\|^2} \leq \|R-\mathrm{Id}\|$ for all $(\dot{\mathbf{x}},\dot{\mathbf{n}}) \in B_1$ as announced.

– Case $\varepsilon_1 \neq \varepsilon_2$. Assume w.l.o.g. that $\varepsilon_1 > 0$, and consider the orthogonal projections

$$P_1(\dot{\mathbf{x}}) := (\dot{\mathbf{x}} \cdot \mathbf{n}_1)\mathbf{n}_1 \qquad P_1^{\perp}(\dot{\mathbf{x}}) := (\mathrm{Id} - P_1)(\dot{\mathbf{x}}).$$

Note that $P_1^{\perp}(\dot{\mathbf{x}}) \leq \varepsilon_1$ if $(\dot{\mathbf{x}}, \dot{\mathbf{n}}) \in B_1$, and that $\|\dot{\mathbf{x}}\| \leq \varepsilon_1$ if $(\dot{\mathbf{x}}, \dot{\mathbf{n}}) \in B_1^+$ and $\dot{\mathbf{x}} \cdot \mathbf{n}_1 \leq 0$. The result follows by choosing

$$\varphi(\dot{\mathbf{x}}, \dot{\mathbf{n}}) := \left(P_1(\dot{\mathbf{x}}) + \frac{\varepsilon_2}{\varepsilon_1} P_1^{\perp}(\dot{\mathbf{x}}), \dot{\mathbf{n}} \right),$$
$$\varphi^+(\dot{\mathbf{x}}, \dot{\mathbf{n}}) := \begin{cases} \varphi(\dot{\mathbf{x}}, \dot{\mathbf{n}}) & \text{if } \dot{\mathbf{x}} \cdot \mathbf{n}_1 \geq 0, \\ (\frac{\varepsilon_2}{\varepsilon_1}\dot{\mathbf{x}}, \dot{\mathbf{n}}) & \text{otherwise.} \end{cases}$$ □

Proof of Proposition 4. Since working with Haussdorff distances on the abstract tangent bundle $T\mathbb{M}$ is not very practical, we make use of the canonical embedding $\mathcal{I} : \mathbb{R}^d \times \mathbb{S}^{d-1} \to \mathbb{R}^d \times \mathbb{R}^d$ of the manifold $\mathbb{M}$ into the Euclidean vector space $\mathbb{R}^{2d}$ given by $(\mathbf{x}, \mathbf{n}) \mapsto (\mathbf{x}, \mathbf{n})$, which has bounded distortion. It suffices to prove the continuity of the image of the control sets $(\varepsilon, \mathbf{p}) \to \mathrm{d}\mathcal{I}(\mathbf{p}, \mathcal{B}_{\mathcal{F}_\varepsilon}(\mathbf{p}))$ (resp. likewise with $\mathcal{F}_\varepsilon^+$) by the tangent maps to this embedding, which follows from Lemma 6. □

B Iterative PDE procedure for solving the Eikonal Equation

We compare the FM method with an iterative PDE method similar to the one used for the $\mathbb{R}^2 \times \mathbb{S}^1$-case in [7], in which the BVP is solved using an iterative procedure (with updating) inspired by mathematical morphology [48]. To adhere, to the previous work [7], and for notational convenience we constrain ourselves to the case where the external costs are equal, i.e. $\mathcal{C}_1 = \mathcal{C}_2 = \mathcal{C}$, where of course the general case can be straightforwardly obtained from this special case by a simple position dependent rescaling in the PDE's.

They formulate an auxiliary initial value problem (IVP), for which the 3D analog in $\mathbb{R}^d \times S^{d-1}$ with $d \in \{2, 3\}$, and with $\varepsilon \geq 0$ is the following:

$$\begin{cases} \dfrac{\partial U_{n+1}}{\partial r}(\mathbf{p}, r) = \\ \mathcal{C}^{-1}(\mathbf{p}) \sqrt{\|\nabla_{S^{d-1}} U_{n+1}(\mathbf{p}, r)\|^2 + \dfrac{\varepsilon^2}{\xi^2}\|\nabla_{\mathbb{R}^d} U_{n+1}(\mathbf{p}, r)\|^2 + \dfrac{1-\varepsilon^2}{\xi^2} |\, \mathbf{n} \cdot \nabla_{\mathbb{R}^d} U_{n+1}(\mathbf{p}, r)\,|^2} - 1, \\ U_{n+1}(\mathbf{p}, r_n) = U_n(\mathbf{p}, r_n), \qquad \text{for } \mathbf{p} \neq \mathbf{e}, \\ U_{n+1}(\mathbf{e}, r_n) = 0, \\ U_{n+1}(\mathbf{p}, 0) = \delta_{\mathbf{e}}^M(\mathbf{p}), \end{cases} \tag{52}$$

with source point $\mathbf{p}_S = \mathbf{e} := (\mathbf{0}, \mathbf{a})$, for $n \in \mathbb{N}$. Here $r_n = n\varepsilon$ and $r \in [r_n, r_{n+1}]$ are artificial times of the IVP and $\delta_{(\mathbf{0},\mathbf{a})}^M$ is the morphological delta, given by

$$\delta_{(\mathbf{0},\mathbf{a})}^M(\mathbf{p}) = \begin{cases} 0 & \mathbf{p} = (\mathbf{0}, \mathbf{a}), \\ \infty & \text{else.} \end{cases} \tag{53}$$

Now the limit

$$U_\infty(\mathbf{p}) := \lim_{\varepsilon \to 0} \left(\lim_{n \to \infty} U_{n+1}(\mathbf{p}, (n+1)\varepsilon) \right) \tag{54}$$

gives the viscosity solution $U_\infty(\mathbf{p}) = d_{\mathcal{F}_\varepsilon}(\mathbf{p}, \mathbf{e})$ of the eikonal equation (5) for Finsler function $\mathcal{F}_\varepsilon$ whose dual is given by (23).

We approximate the system (52) with first order, upwind finite differences for the gradients on the right-hand side, and central differences for the time derivate. We use the following stopping criterion:

$$\max_{\mathbf{p}} |U_{n+1}(\mathbf{p}, r_{n+1}) - U_n(\mathbf{p}, r_n)| < \theta, \qquad \theta \in \mathbb{R}. \tag{55}$$

The disadvantage of this method (compared to the single pass anisotropic fast-marching method) is the computational load. The advantage of this PDE-method is a high accuracy near the origin, and that it is very easy to adapt to the (approximative) Reeds-shepp car model without reverse gear (i.e. the metric space $(\mathbb{M}, \mathcal{F}_\varepsilon)$) as we explain next. Namely $W^+(\mathbf{p}, e) = d_{\mathcal{F}_\varepsilon^+}(\mathbf{p}, \mathbf{e})$ is implemented by the same limiting procedure (54) but now applied to

$$\begin{cases} \dfrac{\partial U_{n+1}^+}{\partial r}(\mathbf{p}, r) = \\ \mathcal{C}^{-1}(\mathbf{p}) \sqrt{\|\nabla_{S^{d-1}} U_{n+1}^+(\mathbf{p}, r)\|^2 + \dfrac{\varepsilon^2}{\xi^2}\|\nabla_{\mathbb{R}^d} U_{n+1}^+(\mathbf{p}, r)\|^2 + \dfrac{1-\varepsilon^2}{\xi^2} |\, (\mathbf{n} \cdot \nabla_{\mathbb{R}^d} U_{n+1}^+(\mathbf{p}, r))_+\,|^2} - 1, \\ U_{n+1}^+(\mathbf{p}, r_n) = U_n^+(\mathbf{p}, r_n), \qquad \text{for } \mathbf{p} \neq \mathbf{e}, \\ U_{n+1}^+(\mathbf{e}, r_n) = 0, \\ U_{n+1}^+(\mathbf{p}, 0) = \delta_{\mathbf{e}}^M(\mathbf{p}) \end{cases} \tag{56}$$

C Backtracking of Geodesics in $(\mathbb{M}, d_{\mathcal{F}})$

This section is devoted to a generic ingredient in the proof of Theorem 4, regarding backtracking of Geodesics in the (pseudo)-Metric Space $(\mathbb{M}, d_{\mathcal{F}})$ in general. Although, these results are standard in Finsler Geometry, we aim to provide a concise overview.

Lemma 7 *Let F be an asymmetric norm on a vector space $\mathbb{E}$, and let us assume that F^* is differentiable at $\hat{\mathbf{p}} \in \mathbb{E}^*$. Then*

$$F(\mathrm{d}F^*(\hat{\mathbf{p}})) = 1, \qquad \langle \hat{\mathbf{p}}, \mathrm{d}F^*(\hat{\mathbf{p}}) \rangle = F^*(\hat{\mathbf{p}}).$$

Proof. The first claim follows by differentiating the expression of F^*

$$F^*(\hat{\mathbf{p}}) = \sup_{\dot{\mathbf{p}} \in \mathbb{E} \setminus \{0\}} \frac{\langle \hat{\mathbf{p}}, \dot{\mathbf{p}} \rangle}{F(\dot{\mathbf{p}})} = \max_{F(\dot{\mathbf{p}})=1} \langle \hat{\mathbf{p}}, \dot{\mathbf{p}} \rangle.$$

The second claim is Euler's formula for homogeneous functions. □

Proposition 5 *Let $\mathbf{p}_{\mathrm{S}}, \mathbf{p}_{\mathrm{T}} \in \mathbb{M}$, let γ be a minimal geodesic from $\mathbf{p}_{\mathrm{S}}$ to $\mathbf{p}_{\mathrm{T}}$ with respect to a continuous metric $\mathcal{F}$, and let $t \in [0, 1]$. Assume that the distance map U from $\mathbf{p}_{\mathrm{S}}$ is differentiable at $\gamma(t)$, and that the dual metric $\mathcal{F}^*$ is differentiable w.r.t. the second variable at $(\gamma(t), \mathrm{d}U(\gamma(t)))$. Then γ is differentiable at time t and with $L := d_{\mathcal{F}}(\mathbf{p}_{\mathrm{S}}, \mathbf{p}_{\mathrm{T}})$*

$$\dot{\gamma}(t) = L \; \mathrm{d}_{\hat{\mathbf{p}}} \mathcal{F}^*(\gamma(t), \mathrm{d}U(\gamma(t))). \tag{57}$$

Proof. The path γ has constant speed L, and $t \mapsto U(\gamma(t))$ increases linearly from 0 to L on it. Let $t \in [0,1]$ be as in the statement of the proposition, and let $\dot{\Gamma}(t) := \lim_{n\to\infty} (\gamma(t+\varepsilon_n) - \gamma(t))/\varepsilon_n$ for some sequence $\varepsilon_n \to 0$. Then

$$\mathcal{F}(\gamma(t), \dot{\Gamma}(t)) = L \qquad \langle \mathrm{d}U(\gamma(t)), \dot{\Gamma}(t)\rangle = L.$$

For typographic simplicity let us denote $\mathbf{p} := \gamma(t)$, $\dot{\mathbf{p}} := \dot{\Gamma}(t)$, $F = \mathcal{F}(\mathbf{p}, \cdot)$ and $F^* := \mathcal{F}^*(\mathbf{p}, \cdot)$. By Lemma 7 and the eikonal equation (5), the vector $\dot{\mathbf{q}} = \mathrm{d}F^*(\mathrm{d}U(\mathbf{p}))$ obeys

$$F(\dot{\mathbf{q}}) = F(\mathrm{d}F^*(\mathrm{d}U(\mathbf{p}))) = 1,$$
$$\langle \mathrm{d}U(\mathbf{p}), \dot{\mathbf{q}}\rangle = \langle \mathrm{d}U(\mathbf{p}), \mathrm{d}F^*(\mathrm{d}U(\mathbf{p}))\rangle = F^*(\mathrm{d}U(\mathbf{p})) = 1.$$

Note that the duality-bracket/norm inequality is saturated by $\langle \mathrm{d}U(\mathbf{p}), \dot{\mathbf{q}}\rangle = 1 = F^*(\mathrm{d}U(\mathbf{p}))F(\dot{\mathbf{q}})$, and that the assumed differentiability of the dual norm F^* at the point $\hat{\mathbf{p}} = \mathrm{d}U(\mathbf{p})$ implies the strict convexity of the primal norm F (up to 1-homogeneity) at the point $\mathrm{d}F^*(\hat{\mathbf{p}}) = \dot{\mathbf{q}}$. Hence $\dot{\mathbf{q}}$ is the unique solution to the system "$F^*(\dot{\mathbf{q}}) = 1$ and $\langle \mathrm{d}U(\mathbf{p}), \dot{\mathbf{q}}\rangle = 1$", and therefore $\dot{\Gamma}(t) = L\dot{\mathbf{q}}$. This implies the differentiability of γ at time t, and the announced equality. □

Remark 14 (Lagrangians and Hamiltonians) Given an arbitrary metric $\mathcal{F}$ on $\mathbb{M}$, its half-square $\mathfrak{L} := \frac{1}{2}\mathcal{F}^2 : T(\mathbb{M}) \to [0, +\infty]$ is usually called the Lagrangian. The shortest path problem (1) can be reformulated in terms of the Lagrangian, thanks to the following identity which follows from Cauchy-Schwartz's inequality

$$d_{\mathcal{F}}(\mathbf{p}, \mathbf{q})^2 = \inf\{\int_0^1 \mathcal{F}(\gamma(t), \dot{\gamma}(t))^2 dt;\ \gamma \in \mathrm{Lip}([0,1], \mathbb{M}), \\ , \gamma(0) = \mathbf{p}, \gamma(1) = \mathbf{q}\}. \quad (58)$$

A path γ is a minimizer of (58) iff it is simultaneously normalized and a minimizer of (1). The Hamiltonian $\mathfrak{H}$ is the Lengendre-Fenchel transform of its Lagrangian $\mathfrak{L}$ with respect to the second variable, hence $\mathfrak{H} = \frac{1}{2}(\mathcal{F}^*)^2$ (for details see [6, ch.14.8]) The eikonal equation can thus be rephrased in terms of the Hamiltonian:

$$\mathcal{F}^*(\mathbf{p}, \mathrm{d}U(\mathbf{p})) = 1 \ \Leftrightarrow\ \mathfrak{H}(\mathbf{p}, \mathrm{d}U(\mathbf{p})) = \frac{1}{2}.$$

The Hamiltonian can also be used to reformulate the back-tracing ODE of geodesics, thanks to the following identity which follows from the eikonal equation: for any $\mathbf{p} \in \mathbb{M}$

$$\begin{aligned} \mathrm{d}_{\hat{\mathbf{p}}}\mathfrak{H}(\mathbf{p}, \mathrm{d}U(\mathbf{p})) =& \mathcal{F}^*(\mathbf{p}, \mathrm{d}U(\mathbf{p}))\, \mathrm{d}_{\hat{\mathbf{p}}}\mathcal{F}^*(\mathbf{p}, \mathrm{d}U(\mathbf{p})) \\ =& \mathrm{d}_{\hat{\mathbf{p}}}\mathcal{F}^*(\mathbf{p}, \mathrm{d}U(\mathbf{p})). \end{aligned} \quad (59)$$

In geometric control theory this Hamiltonian is often referred to the 'fixed time Hamiltonian of the action functional', cf. [2, 7, 46], and is typically used [39] in the Pontryagin maximum principle [2] for (sub-)Riemannian geodesics.

D Characterization of Cusps: Proof of Lemma 1

Consider Lemma 1. The structure of this lemma is $a \Leftrightarrow b \Leftrightarrow c$. The implication $a \Rightarrow b$ is trivial. The equivalence $b \Leftrightarrow c$ follows by Theorem 4 and Theorem 2. The implication $b \Rightarrow a$ remains.

Suppose the d-th spatial control aligned with $\mathbf{n}(t_0)$ vanishes $\tilde{u}(t_0) = 0$. Now we show by contradiction that in this case $\dot{\tilde{u}}(t_0) \neq 0$. Suppose $\tilde{u}(t_0) = \dot{\tilde{u}}(t_0) = 0$.

Then by application of the PMP (Pontryagin Maximum Principle), similar to [7, App.A], [24]) and coercivity/invertibility of the SR-metric tensor $\mathcal{G}_0|_{\gamma(t_0)}$, recall (24), constrained to the horizontal part of the tangent space $\Delta|_{\gamma(t)} = \{(\mathbf{p}_0 = (\mathbf{x}_0, \mathbf{n}_0), \dot{\mathbf{p}}_0 = (\dot{\mathbf{x}}_0, \dot{\mathbf{n}}_0)) \in T(\mathbb{M}) \mid \mathbf{n}_0 \equiv \dot{x}_0\}$, that the (analytic) spatial control variable $\tilde{u} = \mathcal{C}_1^{-2}\tilde{\lambda}$ vanishes for all times (for $d = 2$ this is directly deduced from the pendulum phase portrait [39] in momentum space). This leaves only purely angular momentum and motion, contradicting $\dot{\mathbf{x}}(\cdot) \neq \mathbf{0}$.

Next we verify that

$$\tilde{u}(t_0) = \dot{\tilde{u}}(t_0) = 0 \quad \Rightarrow \quad \frac{d}{dt}\tilde{\lambda}(t)\Big|_{t=t_0} = \tilde{\lambda}(t_0) = 0.$$

By the chain rule for differentiation (applied to the d-th spatial momentum component $\tilde{\lambda}(t) = \langle \lambda, (\mathbf{n}(t), \mathbf{0})\rangle$):

$$\begin{aligned} \tfrac{d}{dt}\tilde{\lambda}(t)\big|_{t=t_0} &= \tfrac{d}{dt}(\mathcal{C}_1(\gamma(t)))^{-2}\tilde{u}(t)\big|_{t=t_0} \\ &= \tfrac{d}{dt}(\mathcal{C}_1(\gamma(t)))^{-2}\big|_{t=t_0}\ \tilde{u}(t_0) + \\ &\qquad \tfrac{d}{dt}(\mathcal{C}_1(\gamma(t)))^{-2}\big|_{t=t_0}\ \dot{\tilde{u}}(t_0) = 0. \end{aligned}$$

and we deduce from the canonical equations of PMP (cf. [24]) that

$$\tilde{\lambda}(t_0) = \dot{\tilde{\lambda}}(t_0) = 0 \Rightarrow \tilde{\lambda} = 0 \Rightarrow \tilde{u} = 0$$

References

1. A. Agrachev, D. Barilari, and U. Boscain. *Introduction to Riemannian and Sub-Riemannian geometry.* http://webusers.imj-prg.fr/~davide.barilari/Notes, 2011.
2. A. A. Agrachev and Y. L. Sachkov. *Control Theory from the Geometric Viewpoint*, volume 87 of *Encyclopaedia of Mathematical Sciences*. Springer Berlin Heidelberg, Berlin, Heidelberg, 2004.
3. C. Arzela. Sulle funzioni di linee. *Mem. Accad. Sci. lst. Bologna Cl. Sci. Fis. Mat.*, 5(5):55–74, 1895.
4. G. Ascoli. Le curve limiti di una varieta data di curve. *Atti della R. Accad. Dei Lincei Memorie della Cl. Sci. Fis. Mat. Nat.*, 18(3):521–586, 1883.
5. L. Astola and L.M.J. Florack. Finsler geometry on higher order tensor fields andapplications tohigh angular resolution diffusion imaging. *International Journal of Computer Vision*, 92(3):325–336, 2011.
6. D. Bao, S.-S. Chern, and Z. Shen. *An Introduction to Riemann-Finsler Geometry.* Graduate Texts in Mathematics. Springer New York, 2000.
7. E. Bekkers, R. Duits, A. Mashtakov, and G. Sanguinetti. A PDE Approach to Data-Driven Sub-Riemannian Geodesics in SE(2). *SIAM J. Imaging Sci.*, 8(4):2740–2770, January 2015.
8. A. Bellaiche. chapter The tangent space in sub-Riemannian geometry. Birkhauser, 1996.
9. U. Boscain, G. Charlot, and F. Rossi. Existence of planar curves minimizing length and curvature. *Proc. Steklov Inst. Math.*, 270(1):43–56, October 2010.
10. U. Boscain, R. Duits, F. Rossi, and Y. Sachkov. Curve cuspless reconstruction via sub-Riemannian geometry. *ESAIM: Control, Optimisation and Calculus of Variations*, 20(3):748–770, July 2014.
11. E. Caruyer, A. Daducci, M. Descoteaux, J-C. Houde, J-P. Thiran, and R. Verma. Phantomas: a flexible software library to simulate diffusion MR phantoms. In *ISMRM*, Milan, Italy, May 2014.

E Table of Notations

Symbol	Explanation	Reference
$\mathbb{R}^d$, $\mathbf{x}$	Position space with vectors $\mathbf{x} = (x^1, \dots, x^d)^T$.	Sect. 1.1, ...
$\mathbb{S}^{d-1}$,$\mathbf{n}$	Angular space, $\mathbb{S}^{d-1} = \{\mathbf{n} \in \mathbb{R}^d \mid \|\mathbf{n}\| = 1\}$.	Sect. 1.1, ...
$\mathbf{a}$	Reference axis. For $d = 2$, $\mathbf{a} = (1, 0)^T$, for $d = 3$, $\mathbf{a} = (0, 0, 1)^T$.	Eq. (11), Remark 3
$\mathbb{M}$, $\mathbf{p}$	Manifold $\mathbb{M} = \mathbb{R}^d \times \mathbb{S}^{d-1}$, with $\mathbf{p} = (\mathbf{x}, \mathbf{n}) \in \mathbb{M}$	Sect. 1.1 ...
$T(\mathbb{M})$, $T^*(\mathbb{M})$, $T_{\mathbf{p}}(\mathbb{M})$	Tangent bundle $T(\mathbb{M}) = \{(\mathbf{p}, \dot{\mathbf{p}}) \mid \mathbf{p} \in \mathbb{M}, \dot{\mathbf{p}} \in T_{\mathbf{p}}(\mathbb{M})\}$, and cotangent bundle $T^*(\mathbb{M})$, with tangent space $T_{\mathbf{p}}(\mathbb{M})$.	Sect. 1.1, Sect. 2.5, ...
Γ, $\boldsymbol{\gamma}$	Space $\Gamma = \mathrm{Lip}([0, 1], \mathbb{M})$ of admissible curves, with $t \mapsto \boldsymbol{\gamma}(t) = (\mathbf{x}(t), \mathbf{n}(t))$.	Eq. (1), ...
$\mathcal{F}$, $\mathcal{F}^*$, $\mathcal{F}_0$, $\mathcal{F}_0^+$ $\mathcal{F}_\varepsilon$, $\mathcal{F}_\varepsilon^+$	Finsler function $\mathcal{F}$ defined on $\mathbb{M}$, its dual $\mathcal{F}^* : T^*(\mathbb{M}) \to \mathbb{R}$ the models with and without reverse gear $\mathcal{F}_0$, $\mathcal{F}_0^+$ and their approximations $\mathcal{F}_\varepsilon$, $\mathcal{F}_\varepsilon^+$.	Sect. 1.1, Eqs. (2), (3), (5), (6), (16), (17), ...
$d_{\mathcal{F}}$, U	Distance function $d_{\mathcal{F}}(\mathbf{p}, \mathbf{q})$ for $\mathbf{p}, \mathbf{q} \in \mathbb{M}$, and $U(\mathbf{p}) = d_{\mathcal{F}}(\mathbf{p}_S, \mathbf{p})$ for a fixed source $\mathbf{p}_S \in \mathbb{M}$	Eqs. (1), (4), ...
ε	Anisotropy parameter in the metric, $\varepsilon = 0$ corresponds to the sub-Riemannian manifold case.	Eqs. (16), (17),...
$\propto$	We write $\dot{\mathbf{x}} \propto \mathbf{n}$ when $\dot{\mathbf{x}} = \lambda \mathbf{n}$ for some $\lambda \in \mathbb{R}$	Eqs. (2), (3), Sect. 2.3, Thm. 1,
$\mathcal{C}_1$, $\mathcal{C}_2$, ξ	External cost $\mathcal{C}_i : \mathbb{M} \to \mathbb{R}^+$, analytic and strictly bounded from below, and $\xi > 0$ to balance the cost of spatial motion relative to angular motion, when we choose $\mathcal{C}_1 = \xi \mathcal{C}_2$	Sect. 1.2, ...
B, $B_{\mathcal{F}}$	Set of controls B, and the set of admissible controls $B_{\mathcal{F}}(\mathbf{p}) = \{\dot{\mathbf{p}} \in T_{\mathbf{p}}(\mathbb{M}) \mid \mathcal{F}(\mathbf{p}, \dot{\mathbf{p}} \leq 1)\}$	Fig. 1, Eq. (7), (8), Appendix A
$(\cdot)_-$, $(\cdot)_+$	$(\cdot)_- = \min(\cdot, 0)$, $(\cdot)_+ = \max(\cdot, 0)$	Eqs. (15),(16),(17),(18), Prop. 1, Cor. 1, Lemma 4
$\mathfrak{R}$, $\bar{\mathfrak{R}}$, $\mathfrak{R}^c$	Subset $\mathfrak{R} \in \mathbb{M}$ of end-points that are reached by cuspless geodesics, the closure $\bar{\mathfrak{R}}$ and its complement $\bar{\mathfrak{R}}^c$	Definition 4, Remark 3, Theorem 3, Section 4.
$\mathcal{A}_i$, ω^i	Left-invariant frame $\mathcal{A}_i$ and the dual frame ω^i.	Section 4, Eqs. (39), (40).
u^i, $\hat{p}_i$	Controls (velocity components) u^i and momentum components $\hat{p}_i$	Def. 2.4, Def. 4, Sect. 4, Sect. 5
$\mathcal{G}_{\mathbf{p},\varepsilon}$, $\tilde{\mathcal{G}}_{\mathbf{p},\varepsilon}$	Metric tensors $\mathcal{G}_{\mathbf{p},\varepsilon}, \tilde{\mathcal{G}}_{\mathbf{p},\varepsilon} : T_{\mathbf{p}}(\mathbb{M}) \times T_{\mathbf{p}}(\mathbb{M}) \to \mathbb{R}^+$	Eq. (24), (25)
∇, $\mathcal{G}_\varepsilon^{-1}\mathrm{d}$, $\tilde{\mathcal{G}}_{\mathbf{p},\varepsilon}^{-1}\mathrm{d}$	Standard gradient $\nabla = (\nabla_{\mathbb{R}^d}, \nabla_{\mathbb{S}^{d-1}})$, the intrinsic gradient $\mathcal{G}_{\mathbf{p},\varepsilon}^{-1}\mathrm{d}$ of the manifold $(\mathbb{M}_+, d_{\mathcal{F}_\varepsilon})$ and $\tilde{\mathcal{G}}_{\mathbf{p},\varepsilon}^{-1}\mathrm{d}$ the intrinsic gradient of $(\mathbb{M}_-, d_{\mathcal{F}_\varepsilon^+})$	Cor. 1, Thm. 4, Remark 30,
$F_{M,\mathbf{w}}$, $F^*_{M,\hat{\mathbf{w}}}$	Norm $F_{M,\mathbf{w}} : \mathbb{R}^n \to \mathbb{R}^+$ and dual norm $F^*_{M,\hat{\mathbf{w}}} : (\mathbb{R}^n)^* \to \mathbb{R}^+$	Cor. 1, Thm. 4, end of Section 5
X, S, M	Discrete subsets of the spaces $\mathbb{R}^d$, $\mathbb{S}^{d-1}$, $\mathbb{M}$.	
$D^\varepsilon_{\mathbf{n}}$	Symmetric positive definite matrix $D^\varepsilon_{\mathbf{n}} = \mathbf{n} \otimes \mathbf{n} + \varepsilon^2(\mathrm{Id} - \mathbf{n} \otimes \mathbf{n})$	Eq. (26), (27), (37)
$\mathbb{M}_+$, $\mathbb{M}_-$, $\partial\mathbb{M}_\pm$	$\mathbb{M}_+ = \{\mathbf{p} \in \mathbb{M} \mid \langle \mathrm{d}U^+(\mathbf{p}), \mathbf{n}\rangle > 0\}$, $\mathbb{M}_- = \{\mathbf{p} \in \mathbb{M} \mid \langle \mathrm{d}U^+(\mathbf{p}), \mathbf{n}\rangle < 0\}$ and their boundary	Cor. 1, Thm. 4, Remarks 8
N_x, N_y, N_z, N_o	Resolution in spatial/angular coordinates	Sect. 7
σ, p	Parameters $\sigma > 0$, $p \in \mathbb{N}$ of the cost function $\mathcal{C}$	Sect. 7

Table 1 Symbols used throughout the paper, their brief explanation and references to where they appear, or where they are defined/first appear. The dots in the Reference column indicate that they are used frequently.

12. D. Chen, J-M. Mirebeau, and L. D. Cohen. Vessel tree extraction using radius-lifted keypoints searching scheme and anisotropic fast marching method. *Journal of Algorithms & Computational Technology*, 10(4):224–234, December 2016.
13. Da Chen, Jean-Marie Mirebeau, and Laurent D. Cohen. Global Minimum for a Finsler Elastica Minimal Path Approach. *Int J Comput Vis*, pages 1–26, December 2016.
14. G. Citti and A. Sarti. A Cortical Based Model of Perceptual Completion in the Roto-Translation Space. *J Math Imaging Vis*, 24(3):307–326, February 2006.
15. T. G. Close, J-D. Tournier, F. Calamante, L. A. Johnston, I. Mareels, and A. Connelly. A software tool to generate simulated white matter structures for the assessment of fibre-tracking algorithms. *NeuroImage*, 47(4):1288–1300, October 2009.
16. M. G. Crandall, H. Ishii, and P-L Lions. User's guide to viscosity solutions of second order partial differential equations. *Bull. Amer. Math. Soc.*, 27(1):1–67, 1992.
17. M. G. Crandall and P-L Lions. Viscosity solutions of Hamilton-Jacobi equations. *Trans. Amer. Math. Soc.*, 277(1):1–42, 1983.

18. Chen Da. *New Minimal Paths Models for Tubular Structure Extraction and Image Segmentation*. PhD thesis, University Paris-Dauphine, 2016.
19. M. Descoteaux, R. Deriche, T. R. Knosche, and A. Anwander. Deterministic and Probabilistic Tractography Based on Complex Fibre Orientation Distributions. *IEEE Transactions on Medical Imaging*, 28(2):269–286, February 2009.
20. L. E. Dubins. On Curves of Minimal Length with a Constraint on Average Curvature, and with Prescribed Initial and Terminal Positions and Tangents. *American Journal of Mathematics*, 79(3):497–516, 1957.
21. R. Duits, U. Boscain, F. Rossi, and Y. Sachkov. Association Fields via Cuspless Sub-Riemannian Geodesics in SE(2). *J Math Imaging Vis*, 49(2):384–417, December 2013.
22. R. Duits, M. Felsberg, G. Granlund, and B. ter Haar Romeny. Image Analysis and Reconstruction using a Wavelet Transform Constructed from a Reducible Representation of the Euclidean Motion Group. *Int J Comput Vision*, 72(1):79–102, July 2006.
23. R. Duits, A. Ghosh, T. Dela Haije, and A. Mashtakov. On sub-Riemannian geodesics in SE(3) whose spatial projections do not have cusps. *arXiv:1305.6061 [math]*, May 2013. arXiv: 1305.6061.
24. R. Duits, A. Ghosh, T. Dela Haije, and Y. Sachkov. Cuspless Sub-Riemannian Geodesics within the Euclidean Motion Group SE(d). In G. Citti and A. Sarti, editors, *Neuromathematics of Vision*, Lecture Notes in Morphogenesis, pages 173–215. Springer Berlin Heidelberg, 2014. DOI: 10.1007/978-3-642-34444-2_5.
25. R. Duits, M. H. J. Janssen, J. Hannink, and G. R. Sanguinetti. Locally Adaptive Frames in the Roto-Translation Group and Their Applications in Medical Imaging. *J Math Imaging Vis*, 56(3):367–402, March 2016.
26. M. Eshagh. Alternative expressions for gravity gradients in local north-oriented frame and tensor spherical harmonics. *Acta Geophysica*, 58(2):215–243, 2010.
27. Jérôme Fehrenbach and Jean-Marie Mirebeau. Sparse Non-negative Stencils for Anisotropic Diffusion. *Journal of Mathematical Imaging and Vision*, pages 1–25, 2013.
28. P.T. Fletcher and S. Joshi. Riemannian geometry for the statistical analysis of diffusion tensor data. *Signal Processing*, 87(2):250–262, 2007.
29. M. Gromov. chapter Carnot-Carathéodory spaces seen from within. Birkhauser, 1996.
30. S. Jbabdi, P. Bellec, R. Toro, J. Daunizeau, M. Pélégrini-Issac, and H. Benali. Accurate Anisotropic Fast Marching for Diffusion-Based Geodesic Tractography. *Int J Biomed Imaging*, 2008, 2008.
31. S. Jbabdi and H. Johansen-Berg. Tractography: Where Do We Go from Here? *Brain Connectivity*, 1(3):169–183, August 2011.
32. C. Lenglet, E. Prados, J. Pons, R. Deriche, and O. Faugeras. Brain Connectivity Mapping Using Riemannian Geometry, Control Theory, and PDEs. *SIAM J. Imaging Sci.*, 2(2):285–322, January 2009.
33. A. Mashtakov, R. Duits, Y. Sachkov, E. Bekkers, and I. Beschastnyi. Tracking of Lines in Spherical Images via Sub-Riemannian Geodesics on SO(3). *arXiv:1604.03800 [math]*, April 2016. arXiv: 1604.03800.
34. A. P. Mashtakov, A. A. Ardentov, and Y. L. Sachkov. Parallel Algorithm and Software for Image Inpainting via Sub-Riemannian Minimizers on the Group of Rototranslations. *Numerical Mathematics: Theory, Methods and Applications*, 6(01):95–115, February 2013.
35. J. Melonakos, V. Mohan, M. Niethammer, K. Smith, M. Kubicki, and A. Tannenbaum. Finsler Tractography for White Matter Connectivity Analysis of the Cingulum Bundle. *Med Image Comput Comput Assist Interv*, 10(0 1):36–43, 2007.
36. J. Melonakos, E. Pichon, S. Angenent, and A. Tannenbaum. Finsler active contours. *IEEE Trans Pattern Anal Mach Intell*, 30(3):412–423, March 2008.
37. J. Mirebeau. Anisotropic Fast-Marching on Cartesian Grids Using Lattice Basis Reduction. *SIAM J. Numer. Anal.*, 52(4):1573–1599, January 2014.
38. J-M. Mirebeau. Efficient fast marching with Finsler metrics. *Numer. Math.*, 126(3):515–557, July 2013.
39. I. Moiseev and Y. L. Sachkov. Maxwell strata in sub-Riemannian problem on the group of motions of a plane. *ESAIM: Control, Optimisation and Calculus of Variations*, 16(02):380–399, April 2010.
40. Sasumu Mori. *Introduction to Diffusion Tensor Imaging*. Elsevier Science, 2007.
41. M. Pechaud, R. Keriven, and G. Peyre. Extraction of tubular structures over an orientation domain. In *IEEE Conference on Computer Vision and Pattern Recognition, 2009. CVPR 2009*, pages 336–342, June 2009.
42. J. Petitot. The neurogeometry of pinwheels as a sub-Riemannian contact structure. *Journal of Physiology-Paris*, 97(2–3):265–309, March 2003.
43. J.M. Portegies and R. Duits. New exact and numerical solutions of the (convection-)diffusion kernels on SE(3). arxiv, 2016. https://arxiv.org/pdf/1604.03843.pdf.
44. J. A. Reeds and L. A. Shepp. Optimal paths for a car that goes both forwards and backwards. *Pacific J. Math.*, 145(2):367–393, 1990.
45. Elisabeth Rouy and Agnès Tourin. A Viscosity Solutions Approach to Shape-From-Shading. *SIAM Journal on Numerical Analysis*, 29(3):867–884, July 1992.
46. Y. L. Sachkov. Cut locus and optimal synthesis in the sub-Riemannian problem on the group of motions of a plane. *ESAIM: Control, Optimisation and Calculus of Variations*, 17(2):293–321, April 2011.
47. G. R. Sanguinetti, E. J. Bekkers, R. Duits, M. H. J. Janssen, A. Mashtakov, and J-M Mirebeau. Sub-Riemannian Fast Marching in SE(2). In A. Pardo and J. Kittler, editors, *Progress in Pattern Recognition, Image Analysis, Computer Vision, and Applications*, number 9423 in Lecture Notes in Computer Science, pages 366–374. Springer International Publishing, November 2015. DOI: 10.1007/978-3-319-25751-8_44.
48. M. Schmidt and J. Weickert. Morphological Counterparts of Linear Shift-Invariant Scale-Spaces. *J Math Imaging Vis*, 56(2):352–366, April 2016.
49. N. Sepasian. *Multi-Valued Geodesic Tractography for Diffusion Weghted Imaging*. PhD thesis, Eindhoven University of Technology, Dep. of Biomedical Engineering, 2011.
50. J. A. Sethian and A. Vladimirsky. Ordered upwind methods for static Hamilton–Jacobi equations. *PNAS*, 98(20):11069–11074, September 2001.
51. A.F.M. ter Elst and D.W. Robinson. Weighted subcoercive operators on lie groups. *Journal of Functional Analysis*, 157:88–163, 1998.
52. J-D. Tournier, F. Calamante, and A. Connelly. MRtrix: Diffusion tractography in crossing fiber regions. *Int. J. Imaging Syst. Technol.*, 22(1):53–66, March 2012.
53. J. N. Tsitsiklis. Efficient algorithms for globally optimal trajectories. *IEEE Transactions on Automatic Control*, 40(9):1528–1538, September 1995.

54. David S Tuch. Q-ball imaging. *Magn Reson Med*, 52(6):1358–1372, Dec 2004.
55. A. Vladimirsky. Static PDEs for time-dependent control problems. *Interfaces and Free Boundaries*, pages 281–300, 2006.